INFORMATION TO USERS

This was produced from a copy of a document sent to us for microfilming. While the most advanced technological means to photograph and reproduce this document have been used, the quality is heavily dependent upon the quality of the material submitted.

The following explanation of techniques is provided to help you understand markings or notations which may appear on this reproduction.

1. The sign or "target" for pages apparently lacking from the document photographed is "Missing Page(s)". If it was possible to obtain the missing page(s) or section, they are spliced into the film along with adjacent pages. This may have necessitated cutting through an image and duplicating adjacent pages to assure you of complete continuity.
2. When an image on the film is obliterated with a round black mark it is an indication that the film inspector noticed either blurred copy because of movement during exposure, or duplicate copy. Unless we meant to delete copyrighted materials that should not have been filmed, you will find a good image of the page in the adjacent frame.
3. When a map, drawing or chart, etc., is part of the material being photographed the photographer has followed a definite method in "sectioning" the material. It is customary to begin filming at the upper left hand corner of a large sheet and to continue from left to right in equal sections with small overlaps. If necessary, sectioning is continued again—beginning below the first row and continuing on until complete.
4. For any illustrations that cannot be reproduced satisfactorily by xerography, photographic prints can be purchased at additional cost and tipped into your xerographic copy. Requests can be made to our Dissertations Customer Services Department.
5. Some pages in any document may have indistinct print. In all cases we have filmed the best available copy.

University
Microfilms
International

300 N. ZEEB ROAD, ANN ARBOR, MI 48106
18 BEDFORD ROW, LONDON WC1R 4EJ, ENGLAND

8003805

WEI, MING-YING

THE ENERGY BUDGETS OF A DEVELOPING CYCLONE OVER THE EAST CHINA SEA DURING THE 1975 AIR MASS TRANSFORMATION EXPERIMENT

The University of Oklahoma PH.D. 1979

University
Microfilms
International 300 N. Zeeb Road, Ann Arbor, MI 48106 18 Bedford Row, London WC1R 4EJ, England

THE UNIVERSITY OF OKLAHOMA

GRADUATE COLLEGE

THE ENERGY BUDGETS OF A DEVELOPING CYCLONE OVER THE EAST CHINA SEA DURING THE 1975 AIR MASS TRANSFORMATION EXPERIMENT

A DISSERTATION
SUBMITTED TO THE GRADUATE FACULTY
in partial fulfillment of the requirements for the
degree of
DOCTOR OF PHILOSOPHY

By
MING-YING WEI
Norman, Oklahoma
1979

THE ENERGY BUDGETS OF A DEVELOPING CYCLONE OVER THE EAST CHINA SEA DURING THE 1975 AIR MASS TRANSFORMATION EXPERIMENT

APPROVED BY

Jay S. Fein

James F. Kimpel

Edward J. Blick

DISSERTATION COMMITTEE

ACKNOWLEDGMENTS

I wish to express my sincere gratitude to Drs. Jay S. Fein and James F. Kimpel for their interest, guidance and encouragement throughout the entire research. I am also thankful to Drs. Yoshi K. Sasaki, Rex L. Inman and Edward F. Blick for many helpful discussions and suggestions.

I am very grateful to all my dear friends for their patience and kindness in answering my various questions. I also want to acknowledge a very special person, Main R. Hutcheson. Special appreciation is given to Ms. Jo Ann Oberst for her expert typing and Ms. Joan Kimpel for her excellent drafting.

This research was accomplished in connection with graduate study at the University of Oklahoma and was sponored by the National Science Foundation under grant ATM74-23024A01 and ATM77-17773.

ABSTRACT

The available potential and kinetic energy budgets are evaluated for a developing cyclone over the East China Sea during the 1975 Air Mass Transformation Experiment. The computations are made in a quasi-Lagrangian frame for areas of approximately 6 x 10^6 km^2 at 12-hour intervals starting at 0000 GMT 13 February and ending at 1200 GMT 15 February 1975. The relationship between the cyclone development and the amount of energy supplied from the ocean during air mass modification is also examined.

Three components of the diabatic processes are considered. Both the stable and convective latent heat release are estimated; the latter is accomplished using Kuo's cumulus parameterization scheme. The sensible heat transferred from the ocean is computed by employing the bulk aerodynamic method. The radiational heating is estimated considering modeled cloud distributions. The magnitudes of the individual diabatic heating rates are comparable to those in other studies. It is shown that the generation of storm's available potential energy by diabatic processes is small compared to the internal source resulting from the temperature advection, suggesting that the energy supplied from the ocean during air mass modification is not very important in the immediate cyclone development. However, at a time scale different from that of cyclone development, the continuous heating of the atmosphere by the ocean creates a situation where an invasion of cold, continental air gives rise to strong baroclinicity, which in turn is favorable for the development of extratropical cyclones.

Part of the storm's available potential energy is converted through large scale vertical motion and part of it is transferred to the subgrid scale processes; of the available potential energy converted, some is used to produce kinetic energy within the storm system and some is used as expansion work along the boundaries. In the mean, the kinetic energy is obtained from both the cross-contour flow and the subgrid scale motion, and is exported out of the storm system. The subgrid scale processes and the interaction between the storm system and its environment are demonstrated to be important in this case study.

TABLE OF CONTENTS

Chapter

Appendices

LIST OF SYMBOLS

A	available potential energy per unit area
c	speed of sound
c_p	specific heat at constant pressure
c_v	specific heat at constant volume
C_D	drag coefficient
C_g	geostrophic drag coefficient
D	frictional dissipation
e	internal energy per unit mass
E	1. moisture flux from underlying surface 2. total internal energy of a fluid system
f	Coriolis parameter
$\mathbb{F}$	frictional force
F_S	sensible heat flux from underlying surface
g	gravitational acceleration
h	height in natural atmosphere
H	height in reference atmosphere
J	transformation Jacobian between height and isentropic coordinates
k	1. horizontal kinetic energy per unit mass 2. von Karmen constant
K	kinetic energy per unit area
L	latent heat of condensation

M_t	moisture convergence due to large scale flow and evaporation
p	pressure
p_b	level of cloud base
p_t	level of cloud top
P	total precipitation rate
P_C	precipitation rate due to convective latent heat release
P_S	precipitation rate due to stable latent heat release
q	specific humidity
q_s	1. saturation specific humidity 2. specific humidity at sea surface
q_a	specific humidity of air
Q	non-frictional diabatic heating rate: $Q = Q_L + Q_S + Q_R$
Q_F	frictional heating rate
Q_L	rate of total latent heat release
Q_{LC}	rate of convective latent heat release
Q_{LS}	rate of stable latent heat release
Q_R	radiational heating rate
Q_S	rate of sensible heat addition from underlying surface
Q_T	total diabatic heat rate: $Q_T = Q_L + Q_S + Q_R + Q_F$
R	gas constant for dry air
R_v	gas constant for water vapor
t	time
T	temperature
T_c	cloud temperature
T_s	temperature at sea surface
U_a	wind speed of air

U_g	surface geostrophic wind speed
dV	differential volume in pressure coordinates: $dV = dx \cdot dy \cdot dp$
$\mathbb{V}$	horizontal wind velocity: $\mathbb{V} = \frac{dx}{dt}\vec{i} + \frac{dy}{dt}\vec{j}$
$\vec{V}$	wind velocity in height coordinates: $\vec{V} = \frac{dx}{dt}\vec{i} + \frac{dy}{dt}\vec{j} + \frac{dz}{dt}\vec{k}$
w	z component of $\vec{V}$
$\mathbb{W}$	horizontal velocity at which storm volume moves: $\mathbb{W} = \frac{\delta x}{\delta t}\vec{i} + \frac{\delta y}{\delta t}\vec{j}$
$\vec{W}$	heat flux
z	height
z_o	surface roughness parameter
α	specific volume
β	angle between surface geostrophic wind vector and shear stress
ε	efficiency factor
θ	potential temperature
θ_o	lowest potential temperature in the natural atmosphere
$\varkappa$	ratio of R to c_p
π	total potential energy per unit area
ρ	density
σ	horizontal area of the storm volume
$d\sigma$	differential area at the surface or any boundary
$d\tau$	differential volume in height coordinates $d\tau = dx \cdot dy \cdot dz$
φ	geopotential or potential energy per unit mass
Φ	total potential energy of a fluid system
χ	deviation from hydrostatic balance

ψ	dummy variable
ω	vertical velocity in pressure coordinates: $\omega = \frac{dp}{dt}$
$\tilde{\omega}$	vertical velocity at which the storm volume moves: $\tilde{\omega} = \frac{\delta p}{\delta t}$

Subscripts

a	denotes air
e	denotes hydrostatic equilibrium
N	denotes the outward normal to the boundary of a fluid system
r	denotes reference atmosphere
s	denotes 1. surface 2. saturation 3. sea
T	denotes the top of the atmosphere

Operators

d	total derivative
∂	partial derivative
$\frac{d}{dt}$	Lagrangian time rate of change
$\frac{\partial}{\partial t}$	Eulerian time rate of change
$\frac{\delta}{\delta t}$	quasi-Lagrangian time rate of change
∇	del operator: $\nabla = \frac{\partial}{\partial x}\vec{i} + \frac{\partial}{\partial y}\vec{j} + \frac{\partial}{\partial z}\vec{k}$ in Appendix A $\nabla = \frac{\partial}{\partial x}\vec{i} + \frac{\partial}{\partial y}\vec{j} + \frac{\partial}{\partial p}\vec{k}$ everywhere else
$\frac{1}{g}\int dV$	integral over the mass of a fluid system
$\int d\tau$	integral over the volume of a fluid system

$\int d\sigma$	integral over a specified surface
$\oint d\sigma$	integral over entire boundary surface
$(\bar{\ })$	1. average surface pressure as in $\overline{p_s}$ 2. spatial average within a grid mesh, denoting the grid scale
$(\ )'$	deviation from $(\bar{\ })$, denoting subgrid scale

Abbreviations

A_c	altocumulus
APE	available potential energy
AW	alpha-omega term representing the conversion of APE
C_i	cirrus
DADT	quasi-Lagrangian time rate of change of A
DAREAA	change in A due to the change in the horizontal area of the storm volume
DAREAK	change in K due to the change in the horizontal area of the storm volume
DEDT	change in A due to time rate of change in ε-field
DKDT	quasi-Lagrangian time rate of change of K
DPSA	change in A due to change in the surface pressure
DPSK	change in K due to change in the surface pressure
DPR	sum of DPRDT, HAPR and VAPR
DPRDT	change in A due to time rate of change in p_r^{κ}
EAW	epsilon-alpha-omega term representing the effect of thermal circulation on A
EHAT	effect of horizontal advection of temperature weighted by the efficiency factor
EVAT	effect of vertical advection of temperature weighted by the efficiency factor

GA	generation of A by non-frictional diabatic processes
GAL	generation of A by total latent heat release
GALS	generation of A by stable latent heat release
GALC	generation of A by convective latent heat release
GAR	generation of A by radiational heating
GAS	generation of A by sensible heat transferred from the ocean
GK	generation of K by cross-contour flow
HAPR	change in A due to horizontal advection of p_r^κ
HFA	horizontal flux of A
HFK	horizontal flux of K
IE	internal energy
KE	kinetic energy
PE	potential energy
RA_I	residual of APE budget I
RA_{II}	residual of APE budget II
RH_c	critical relative humidity
RK	residual of KE budget
S_c	stratocumulus
TPE	total potential energy
VAPR	change in A due to vertical advection of p_r^κ
VFA	vertical flux of A
VFK	vertical flux of K

CHAPTER I

INTRODUCTION

Extratropical disturbances form most readily in the strong baroclinic region near the jet stream (Palmen and Newton, 1969). According to Petterssen (1950), two major cyclone tracks exist in the northern hemisphere during winter season, from the southwestern to the northeastern parts of the Pacific and Atlantic oceans. The regions where these cyclones originate are coincident with the areas where observations indicate that a considerable amount of sensible heat and moisture are transferred from the ocean to the atmosphere during winter (e.g., Ninomiya, 1972). With the development of baroclinic instability theory, the current viewpoint is that extratropical cyclones are manifestations of the adiabatic release of the zonal available potential energy (Johnson, 1970). Observational studies, such as those by Oort (1964) and Dutton and Johnson (1967), also show that the energy cycle of the general circulation (Fig. 48) proceeds on the average from zonal available potential energy via eddy available potential energy and eddy kinetic energy to, finally, the zonal kinetic energy. These eddies can be identified as cyclones and/or anticyclones.

Petterssen's statistical evidence showing that cyclogenetic areas are usually regions where sources of either sensible heat or moisture exist has not been satisfactorily explained.

Many of the past studies on the available potential energy budget of cyclones have emphasized the generation effect of the diabatic processes. Several such studies were accomplished at the University of Wisconsin. Some of the results are included in Table 1. An objective at the University of Wisconsin has been to test the hypothesis that the generation of available potential energy by diabatic processes in large scale disturbances is a significant source of energy for the development and maintenance of cyclones. Their strategy was to compare the magnitudes of the _in situ_ generation and the frictional dissipation in the planetary boundary layer. As summarized by Johnson (1970), all of the results support the hypothesis that the _in situ_ generation of available potential energy at the storm* scale is sufficient 1) to offset a significant portion of the storm's kinetic energy dissipation in the planetary boundary layer, 2) to imply that, at least during the mature stage, the storm may be energetically self-sufficient, and 3) to suggest that diabatic heating is an important factor in determining the storm's transient behavior during its growth, maturation and decay.

These conclusions are questionable since not all the

---

*The terms storm and cyclone will be used interchangeably.

sources and sinks of the available potential and kinetic energy are considered. A comparison between the generation of available potential energy by diabatic processes and the frictional dissipation in the planetary boundary layer is not sufficient to assess the importance of diabatic processes in cyclone development. An evaluation of the budget of available potential energy, which includes various sources and sinks is required if any conclusion on the role of diabatic processes is to be drawn.

The Air Mass Transformation Experiment (AMTEX), a subprogram of the Global Atmospheric Research Program (GARP), was carried out over the East China Sea during 14-28 February 1974 and 1975. One of the scientific objectives was to determine the relationship between the development of both mesoscale and synoptic scale disturbances and the amount of energy supplied from the sea surface during air mass modification (GARP Publication Series No. 13, 1973). The goal of the present research is to examine this relationship using an energetics approach. The cyclone, which developed over the East China Sea on 13 February 1975 and subsequently moved in a northeastward direction, will be used as a case study. Hereafter it will be referred to as the AMTEX storm.

The specific objective of this study is to evaluate the sources and sinks of the AMTEX storm's available potential and kinetic energy in a quasi-Lagrangian frame for areas of approximately 6 x 10^6 km^2. Two formulations of the available potential energy budget are utilized, one by Vincent and Chang (1973) and the other by Edmon (1978). Since the resolution is limited by the size of the grid mesh, all of the subgrid scale processes are evaluated as a residual. The importance of diabatic processes in the cyclone development will be judged by the magnitude of the generation of the storm's available potential energy. If the magnitude is relatively small, it will be concluded that the diabatic heating or cooling is not as important as other processes in the immediate development of the AMTEX storm.

The concept of available potential energy and the energy budget equations will be discussed in the next chapter. In Chapter III, the data source and the synoptic background of the AMTEX storm are described. The methodology and the estimated diabatic heating rates are given in Chapter IV. A detailed discussion of the results is presented in Chapter V, and Chapter VI contains the summary and concluding remarks. The notations and abbreviations are explained in the List of Symbols. Those symbols which are often used in the meteorological literature will not be redefined in the following discussion.

CHAPTER II

THE ENERGY BUDGET EQUATIONS

1. The Concept of Available Potential Energy

The forms of energy which play a significant role in atmospheric energetics are kinetic energy (KE), potential energy (PE), and internal energy (IE). If a distinction is made between the thermal and latent forms of IE, the processes of evaporation and melting and the reverse processes of condensation and freezing convert thermal IE into latent IE, and vice versa. In particular, evaporation from the ocean surface removes thermal IE from the ocean and adds latent IE to the atmosphere. It is possible, however, not to include latent IE as a form of atmospheric energy, provided that the release of latent heat is treated as a form of diabatic heating, rather than an internal quasi-adiabatic processes. If this convention is adopted, the atmosphere will be assumed to gain IE not when water evaporates from the ocean, but when the water subsequently condenses within the atmosphere. This allows the energetics of the atmosphere to be treated separately from the ocean (Lorenz, 1967).

The atmospheric KE, PE and IE per unit mass are $\frac{1}{2}\mathbb{V}\cdot\mathbb{V}$, gz and c_vT, respectively. Under hydrostatic equilibrium, the ratio PE/IE for a column of air extending from the surface to the top of the atmosphere is constant and equal to $R/c_v (\sim 2/5)$, and therefore, PE and IE increase or decrease together. The sum of the two is referred to as the total potential energy (TPE). Let π denote TPE, thus,

$$\begin{aligned}\pi &= \int_0^\infty \rho g z \, dz + \int_0^\infty \rho \, c_v T \, dz = \int_{p_s}^0 - z \, dp + \int_0^\infty \rho \, \chi z \, dz + \int_0^\infty \rho \, c_v T \, dz \\ &= \int_0^\infty \rho \, R T \, dz + \int_0^\infty \rho \, c_v T \, dz + \int_0^\infty \rho \, \chi z \, dz \\ &= \int_0^\infty \rho \, c_p T \, dz + \int_0^\infty \rho \, \chi z \, dz \ , \qquad (1)\end{aligned}$$

where $\chi (= g + \frac{1}{\rho} \frac{\partial p}{\partial z})$ is the deviation from the hydrostatic balance, and the boundary conditions $p = p_s$ at $z = 0$ and $p = 0$ at $z = \infty$ are applied in the integration by parts. Since the computations in this study are for the synoptic scale, hydrostatic balance will be assumed. Therefore, the last integral in (1) vanishes. Note that it is meaningless to speak of TPE at a particular point, but within a vertical column the average amount of TPE per unit mass is given by the average value of $c_p T$, which is simply the sensible heat per unit mass.

The pressure p, density ρ and potential temperature θ of any natural state of the atmosphere are assumed to be differentiable (and hence continuous) functions of x, y, z and t. In addition, $\frac{\partial \theta}{\partial z}$ is assumed to be continuous and positive above the ground. Therefore θ is a continuous, one-to-one function of height z. Approaching the top of the atmosphere, the density and pressure are assumed to decrease at a much faster rate than the rate at which temperature increases. If θ_T denotes the potential temperature at the top of the atmosphere, then $\theta_T = \infty$ and $p(\theta_T) = \rho(\theta_T) = 0$.

Lorenz (1955) introduced an ingenious convention which avoids the necessity of determining the equation of the earth's surface in isentropic coordinates. This is accomplished by defining the pressure on an isentrope which intersects the earth and goes "underground" as the pressure at the surface. Therefore, $\frac{\partial z}{\partial \theta}$ can be defined to be zero (i.e., $\frac{\partial \theta}{\partial z} = \infty$) over the underground portion of any isentrope.

The concept of available potential energy (APE) is based on the principle of conservation of mass and on the idealization that flows which conserve specific entropy may exist. Under these conditions, the sum of the internal, potential and kinetic energies is a constant. Therefore, a state of the atmosphere which possesses a minimum of total potential energy will likewise have a maximum of kinetic energy.

The available potential energy is defined to be the difference between the TPE of the natural state and that of the reference state; the reference state being a horizontally invariant and statically stable density distribution achieved by isentropically redistributing the mass in the natural state without any boundary work done to or advection into the system.

The TPE of this reference state is a minimum (Appendix A). Hence the kinetic energy of the isentropic flow leading to the reference state assumes a maximum value. The difference between this maximum amount of KE and the KE of the natural state is equivalent to the available potential energy.

Conceptually the reference state can be attained by imposing a vertical motion field which moves the originally undulating isentropic surfaces into coincidence with the earth's geopotential surfaces. Thus, all thermodynamic variables will be constant on the geopotential surfaces. The redistribution process preserves the distribution of mass with respect to potential temperature. The surface potential temperature in the reference atmosphere, i.e. θ_r at $H = 0$, will be the lowest potential temperature θ_0 of the natural state, and the potential temperature θ_T at the top of the reference atmosphere will be the highest found in the natural state.

The mass per unit area contained between the isentropic surfaces with values θ_0 and θ in the reference state is,

$$\int_{o}^{H(\theta)} \rho_r(z)\,dz = \int_{\theta_o}^{\theta} \rho_r \frac{\partial H}{\partial \psi}\,d\psi \ , \tag{2}$$

and in the natural state it is

$$\frac{1}{\sigma}\int_{\theta_s}^{\theta}\int \rho \frac{\partial h}{\partial \psi}\,d\sigma\,d\psi = \int_{\theta_o}^{\theta} \langle \rho \frac{\partial h}{\partial \psi} \rangle\,d\psi \ , \tag{3}$$

where H and h represent the height in the reference state and the natural state, respectively, ψ is a dummy variable, subscript s denotes surface, σ is the horizontal area of the system of interest, and the careted brackets defined by

$$\langle(\ )\rangle \equiv \frac{1}{\sigma}\int(\ )_\theta d\sigma ,$$

denote the ratio of an integral over an isentropic surface to σ. The assumption that $\frac{\partial h}{\partial \theta}$ vanishes on underground isentropes is used in (3), which ensures that the portion of the integral from θ_0 to θ_s makes no contribution. The definition of the reference state requires (2) and (3) to be equal;

$$\int_{\theta_o}^{\theta} \rho_r \frac{\partial H}{\partial \psi}\, d\psi = \int_{\theta_o}^{\theta} \langle\rho \frac{\partial h}{\partial \psi}\rangle\, d\psi . \tag{4}$$

Differentiation of (4) with respect to θ gives,

$$\rho_r \frac{\partial H}{\partial \theta} = \langle\rho \frac{\partial h}{\partial \theta}\rangle . \tag{5}$$

Eq. (5), combined with the hydrostatic equation for the reference state,

$$\frac{\partial p_r}{\partial \theta} = -\rho_r g \frac{\partial H}{\partial \theta} , \tag{6}$$

gives,

$$p_r(\theta) = g\int_{\theta}^{\theta_T} \langle\rho \frac{\partial h}{\partial \psi}\rangle\, d\psi = -\int_{\theta}^{\theta_T} \langle\frac{\partial p}{\partial \psi}\rangle\, d\psi . \tag{7}$$

Having determined the pressure and potential temperature of the reference atmosphere, all other thermodynamic variables may be derived. Therefore, the structure of the reference state can be uniquely and explicitly determined from the natural state of the atmosphere (Dutton and Johnson, 1967).

Computationally, the reference pressure in (7) is the average pressure on an isentropic surface in the natural state. When an isentrope intersects the ground, the convention that $\frac{\partial h}{\partial \theta}$ vanishes allows the surface pressure to be used in the averaging procedure and guarantees the conservation of mass. Therefore, at the surface $(H = 0)$ of the reference atmosphere the pressure is the average of the surface pressure in the natural state, denoted by $\overline{p_s}$, and at the top $(H = \infty)$ the pressure is zero.

2. The Amount of Available Potential Energy

To evaluate its energetics, the system of interest must extend from the earth's surface to the top of the atmosphere and its lateral boundaries must be vertical. The dimensional constraints are implied by the definition of TPE and the hydrostatic specification of the reference atmosphere. The TPE per unit area, π, of such a system is,

$$\pi = \frac{c_p}{\sigma g}\iint_0^{p_s} T \, dp \, d\sigma = \frac{c_p}{\sigma}\iint_{\theta_0}^{\infty} \rho \, T \, J \, d\theta \, d\sigma \ , \tag{8}$$

in p and θ coordinates, respectively. J, equal to $\frac{\partial h}{\partial \theta}$, is the transformation Jacobian between the height and isentropic coordinates. Since the structure of the reference atmosphere can be explicitly determined, the TPE per unit area, π_r, is,

$$\pi_r = \frac{c_p}{g}\int_0^{\overline{p_s}} T_r \, dp_r = c_p\int_{\theta_0}^{\infty} \rho_r \, T_r \, J_r \, d\theta_r \ , \tag{9}$$

where $J_r = \frac{\partial H}{\partial \theta}$. Van Mieghem (1956) used a variational approach to show that π_r in (9) is indeed a relative minimum (Appendix A) and is the part of TPE which is unavailable for conversion to KE. The available potential energy per unit area therefore is,

$$A = \pi - \pi_r \ . \tag{10}$$

Substituting for T_r in (9) from Poisson's equation gives,

$$\pi_r = c_p \int_{\theta_o}^{\infty} \theta_r \left(\frac{p_r}{1000}\right)^{\varkappa} \rho_r \frac{\partial H}{\partial \theta_r} d\theta_r \ , \tag{11}$$

where $\varkappa$ is R/c_p. Since θ_r is a dummy variable, it may be replaced by θ. Therefore,

$$\pi_r = c_p \int_{\theta_o}^{\infty} \theta \left(\frac{p_r}{1000}\right)^{\varkappa} \rho_r \frac{\partial H}{\partial \theta} d\theta \ . \tag{12}$$

Substitution of (5) into (12) gives,

$$\pi_r = c_p \int_{\theta_o}^{\infty} \theta \left(\frac{p_r}{1000}\right)^{\varkappa} \langle \rho \frac{\partial h}{\partial \theta} \rangle \, d\theta = \frac{c_p}{\sigma} \iint_{\theta_o}^{\infty} \rho\, \theta \left(\frac{p_r}{1000}\right)^{\varkappa} \frac{\partial h}{\partial \theta} \, d\theta \, d\sigma$$

$$= \frac{c_p}{\sigma} \iint_{o}^{\infty} \rho\, \theta \left(\frac{p_r}{1000}\right)^{\varkappa} dz \, d\sigma = \frac{c_p}{\sigma g} \iint_{o}^{p_s} \theta \left(\frac{p_r}{1000}\right)^{\varkappa} dp \, d\sigma \ . \tag{13}$$

Note that the physical meaning of π_r has changed from (9) to (13). Having redistributed the mass, π_r in (9) is expressed in the frame of the reference atmosphere. The reference pressure is only a function of the potential temperature. For each particle in the natural state, the pressure value in the reference state is known if θ is known. Therefore, the contribution to π_r from each particle in the natural state is $c_p \theta \left(\frac{p_r}{1000}\right)^{\varkappa}$.

Summing up all the contributions in the frame of the natural state gives the expression in (13). This formulation allows $\pi - \pi_r$ in (10) to be combined and A expressed in one term.

$$A = \frac{c_p}{\sigma g}\iint_0^{p_s} \theta\left(\frac{p}{1000}\right)^{\varkappa} - \theta\left(\frac{p_r}{1000}\right)^{\varkappa} dp\, d\sigma$$

$$= \frac{c_p}{\sigma g}\iint_0^{p_s} \left[1 - \left(\frac{p_r}{p}\right)^{\varkappa}\right]T\; dp\, d\sigma = \frac{c_p}{\sigma g}\iint_0^{p_s} \varepsilon T\, dp\, d\sigma\ , \qquad (14)$$

where ε is often called the efficiency factor, which specifies how efficiently diabatic processes generate or destroy APE on an isentropic surface. Areas where the pressure is higher than the isentropic average will yield a positive efficiency factor; on the other hand, where the pressure is lower than the isentropic average, the efficiency factor will be negative.

The use of isentropic coordinates in the theory of available potential energy is conceptually simple since isentropic redistribution of mass is called for in the definition of the reference state. However, isobaric coordinates are chosen for this research since the data available are in isobaric coordinates.

3. The Time Rate of Change of APE and KE for an Open Quasi-Lagrangian System

For an energetics study, the choice of the horizontal extent of a system varies depending on the objective of the research. In general circulation studies, the entire atmosphere can be considered approximately as a closed system. For a large scale cyclone, the system may be one that includes most of the important synoptic and dynamic features. The system should be considered open because of the fluxes and work occurring at the boundaries. Johnson (1970) illustrated that the same diabatic process might generate or destroy a storm's APE and global APE by different amounts, and sometimes even have opposite effects. Therefore, it is difficult to infer the role of the diabatic processes in the energetics of a storm if the global system is used. Since the major concern of this research is on the energetics of a developing storm, rather than the contribution of the storm to the global energetics, an open system is chosen and will be referred to as the "storm volume." Since the AMTEX storm moved rapidly, it is desirable to let the storm volume follow the storm instead of being fixed in space. The details used to specify the moving storm volumes will be described in Chapter III.

Any meteorological variable ψ can be decomposed into two parts, $\overline{\psi}$ and ψ'. The overbared quantity is a spatial average defined by

$$\overline{\psi}(x,y,p) = \frac{1}{\Delta x\,\Delta y\,\Delta p}\int_{x-\frac{\Delta x}{2}}^{x+\frac{\Delta x}{2}}\int_{y-\frac{\Delta y}{2}}^{y+\frac{\Delta y}{2}}\int_{p-\frac{\Delta p}{2}}^{p+\frac{\Delta p}{2}} \psi\,dx\,dy\,dp\ ,$$

where Δx, Δy and Δp are the grid spacing in the x, y and p directions, respectively. The primed quantity is the deviation of ψ from $\overline{\psi}$. It is easily seen that $\overline{\psi'} = 0$. Due to discrete sampling, atmospheric information is not available in a continuous form. The value at each grid point is often assumed to be representative of a spatial average. The atmospheric motion, therefore, can be divided into two parts. The part defined by grid point numbers will be called the grid scale, and the part which may occur in nature but cannot be resolved by the grid will be called the subgrid scale.

Two formulations of the APE budget and one of the KE budget will be discussed below. The derivation of the budget equations and the decomposition of the grid and subgrid scale processes are included in Appendix B. Since the subgrid scale processes cannot be directly computed, they are grouped together and evaluated as the "residual" of the grid scale terms. The overbars will be omitted in the following discussion for convenience. Therefore, all the variables represent the grid scale unless otherwise stated.

Following Vincent and Chang (1973), the time rate of change of the grid scale APE for a moving storm volume, hereafter referred to as APE budget I, is,

$$\begin{aligned}\frac{\delta A}{\delta t} = & -\frac{A}{\sigma}\frac{\delta\sigma}{\delta t} + \frac{1}{\sigma g}\int \varepsilon Q\,dV + \frac{1}{\sigma g}\int \alpha\omega\,dV - \frac{c_p}{\sigma g}\int \frac{T}{p^{\varkappa}}\frac{\delta p_r^{\varkappa}}{\delta t}\,dV \\ & - \frac{c_p}{\sigma g}\int \frac{T}{p^{\varkappa}}(\mathbb{V} - \mathbb{W})\cdot\nabla p_r^{\varkappa}\,dV - \frac{c_p}{\sigma g}\int \frac{T}{p^{\varkappa}}\omega\frac{\partial p_r^{\varkappa}}{\partial p}\,dV - \frac{c_p}{\sigma g}\int \nabla\cdot[\varepsilon T(\mathbb{V} - \mathbb{W})]\,dV \\ & - \frac{c_p}{\sigma g}\int \frac{\partial}{\partial p}(\varepsilon T\omega)\,dV + \frac{c_p}{\sigma g}\int \varepsilon_s T_s \frac{\delta p_s}{\delta t}\,d\sigma + RA_I\,, \qquad (15)\end{aligned}$$

where $\frac{\delta}{\delta t}$ is the quasi-Lagrangian time rate of change, $\frac{1}{g}\int(\ )\,dV$ is the mass integration within the storm volume, and $\mathbb{W}$ and $\tilde{\omega}$

are, respectively, the horizontal and vertical velocity at which the storm volume moves. Symbolically, (15) may be written as

$$\text{DADT} = \text{DAREAA} + \text{GA} + \text{AW} + \text{DPRDT} + \text{HAPR} + \text{VAPR} + \text{HFA} + \text{VFA} + \text{DPSA} + \text{RA}_I \,, \qquad (16)$$

where DADT is the quasi-Lagrangian time rate of change of A, DAREAA is the change in A due to the change in the horizontal area of the storm volume, GA is the generation of A due to non-frictional diabatic heating Q, AW is the conversion of A due to the vertical re-distribution of mass, DPRDT is the effect of the time rate of change of p_r^{κ}, HAPR and VAPR are, respectively, the effects of the horizontal and vertical advection of p_r^{κ}, HFA and VFA are, respectively, the horizontal and vertical fluxes of A, DPSA is the change in A due to changes in the surface pressure, and finally RA_I is the residual of (15). Notice that the signs of symbolic terms are positive when the effects on the budget are to increase A, and vice versa.

The generation of APE (GA) by non-frictional diabatic heating may be further divided into contributions from latent heat release (GAL), from sensible heat addition (GAS), and from radiational heating (GAR),

$$\text{GA} = \text{GAL} + \text{GAS} + \text{GAR} \,. \qquad (17)$$

The methods used to estimate the individual heating rates are discussed in Chapter IV. The net effect of vertical motion in air with different densities is revealed by the term AW, which is the integration of $\alpha\omega$ throughout the mass in the storm volume. Negative AW indicates warmer air rising or colder air sinking, and therefore the release of APE. The APE is stored when AW is positive. Recall that A is a quantity defined for a system with certain constraints, and ε and p_r are assigned values only within the system. The physical meaning of the flux of APE and advection of $p_r^{\varkappa}$ is vague. The flux of APE represents a transfer of energy between the storm volume and its environment by boundary processes. The terms HAPR and VAPR represent the effect of advection in altering the mass-potential temperature distribution. The sum of DPRDT, HAPR and VAPR will be referred to as DPR, where

$$\text{DPR} = -\frac{c_p}{\sigma g}\int \frac{T}{p^{\varkappa}}\frac{dp_r^{\varkappa}}{dt}\,dV \ . \qquad (18)$$

The computed RA_I consists of all the subgrid scale processes and the errors on the grid scale, accumulated through observation, objective analyses, finite differencing, etc.

Edmon (1978) argued that AW and VAPR were nearly equal in magnitude and opposite in sign, and that the magnitudes were usually much larger than those of the other terms in (16). He contends that the generation of APE (GA) is an important term in the budget equation, but is small compared to AW or VAPR. Therefore, he proposed a new formulation in which the terms would be of similar magnitude and the magnitudes would be comparable to those in the KE budget equation. His formulation, hereafter referred to as APE budget II, is

$$\frac{\delta A}{\delta t} = -\frac{A}{\sigma}\frac{\delta \sigma}{\delta t} + \frac{1}{\sigma g}\int \varepsilon Q \, dV + \frac{1}{\sigma g}\int \varepsilon \alpha \omega \, dV - \frac{c_p}{\sigma g}\int \varepsilon (\mathbf{V} - \mathbf{W}) \cdot \nabla T \, dV$$

$$- \frac{c_p}{\sigma g}\int \varepsilon \omega \frac{\partial T}{\partial p} \, dV + \frac{c_p}{\sigma g}\int T \frac{\delta \varepsilon}{\delta t} \, dV + \frac{c_p}{\sigma g}\int \varepsilon_s T_s \frac{\delta p_s}{\delta t} \, d\sigma + RA_{II} , \quad (19)$$

or symbolically,

$$\text{DADT} = \text{DAREAA} + \text{GA} + \text{EAW} + \text{EHAT} + \text{EVAT} + \text{DEDT}$$

$$+ \text{DPSA} + RA_{II} , \quad (20)$$

where DADT, DAREAA, GA and DPSA are the same as those in (16), EAW is the change in A due to the thermal circulations, EHAT and EVAT are, respectively, the effects of the horizontal and vertical thermal advection, weighted by the efficiency factor, DEDT is the change in A due to changes in the ε-field, weighted by the temperature, and RA_{II} is the residual of (19).

Along an isentrope, a region with a positive efficiency factor is warmer than a region with a negative efficiency factor. The function $\varepsilon \alpha \omega$ represents the distribution of direct and indirect thermal circulations. $\varepsilon \alpha \omega$ is negative for direct thermal circulation, i.e., warmer air rising ($\varepsilon > 0$, $\omega < 0$) or colder air sinking ($\varepsilon < 0$, $\omega > 0$), and vice versa. APE is released when EAW is negative and generated when EAW is positive. Since the efficiency factor is usually of the order of 10^{-1} or 10^{-2}, EAW is generally one to two orders of magnitude smaller than AW. The advection within the storm volume, which alters the thermal distribution, has a definite influence on the APE, as illustrated by EHAT and EVAT. The term DEDT is equivalent to the term DPRDT in APE budget I (Appendix B). It is the effect of the time rate of change in the mass-potential temperature distribution within the whole system.

The analytical forms of budgets I and II, i.e., the continuous functions which describe all scales of motion, are shown to be equivalent in Appendix B. Since the physical processes are grouped together differently, there is no reason to assume equivalence for the grid scale and subgrid scale counterparts. In other words, RA_I and RA_{II} are not necessarily equal.

Let K represent the amount of KE within the storm volume divided by the horizontal area,

$$K = \frac{1}{\sigma g}\int k \, dV \ ,$$

where $k = \frac{1}{2}\mathbf{V}\cdot\mathbf{V}$. The quasi-Lagrangian time rate of change of K is,

$$\frac{\delta K}{\delta t} = -\frac{K}{\sigma}\frac{\delta\sigma}{\delta t} - \frac{1}{\sigma g}\int \mathbf{V}\cdot\nabla\Phi \, dV - \frac{1}{\sigma g}\int \nabla\cdot[k(\mathbf{V} - \mathbb{W})] \, dV$$

$$- \frac{1}{\sigma g}\int \frac{\partial}{\partial p}(k\omega) \, dV + \frac{1}{\sigma g}\int k_s \frac{\delta p_s}{\delta t} \, d\sigma + RK \ . \qquad (21)$$

When written in symbolic form, it is

$$DKDT = DAREAK + GK + HFK + VFK + DPSK + RK \ , \qquad (22)$$

where DKDT is the quasi-Lagrangian time rate of change of K, DAREAK is the change in K due to the change in the horizontal area of the storm volumes, GK is the production of K by cross-contour flow, HFK and VFK are, respectively, the horizontal and vertical fluxes of K, DPSK is the change in K due to changes in the surface pressure, and RK is the residual of (21). Besides the subgrid scale processes and errors accumulated in other terms, RK also includes the frictional dissipation of both grid and subgrid flow.

For an open system the production of KE is not necessarily realized from the store of APE within the system, and the release of APE is not necessarily converted to KE within the system. For all scales of motion,

$$\frac{1}{g}\int \alpha\,\omega\,dV - \frac{1}{g}\int \mathbb{V}\cdot\nabla\phi\,dV = -\frac{1}{g}\int \left[\nabla\cdot(\mathbb{V}\phi) + \frac{\partial}{\partial p}(\omega\phi)\right]dV\ . \qquad (23)$$

The term on the right-hand side is the negative of the pressure work which a system exerts on its environment. It is zero for a closed system. For an open system, it is negative if the system expands and positive if the system contracts. Due to the subgrid scale processes, actual computation of the quantities in (23) may not yield an equality relationship. Although the EAW term in (19) is related to the conversion of APE, there is no explicit expression for connection with the KE budget.

An energy diagram for the grid and subgrid scale APE and KE can be constructed in a fashion similar to the energy diagram for the zonal and eddy APE and KE (Fig. 48) which is often seen in association with the energetics of the general circulation. This diagram (Fig. 2) summarizes the APE budget I and the KE budget. All of the grid scale processes can be directly computed. The dashed line between the conversion of APE (AW) and the generation of KE (GK) symbolizes the boundary work which often exists in open systems. The residuals, RA_I and RK, represent the energy transfer between the grid and subgrid scale APE and KE, respectively.

The results of the two APE and one KE budgets for the AMTEX storm are presented in Chapter V.

CHAPTER III

DATA AND SYNOPTIC REVIEW

The gridded fields of various parameters used in this research were prepared and analyzed by Soliz (1977). They include surface pressure, height, temperature, dewpoint depression, sea-surface temperature and three dimensional wind velocities. They are available from 0000 GMT 13 February to 1200 GMT 15 February 1975 at 12-hour intervals. Horizontally, the analyses cover a 31 X 41 grid mesh (Fig. 3) which is a subset of the octagonal grid (polar stereographic map projection true at 60°N) used by the Air Force Global Weather Central (AFGWC). A grid spacing of 190.5 km is used. Vertically, the analyses are available at the following levels: surface, 850, 700, 500, 400, 300, 250, 200, 150 and 100 mb. Marked in Fig. 3 are the positions of the upper air and some of the surface observations utilized in the objective analyses. The upper air data include radiosonde observations and reports from military aircraft. The surface data consist of observations from land stations and transient ships. Most of the data are obtained from the AFGWC data base. Portions are provided by the AMTEX.

Soliz used a variational approach (Sasaki, 1970) to do the objective analyses. Several constraints were applied. One of these was the pattern conservation technique described by Baxter (1975). This technique simulates some of the thought processes of a good human analyst. Given a first guess field which may be a forecast or a recent analysis, an analyst will usually evaluate the quality of the data and try to fit the reasonable ones to the first guess fields while attempting to preserve the maximum and minimum, shapes of the contours, and magnitudes of the gradients. Besides the pattern conservation constraint, variational algorithms insured hydrostatic balance, mass continuity and the inertial stability.

There are always limitations in objective analyses imposed by the density, resolution and accuracy of the data, as well as the ability of the data assimilation procedure. The comparison made by Soliz among the vertical motion fields from different sources and the synoptic features indicates that the major features are realistic.

The observations on the original weather maps may help the synoptic discussion more than a display of the objective analyses. Therefore, the analyses of 500-mb height at 1200 GMT and the analyses of surface pressure at 0000 and 1200 GMT for February 13-15, analyzed by the Japan Meteorological Agency, are presented in Figs. 4-12.

Prior to the development of the AMTEX storm there was an intense 500-mb trough centered over the extreme western section of the Sea of Okhotsk (50°N, 145°E). This upper level low persisted through the intensifying and mature stages of the surface cyclone. At 1200 GMT 11 February, there was a short wave embedded in the westerly flow to the south of the Tibetan Plateau (not shown). It was around 90°E and extended from 20°N to 30°N, and was traveling eastward at roughly 10° per day. At 1200 GMT 13 February, the axis was situated from 20°N, 108°E to 30°N, 110°E (Fig. 4). At the same time, a weak surface low (Fig. 8) emerged on a weak, diffuse stationary front undergoing frontolysis. Its position was approximately at 24°N and 123°E, just to the east of Taiwan. Its central pressure was 1012 mb. This trough system had a westward tilt toward the colder air from the surface to 500 mb. The tilt between the surface and 850 mb was a lot more than that between 850 mb and 500 mb.

The low center at the surface first moved northeastward to an area northwest of Okinawa at 0000 GMT 14 February (Fig. 9), with a central pressure drop of 10 mb in 12 hours. It then curved east-northeastward to 30°N, 135°E at 1200 GMT 14 February (Fig. 10), deepening to 996 mb. A widespread area of precipitation was observed in the two northern quadrants of the storm. Convective activity was also observed along the cold front as it moved across the southwest Japanese islands. Strong cold air advection behind the cold front extended up to 700 mb. The 500-mb short wave was already off the China coast.

During the next 24 hours, the storm moved toward the northeast again and assumed a faster speed (Figs. 11 and 12), deepening rapidly. The central pressure decreased to 980 mb at 0000 GMT 15 February (an average rate of 1.3 mb hr^{-1}), and to 956 mb at 1200 GMT 15 February (an average rate of 2 mb hr^{-1}). Surface winds were around 50 knots near the storm center. The 500-mb short wave seemed to be in phase with the long wave trough, and the trough axis was around 142°E.

As the surface cyclone continued its northeastward path, the central pressure attained a minimum of 952 mb at 0000 GMT 16 February and started filling at 1200 GMT. The storm reached a point south of the Aleutian Islands at 0000 GMT 17 February (not shown). The change in the surface central pressure shown in Fig. 13 attests to the intensity of the storm. Only the period from 0000 GMT 13 February to 1200 GMT 15 February is studied here, covering the incipient and intensifying stages of the AMTEX storm.

The selection of the storm volumes is somewhat subjective. It is desirable to include the entire storm at all levels, but the horizontal coverage of the analyses limits the size of the volume. The selection must be a compromise between these considerations. Fig. 14 outlines the storm volumes chosen for this study. The positions of the low centers and fronts at the surface are also indicated for reference. Each storm volume consists of 17 X 17 grid points, covering a square area with about 3000-km map distance along each side. The same number of grid points are chosen at each time for the convenience of handling the horizontal movement of the storm volume. For most of the times, these storm volumes enclose the cyclonic circulation at the surface, the 500 mb vorticity maximum (Fig. 15), and the couplet of upward and downward vertical motion (Fig. 16). The relative positions of the storm volumes and the 300 mb jet streaks as indicated by the objective analysis are also shown in Fig. 17.

CHAPTER IV

DIABATIC PROCESSES

The total diabatic heating rate (Q_T) consists of the latent heat release (Q_L), sensible heat addition from the underlying surface (Q_S), radiational heating (Q_R), and frictional heating (Q_F). Thus,

$$Q_T = Q_L + Q_S + Q_R + Q_F \, . \tag{24}$$

The frictional heating is believed to affect mostly that part of TPE which is unavailable to be converted to KE, and to affect the APE much less (Lorenz, 1967). Therefore only Q_L, Q_S and Q_R are considered here.

Each diabatic process individually deserves much study. Not only are some of the micro-physical mechanisms not well understood, but also the adaptation for large scale motion is somewhat vague. Therefore parameterization and modeling techniques are often used as an alternative. The assumptions made in modeling and the density and quality of data preclude any claim of precision. The intention here is to estimate the sign and rough magnitude of these processes, and to infer their role in the generation or destruction of the storm's APE. The methodology and the calculation of the heating rates will be discussed in this chapter. The implications of these heating rates for the available potential energy budget will be discussed in Chapter V.

1. Latent Heat Release

The latent heat release is often partitioned into two components,

$$\dot{Q}_L = \dot{Q}_{LS} + \dot{Q}_{LC} , \tag{25}$$

where Q_{LS} is the stable and Q_{LC} is the convective component. The stable component results from the condensation caused by large scale lifting, and the convective component represents the effect of subgrid scale cumulus convection on the grid scale motion. The convective component cannot be computed directly, and must be parameterized.

If all the diagnosed condensation is allowed to fall instantly to the ground, the corresponding precipitation rates are,

$$P = P_S + P_C , \tag{26}$$

where,

$$P = - \frac{1}{gL} \int_{P_s}^{o} Q_L \, dp , \tag{27}$$

and L is the latent heat of condensation. Similar relationships may be written for P_S and P_C. One way to evaluate the schemes used for estimating the latent heat release is to compare P with what is actually observed.

Two methods of estimating P_S were tested. One is by Krishnamurti et al. (1973) and the other by Haltiner (1971).

Krishnamurti's method diagnoses condensation when moist air being advected upward achieves a relative humidity higher than a critical value. The heating rate due to this may be written as,

$$Q_{LS} = \begin{cases} -L\omega \dfrac{dq_s}{dp} , \text{ when } \omega<0, \dfrac{dq_s}{dp} > 0 \text{ and } \dfrac{q}{q_s} \geq RH_c , \\ 0 , \text{ otherwise}, \end{cases} \tag{28}$$

where ω is vertical velocity, q is specific humidity and the subscript s denotes saturation. The critical relative humidity RH_c is chosen to be 75% in this study.

The precipitation rate given by Haltiner is,

$$P_S = \frac{1}{g}\int_0^{p_s} - \frac{dq_s}{dt}\, dp = \int_0^{p_s} - \frac{\delta F\omega}{pg}\, dp , \tag{29}$$

where,

$$F = q_s T\left(\frac{LR - c_pR_vT}{c_pR_vT^2 + q_sL^2}\right) . \tag{30}$$

R and R_v are gas constants for dry air and water vapor, respectively. δ is defined as follows:

$$\delta = \begin{cases} 1 , \text{ when } \omega < 0 \text{ and } q/q_s \geq RH_c , \\ 0 , \text{ otherwise} . \end{cases} \tag{31}$$

These formulae are derived from the first law of thermodynamics, Clapeyron's equation and the law of conservation of water vapor. Although they are used here to estimate the precipitation from stratiform clouds, the original formulation contains no such constraint. However, Haltiner did point out that the precipitation equation (29) gives reasonably good results with synoptic scale pressure systems in the middle latitudes, but has been found to be inadequate in areas of convection and especially in tropical systems.

Several dissimilar cumulus parameterization procedures have been developed in the past. Some are related to the moisture convergence at the boundary layer top, some use the convective adjustment technique, and some involve the concept of mass continuity on the cumulus scale. The second group are mostly used in general circulation studies. The third is known as Arakawa's scheme. Edmon and Vincent (1976) applied the schemes of Krishnamurti et al. (1973) and Kuo (1974), from the first group, with some modifications for a case when a tropical storm interacts with an extratropical baroclinic frontal system. Their results showed that Krishnamurti's scheme did not produce reliable patterns of the horizontal coverage of precipitation. Kuo's scheme showed better agreement with observed precipitation rates, although discrepancies still existed in both the magnitude and the horizontal coverage.

Edmon and Vincent's version of Kuo's scheme is selected for this research. Convective condensation occurs when there is both moisture convergence and a deep conditionally unstable layer in the low levels. The net moisture convergence, M_t, into a column of air of unit area is given by,

$$M_t = -\frac{1}{g}\int_0^{p_s} \nabla\cdot(\mathbf{V}q)\,dp - \frac{1}{g}(\omega q)_{p_s} + \rho\, C_D(q_s - q_a)U_a\ , \qquad (32)$$

where the first two terms on the right hand side represent production by the large scale flow and the last term represents production by evaporation from the underlying surface. The estimation of the evaporation will be discussed in the next section of this chapter. The cloud base p_b is assumed to be the base of the first conditionally or absolutely unstable layer. It is not allowed to be higher than 500 mb. The temperature along the moist adiabat from the cloud base is the cloud temperature T_c, which is generally larger than the temperature T of the environment. Where T_c is equal to T, that level is defined to be the cloud top, p_t. Note that this definition may not be realistic due to the "overshooting" often observed. The heating rate Q_{LC} due to convective condensation is,

$$Q_{LC} = \begin{cases} \dfrac{g(1-b)LM_t\mu}{p_b - p_t} \dfrac{T_c - T}{\langle T_c - T \rangle} , & \text{when } M_t > 0 \\ 0 , & \text{when } M_t \leq 0 , \end{cases} \tag{33}$$

where μ is $(\frac{1000}{p})^{\varkappa}$, and b is a parameter indicating the fraction of M_t which is not condensed, but instead, stored in the air to increase the relative humidity. Kuo suggested that the value of b is probably small compared to 1. In the present study it is assumed to be zero. $\langle T_c - T \rangle$ is the average of $T_c - T$ over the cloud depth.

The AMTEX storm traveled mostly over ocean where not many observations are available. Therefore it is not feasible to compare the areal coverage of the estimated and observed precipitation. Instead, the observations at eight stations (Fig. 18) scattered over Japan and the southwest islands are compared with the estimates at the nearest grid points.

The so-called observed precipitation rates were obtained by dividing the total amount of precipitation received within a 12-hour period by 12 hours. The 12-hour period was centered at the time of interest, which is either 0000 or 1200 GMT. The precipitation totals were obtained from 3, 6, 12 and 24 hour precipitation reports. Due to the assembling procedure and the fact that the stations and the grid points do not represent the same points on earth, the observed and estimated precipitation rates are not expected to correspond exactly. A general quantitative agreement is considered adequate.

The results are shown in Tables 2-9. The sky coverage, cloud descriptions and present weather are also recorded for reference. Although the philosophies of Krishnamurti's and Haltiner's methods of estimating the stable latent heat release are very different, it is encouraging to find that the resulting precipitation rates are very similar. Only the ones resulting from Krishnamurti's method are included in the total precipitation rates.

In most cases, when no precipitation is reported and/or when the cloud cover is small, either both the stable and convective precipitation rates are zero, or the stable component is very small, being a few hundredth of a mm hr^{-1}, and the convective component is zero. For the majority of cases when rain occurred, Krishnamurti's and Kuo's schemes are able to diagnose total precipitation rates of similar magnitudes to those observed. When the observed precipitation rates are fairly high, the convective contribution is usually larger than the stable one. However, the observed precipitation rates can sometimes be misleading. One such example occurs at station 47909 at 1200 GMT 13 February (Table 6). Rain was actually reported after this hour. Due to the assembling procedure, the observed precipitation rate at this hour is 1.33 mm hr^{-1}, instead of zero.

Disagreement between the observed and calculated precipitation rates can also be seen. At station 47678 (Table 2), the calculated precipitation rates at 1200 GMT 14 February and 0000 GMT 15 February are much lower than the observed. At station 47909 (Table 6), shower activity was indicated through most of the 14th and 15th, but, the gridded analyses and the parameterization schemes are not able to produce any latent heat release. They also fail to respond to the brief shower activity recorded at 1200 GMT 15 February at stations 47927 (Table 8) and 47918 (Table 9).

Overall, Krishnamurti's, Haltiner's and Kuo's methods of estimating the latent heat release appear to be satisfactory in terms of the vertically integrated effects. Figs. 19-21 show the areal extent of the calculated precipitation rates (P_S and P_C) and the sum of the two (P) for the six moving storm volumes. The precipitation is diagnosed mostly in the vicinity of the surface storm center and along the fronts, with larger amounts occurring at 0000 and 1200 GMT 14 February and 0000 GMT 15 February. The horizontal coverage of the stable component is broader than that of the convective, but the latter has a larger magnitude.

There are a lot of variations in the vertical profiles of the latent heat release (Fig. 22). The convective component is sometimes diagnosed only at one level; the stable latent heat release may occur in a layer deeper than the layer of the convective latent heat release. The maximum of the total latent heat release often occurs at 700 or 500 mb. A similar statement was also made by Vincent, Pant and Edmon (1977). This may be a special feature of the schemes used, and may not be representative of reality.

The vertical distribution of the latent heat release is of special importance to energetics studies. While the total amount of heating may be correct, an incorrect vertical distribution can have an adverse effect on the generation of APE. Unfortunately the vertical distribution of heating in cumulus parameterization schemes is still very uncertain.

The moisture convergence has two sources, one caused by the large scale flow and the other by evaporation from the ocean. For the area covered by the storm volumes, these two parts have similar orders of magnitude, but the large scale moisture convergence is generally a few times larger than the moisture flux from the ocean. At those grid points where latent heat release occurs, the amount of heating is of the order of 5 K day^{-1} for Q_{LS} and 30 K day^{-1} for Q_{LC}.

2. Sensible Heat and Moisture Fluxes From the Ocean

Due to the temperature and moisture differences between the atmosphere and the ocean, turbulent fluxes can transfer heat and water vapor from one to the other, and therefore contribute to air mass modification. The sensible heat addition has a direct effect on the APE budget. The added moisture produces heating only when it condenses.

A practical method for estimating the sensible heat flux F_S and moisture flux E is the bulk aerodynamic method given by

$$F_S = \rho\, c_p C_D(z)[T_s(0) - T_a(z)]U_a(z) \tag{34}$$

and

$$E = \rho\, C_D\,(z)[q_s(0) - q_a(z)]U_a(z)\ , \tag{35}$$

where C_D and U_a are, respectively, the drag coefficient and wind speed at height z, T is the temperature, q is the specific humidity, and subscripts "s" and "a" represent sea and air, respectively. If L represents the latent heat of condensation, the quantity, LE, is also a measure of the moisture flux. LE will be used in the following discussion instead of E.

The choice of height z for the air temperature, specific humidity and wind speed is not very critical since the drag coefficient is adjusted for the appropriate height. A commonly selected height of 10 meters is used. If the quantities in the brackets in (34) and (35) are negative, zero values are assumed for F_S and LE, respectively. Since the percentages of land in the storm volumes are small, zero F_S and LE are also assumed for those grid points which are over land.

Observational results for neutral atmospheric conditions indicate that the functional dependence of the drag coefficient is of the form,

$$C_D(z) = (a + bU_a(z)) \times 10^{-4} \ , \qquad (36)$$

where $U_a(z)$ is in m $\sec^{-1}$, a and b are 11.0 and 0.7, respectively, as suggested by Deacon and Webb (1962). The 10 m wind is estimated from the surface geostrophic wind U_g by a model proposed by Rossby and Montgomery (1935),

$$U_a(z) = \frac{3}{2} \frac{0.0625 U_g}{k} \sin\beta \ln(\frac{z + z_o}{z_o}) \ , \qquad (37)$$

where k is the von Karmen constant (0.4), and β is the angle between the geostrophic wind vector and the surface shear stress, chosen to be 20° in this study. The roughness parameter z_0 is determined from an approximate relation (Roll, 1965),

$$z_0 \simeq z \exp(-k/\sqrt{C_D}) \ . \qquad (38)$$

A first guess of one-half of the geostrophic wind is used for the 10 m wind speed to estimate the drag coefficient by (36), then from (38) and (37), the 10 m wind estimate can be revised by using this drag coefficient. Three or four such iterations are sufficient to achieve a stable estimate of the 10 m wind speed. Thus, the heat and moisture fluxes can be calculated.

One assumption made in the method described above is that the sensible heat and moisture transfer coefficients are equal to the momentum transfer coefficient (i.e., the drag coefficient) in a neutral atmospheric surface layer. Some studies in the past indicated that the heat and moisture transfer coefficients are larger than the momentum transfer coefficient, and those under unstable conditions tend to be larger than those in neutral conditions (e.g., Deardorff, 1968). Although factors such as stability, wave height and roughness parameter may be important in estimating the drag coefficient (Wildman, 1977), no attempt is made here to incorporate these factors because of the limited vertical resolution of synoptic data. As a result, the flux estimates in this study may be conservative.

Shown in Table 10 are estimates of the drag coefficient, sensible and latent heat fluxes and the Bowen ratio, averaged over a small 5 x 7 grid mesh (Fig. 23) containing the Japanese southwest islands, for comparison with other flux computations. A distinct increase in F_S and LE occurred at

1200 GMT 14 February, with the passage of the cold front.

The bulk transfer coefficients calculated by Mitsuta, Mongi and Tsukomoto (1977) using the AMTEX flux measurements are given in Table 11. The authors noted that the scatter about these values was very large, particularly for the heat and moisture fluxes. The drag coefficients computed in this study are in the proximity of those values computed by Mitsuta, Mongi and Tsukomota, larger than their momentum values but smaller than their heat and moisture values.

Several groups of flux estimates made over the AMTEX area are listed in Table 12 for comparison. The AMTEX'75 turbulent flux data (AMTEX'75 Data Report, Vol. 4, 1975) at two island sites, Miyakojima and Taramajima, were determined hourly by the eddy correlation technique during onshore winds. Shown are those averaged from February 14 to 28. Ninomiya's (1972) estimates are those averaged over a 20 day period in February of 1968. Both Agee and Howley (1977) and Amburn (1976) used the data collected during AMTEX'74 and the bulk aerodynamic method with different drag coefficients. The functional form of the drag coefficient used by Agee and Howley and in Amburn's Method 2 was the same as that used in this study, Eq. (36), but in Amburn's computation, a and b were respectively 8 and 1.14 (Sheppard, 1958). In Amburn's Method 3, the drag coefficient was stability dependent (Roll, 1965). Although there is a lot of variation among these estimates, they all have the same order of magnitude except

Amburn's Method 2.

The flux estimates in this study are closest to the measurements at the two island sites. The maximum measurement was around 500 ly day^{-1} for F_S and 1600 ly day^{-1} for LE. The maximum estimates made by (34) and (35) are 1½ to 2 times as large. At some grid points the calculated fluxes seem to vary too rapidly with time, but they are usable for a rough estimate. The averages of the non-zero flux estimates for the moving storm volumes are shown in Table 13.

The heating rate resulting at a particular location is given by the divergence of the sensible heat flux. For horizontal homogeneity and hydrostatic conditions, the heat addition per unit mass is given by

$$Q_S = g \frac{\partial F_S}{\partial p} . \tag{39}$$

Because of the presence of low-level cold air over the warm ocean, a well-mixed boundary layer develops, capped by an inversion. In this mixed layer, the lapse rate is approximately adiabatic and the heating rate due to the sensible heat flux is nearly uniform with height. Therefore, a constant flux divergence will be assumed for the mixed layer.

There is not much choice about the top of the mixed layer because of the coarse vertical resolution of the analyses. The level of 850 mb is chosen for all storm volumes. This is not unreasonable since the upper boundary of the mixed layer on cold air outbreak days during AMTEX'75 was found approximately at 850 mb (Stephens, 1978).

For a typical value of the sensible heat flux, say, 200 ly day^{-1}, the amount of heating produced in the layer between the surface and 850 mb is around 5.4 K day^{-1}.

3. Radiational Heating

Radiative budgets of the troposphere are highly dependent upon the cloud conditions present. Data from climatological studies may not be applicable to a specific case of cyclone development.

Chaplin (1976) performed an objective cloud analysis and calculated the radiation budget of the troposphere over a region enclosing the observational network during AMTEX'74. Clouds were divided into three layers: low (Sc), middle (Ac) and high (Ci). Results indicated that the mean daily total, low, middle and high cloud cover increased on a cold air outbreak day, when compared with those on a warm day. The net radiative loss by an atmospheric column was larger during warm days than cold days. It suggested that the net radiative contribution to air mass modification is a reduction in cooling, or possibly even warming in some instances.

A detailed radiation budget calculation is not within the scope of this research. Instead, a subjective approach is taken. This is by no means precise, but may allow an estimate of the contribution of radiative processes to the development of the AMTEX storm.

Following Chaplin (1976), three cloud layers are assumed. The low clouds extend from 950 to 850 mb, the middle clouds from 700 to 550 mb, and the high clouds from 350 to 300 mb. The cloud distributions for all six storm volumes, shown in Fig. 24, are subjectively analyzed based on the surface observations, satellite photos, dewpoint depression analyses, surface maps from JMA and U.S. Air Force Air Weather Service, and synoptic considerations. The coverage is assumed to be about 75% and uniform.

Based on the computations from Chaplin (1976) and Chaplin and Kimpel (1978), the radiative heating (positive) and/or cooling (negative) rates are estimated from the surface to 100 mb at 50 mb intervals for eight different cloud combinations (Fig. 25). Maximum cooling is assumed to occur in the upper portion of a cloud layer and immediately above. Minimum cooling or even some warming occurs in the lower portion of a cloud layer and immediately below. The region near and above the tropopause is assumed to be approximately in radiative equilibrium if there are no high clouds present (Dopplick, 1972). No adjustment is made for precipitating clouds.

To obtain the heating or cooling rates at the levels used in this study (50 to 200 mb apart), the estimates at 50 mb increments are averaged in appropriate layers in an attempt to capture the extreme features. For example, the cooling rate at 700 mb is $(C_{750}+C_{700}+C_{650}+C_{600}/2)/3.5$.

These new vertical profiles are depicted by the dashed lines in Fig. 25. The average cooling rates for the air column extending from the surface to 100 mb and the layer between the surface and 850 mb are included in Table 14. The magnitude of the average cooling rate from surface to 100 mb is largest for the combination of Sc and Ac, followed successively by Sc, Ac, Sc + Ac + Ci, Sc + Ci, Ac + Ci, clear and Ci.

In summary, the latent heat release has the largest magnitude of the diabatic processes, about 35 K day^{-1}. At those grid points where only sensible heating and radiative cooling apply, the former is the larger of the two, about 5 K day^{-1}. Radiative cooling is comparatively small, about 1 K day^{-1}. Note that radiative heating and cooling apply to all the grid points within the storm volumes, while the sensible heating only extends up to 850 mb at ocean grid points, and latent heating occurs mostly near the storm center and in the lower and middle troposphere.

CHAPTER V

RESULTS

The available potential energy and kinetic energy budgets are evaluated for the AMTEX storm in an open quasi-Lagrangian frame at 12-hour intervals starting at 0000 GMT 13 February and ending at 1200 GMT 15 February 1975. The storm volumes cover horizontal areas of approximately 6×10^6 km^2. Two formulations of the APE budget are used: one by Vincent and Chang (1973) and the other by Edmon (1978), referred to as APE budget I and II, respectively. The results are presented in five sections: the amount of APE and KE, generation of APE, APE budget I, APE budget II and KE budget.

1. The Amount of APE and KE

Shown in Fig. 26 are the total potential energy of the atmosphere within the storm volumes and their respective reference states. The difference between the two, i.e., the APE, is shown in Fig. 27. The amount of APE changed little between 0000 and 1200 GMT 13 February. This is consistent with the fact that the surface low center and closed isobars were not analyzed by JMA until 1200 GMT 13 February. The APE increased significantly at 0000 GMT on the 14th and decreased rapidly afterwards. There are many factors which can affect A. The temporal variation can be better explained after examining the APE budgets.

Also shown in Fig. 27 is the amount of KE within the storm volumes. The variation in K with time is not as large as that in A. K decreased initially, increased at 1200 GMT 14 February, and then decreased again. The amount of kinetic energy is generally expected to increase as a storm system intensifies. The decrease in K of the AMTEX storm can be partially explained by examining the wind-speed distribution in the upper troposphere, e.g., the isotachs at 300 mb (Fig. 17). The position of the jet stream relative to the storm volume is an important factor in the KE budget. More detailed discussions are included in section 4 of this chapter.

The ratios of APE to TPE and KE to APE are also calculated for comparison with those of the general circulation. As shown in Table 15, the ratios of APE to TPE of the AMTEX storm are similar in magnitude to the global value. However, the ratios of KE to APE are significantly larger than the global one, suggesting that the efficiency of the atmosphere as a heat engine is maximized in the vicinity of a developing cyclone.

2. Generation of APE

Before discussing the generation of APE, it is helpful to first examine the distribution of the efficiency factor.

Shown in Fig. 28 are typical cross-sections of the efficiency factor and the potential temperature. The efficiency factor is dependent upon the pressure distribution on an isentropic surface. As the isentropic surface slopes upward toward the cold air in the troposphere, the warmer region usually has a positive efficiency factor and the colder region a negative efficiency factor. The sign is often reversed in the stratosphere. Sometimes the two negative regions are connected and the lower zero isopleth assumes an "s" shape. Recall that the generation of APE due to non-frictional diabatic heating Q is defined (see Eqs. (15) and (16)) as,

$$GA = \frac{1}{\sigma g} \int \varepsilon \, Q \, dV \; .$$

Heating in a region with a positive efficiency factor and cooling in a region with a negative efficiency factor will generate APE; conversely, heating in a region with a negative efficiency factor and cooling in a region with a positive efficiency factor will destroy APE.

The diabatic heating rates discussed in Chapter IV are used in the calculation of generation of APE. The contributions from latent heat release (GAL), sensible heat addition (GAS), and radiational heating (GAR), as well as the total generation (GA) are depicted in Fig. 29. The orders of magnitude are comparable with those obtained in other studies (e.g., Gall and Johnson, 1971; Vincent, Pant and Edmon, 1977; Edmon and Vincent, 1977). GA is positive for the entire study period from 0000 GMT 13 February to 1200 GMT 15 February. The net effect of the diabatic processes on the AMTEX storm, therefore, is to generate APE. The total generation is dominated by the contribution from the latent heat release. The contribution from radiation is very small.

The dominant component generation, GAL, is the sum of the generations by stable and convective latent heat release, denoted by GALS and GALC, respectively. Recall that the stable and convective latent heat release result from the condensation due to large scale lifting and subgrid-scale cumulus convection, respectively. As shown in Fig. 30, GALS and GALC are of similar order of magnitude. GALS increases slowly at 0000 and 1200 GMT 13 February, reaching a maximum at 0000 GMT 15 February, gradually decreases afterwards and is slightly negative at 1200 GMT on the 15th. GALC has an increasing trend from 0000 GMT 13 February to 0000 GMT 15 February, oscillating between 0000 GMT (0900 LST) and 1200 GMT (2100 LST). The oscillation may be a diurnal effect; no firm explanation can be offered at present. There are sharp decreases in GALC and GALS at 1200 GMT 15 February. This is observed in spite of the fact that the central pressure of the surface low did not increase until 1200 GMT 16 February (Fig. 13). These decreases may be attributed in part to the decrease in the amount of latent heat released, and also in part to the fact that some of the condensation occurred in the cold sector, which contributes to the destruction of APE. The energy source provided by condensation at the end of the intensifying stage is much less than at earlier times.

Displayed in Figs. 31-33 are the vertical profiles of horizontally averaged GAL, GAS and GAR. The generation by latent heat release (Fig. 31) maximizes in the middle troposphere, and is zero above 300 mb. The effect of the sensible heat transferred from the ocean is confined within the lowest two layers (Fig. 32), since the top of the mixed planetary boundary layer is chosen at 850 mb. Generation is indicated for most of the layers except at 1200 GMT 14 and 15 February, when small destruction is seen in the layer between 850 and 700 mb. The radiational cooling generally results in generation of APE in the middle and upper troposphere and destruction of APE in the lower troposphere (Fig. 33). The reason for the destruction in the lower troposphere is that the efficiency factors near the surface are mostly positive (Fig. 28).

The horizontal distributions of vertically averaged GAL, GAS and GAR are shown in Figs. 34-36. The condensation near the storm center accounts for most of the generation by latent heat release (Fig. 34). The sensible heat transferred from the ocean generates APE to the south-southeast (warmer side) of the surface low center, but destroys APE to the north-northwest (colder side) (Fig. 35). The reverse is true for the radiational cooling (Fig. 36). This can be explained by the fact that the efficiency factor in the tropopause is generally positive in the warmer region and negative in the colder region.

A major point made above is that the diabatic processes are a source of the AMTEX storm's APE. The magnitude of the generation ranges from 1.5 to 14.0 W m^{-2} (Table 16). The relative importance of the diabatic processes in the cyclone development will be examined in the following sections where the APE budgets will be discussed.

3. APE Budget I

The APE budget I, as defined by Eq. (15) and described symbolically by Eq. (16), is shown in Table 16. The generation of APE by diabatic processes (GA), the vertical flux of APE (VFA), as well as the change in A due to the changes in the horizontal area (DAREAA) and the surface pressure (DPSA) are more than one order of magnitude smaller than the other terms. Therefore, only DADT, AW, HFA, DPRDT, HAPR, VAPR and RA_I are plotted as functions of time in Fig. 37.

An outstanding feature in Fig. 37 is the strong negative correlation between the horizontal flux of APE (HFA) and the term related to the horizontal advection of $p_r^{\varkappa}$ (HAPR). Expanding the del operator in HFA yields

$$HFA = -\frac{c_p}{\sigma g}\int \varepsilon[\nabla\cdot T(\mathbb{V} - \mathbb{W})]\, dV - \frac{c_p}{\sigma g}\int T(\mathbb{V} - \mathbb{W})\cdot\nabla\varepsilon\, dV \quad .(40)$$

As shown by Eq. (B.23), the second term on the right hand side is the same as HAPR except for the opposite sign. The individual mechanisms described by these two terms do not add insight to the discussion of the APE budget I. The sum of HFA and HAPR, however,

$$\mathrm{HFA} + \mathrm{HAPR} = -\frac{c_p}{\sigma g}\int \varepsilon[\nabla\cdot T(\mathbb{V} - \mathbb{W})]\,dV\ , \tag{41}$$

is the effect of the horizontal divergence of the temperature flux within the storm system. As shown in Table 16 and Fig. 37, it is continually a source of the AMTEX storm's APE for the incipient and intensifying stages, ranging in magnitude from 41.3 to 207.1 W m^{-2}.

Aside from the horizontal divergence of the temperature flux described above, term VAPR,

$$\mathrm{VAPR} = -\frac{c_p}{\sigma g}\int \frac{T\omega}{p^{\kappa}}\frac{\partial p_r^{\kappa}}{\partial p}\,dV\ ,$$

which is related to the vertical advection of p_r^{κ}, is also an internal source of the storm's APE for the entire study period. Since p_r depends upon the entire mass-potential temperature distribution within the storm volumes, it is difficult to explicitly state the physical meaning of VAPR. Nevertheless, this term represents the effect of the change in the mass-potential temperature distribution due to the vertical motion. The magnitude of this internal source ranges from 67.7 to 319.4 W m^{-2}.

From Eq. (B.18), the conversion of APE (AW) may be written as

$$\mathrm{AW} = \frac{c_p}{\sigma g}\int \frac{T\omega}{p^{\kappa}}\frac{\partial p^{\kappa}}{\partial p}\,dV\ .$$

The only differences between VAPR and AW are the sign and the differential term within the integral. Since p_r is the average pressure on an isentropic surface, the difference between p_r and p probably is not more than 10%. Therefore, VAPR and AW should have similar magnitude and opposite signs (Edmon, 1978). This is indeed true in this case study.

The APE of the AMTEX storm is converted at a rate ranging from -171.8 to -370.6 W m^{-2}, which is much larger than the conversion rates of the zonal and eddy available potential energy estimated for the general circulation (Fig. 48). As shown in Eq. (23), the APE converted in an open system can be used for either the generation of KE or the pressure work done at the boundaries. The KE of the AMTEX storm is generated at a rate of the order of 10 W m^{-2} (Section 5). Therefore, a large portion of the converted APE is used for the boundary work. The horizontal distribution of vertically averaged AW (Fig. 38) shows positive-negative couplets in the vicinity of the storm, which resembles the pattern of the vertical motion field. The vertical profiles (Fig. 39) show negative values throughout the atmosphere with one or two minima occurring in the middle or upper troposphere.

Another important sink term in the APE budget I is the residual. The grid scale APE is transferred to the subgrid scale at a rate ranging from -50.8 to -197.8 W m^{-2}. If the observational error and the errors accumulated through data manipulation are not significant, the residual in this study suggests the important role played by the subgrid scale in the energetics of large scale cyclones.

The major sources and sinks of the grid scale APE of the AMTEX storm have been discussed. For the 3-day period from 0000 GMT 13 February to 1200 GMT 15 February, the horizontal divergence of the temperature flux contributes to the generation of APE within the storm system at an average rate of 157.5 W m^{-2}, and the change in the mass-potential temperature distribution due to vertical motion contributes at an average rate of 203.9 W m^{-2}. Although the generation of APE by diabatic processes is suspected to be an important energy source for the cyclone development, the present study does not support this hypothesis since it is small compared with the internal sources. The storm's APE is converted to KE and boundary work through large-scale vertical motion at an average rate of -289.2 W m^{-2}, and is transferred to the subgrid scale at an average rate of -143.7 W m^{-2}.

Following are the comparisons made between the APE budget of the AMTEX storm and that of a continental U.S. cyclone (Pant, 1976). The generation of APE by diabatic processes in the latter is 11, 21 and 10 W m^{-2} for the developing and for the mature and occluded stages, respectively. As in the AMTEX storm, it is very small compared to the leading order terms (Fig. 40). There are other similarities. Term DPR, which is the sum of DPRDT, HAPR and VAPR (Eq. (18)), correlated negatively with term HFA. The sum of the two is positive for all three stages, indicating the internal source of APE discussed earlier. The large scale vertical motion is a sink of the cyclone's APE. The average rate of the APE conversion of the continental U.S. cyclone is much larger than that of the AMTEX storm. Part of the reason is that the horizontal area of the storm volumes in Pant (1976) is approximately 1/3 of that in this study; therefore, the intense cyclone activity is more concentrated in the former than in the latter. And, of course, the accuracy of the vertical motion field is also an important factor. The main difference between the two APE budgets is the sign of the residual. The subgrid scale processes are a sink for the AMTEX storm, but a source for the continental U.S. cyclone.

4. APE Budget II

The second formulation of the APE budget, as described by Eqs. (19) and (20), will be discussed in this section. The values of the terms are listed in Table 17 and plotted in Fig. 41. The terms DADT, GA, DAREAA and DPSA are the same as those in budget I. Note that the terms in APE budget II all have similar order of magnitude and that their magnitudes are smaller than the leading order terms in APE budget I.

Unlike APE budget I where the time rate of change of A (DADT) appears to be the small difference between large values, the magnitude of DADT is relatively large in the budget II. A close examination reveals that DADT, DEDT and RA_{II} are in approximate balance for the entire period from 0000 GMT

13 February to 1200 GMT 15 February, with larger discrepancies occurring on the 15th.

Term DEDT is negative at 1200 GMT 14 February and 0000 GMT 15 February and positive the rest of the time. The change in the efficiency factor is a result of the change in the mass-potential temperature distribution within the storm system. Although it is desirable to have a more specific physical explanation, none can be offered at present.

As in the APE budget I, the subgrid scale processes are a sink of the grid scale APE. The average value of RA_{II} for the 3-day period is -60.1 W m^{-2}, which is smaller than the average value of RA_{I}. The trend from one time to the next is the same for RA_{I} and RA_{II}. Moreover, there are notable similarities between the horizontal distributions and vertical profiles of RA_{I} and RA_{II}. The conclusion that the subgrid scale motion plays an important role in the energetics of large scale cyclone is well supported.

The generation of APE by diabatic processes (GA) and the effect of the horizontal and vertical advection of temperature, denoted by EHAT and EVAT, respectively, are sources of the AMTEX storm's APE for the entire study period except at 1200 GMT 15 February, when EHAT is a sink. The average rate of the internal generation resulting from the temperature advection is 23.2 W m^{-2}, which is larger than the average of GA, 5.5 W m^{-2}. If "advection" is used in a broad sense referring to the advective property of the flow, the divergence of the temperature flux discussed in the last section is, in effect, the temperature advection. The results from both of the APE budgets suggest that the temperature advection within the AMTEX storm system is a more important source of APE than the generation by diabatic processes.

The thermal circulation described by term EAW is a sink of the storm's APE. The average rate of conversion is -20.6 W m^{-2}, which is one order of magnitude smaller than the AW term in APE budget I. Although the physical processes described by EAW and AW are similar, there is not a good temporal correlation between the two. The vertical profiles of the horizontally integrated EAW are shown in Fig. 42. Direct circulations exist in the troposphere and indirect ones exist in the stratosphere. The minima occur in the middle troposphere.

Following Edmon and Vincent (1977), the negative correlation between EVAT and EAW can be explained by comparing the expressions of the two terms:

$$\mathrm{EVAT} = -\frac{c_p}{\sigma g}\int \varepsilon\,\omega\frac{\partial T}{\partial p}\,dV ,$$

and

$$\mathrm{EAW} = \frac{c_p}{\sigma g}\int \varepsilon\,\omega\frac{\alpha}{c_p}\,dV .$$

The function, αc_p^{-1}, represents the dry adiabatic lapse rate in the pressure coordinates. The lapse rate of the real atmosphere, $\frac{\partial T}{\partial p}$, usually has the same sign, but smaller magnitude in comparison with αc_p^{-1}. Hence, the terms EVAT and EAW are similar in magnitude and opposite in sign, with EAW being the larger of the two.

Since the image scale factor of the polar stereographic map projection varies with latitude, the horizontal area of the storm volume at 1200 GMT 15 February is approximately 120% of that of the storm volumes at the first three times. This increase in the horizontal area contribute negatively to the time rate of change in A. The decrease in the surface pressure also contribute negatively to the change in A.

Shown in Fig. 43 is the APE budget of hurricane Carmen (Edmon and Vincent, 1977). The formulation is the same as the APE budget II except that the storm volumes are fixed in space. Edmon and Vincent remarked that the quasi-Lagrangian budget is essentially the same. The most notable differences in the APE budget of Carmen are the quasi-balance between DADT and DEDT, and the relatively small magnitude of the residual. The latter point is especially interesting since the tropical storms generally are more cumulus-oriented than the extratropical storms. No apparent explanation can be offered at this time. The following three aspects are the same as for the AMTEX storm: 1) the temperature advection is an internal source of APE, 2) the generation by diabatic processes is relatively small, and 3) EAW is a sink term.

5. KE Budget

The KE budget of the AMTEX storm will be discussed in this section. The values of all the terms in Eq. (21) are included in Table 18. All, but the vertical flux of K (VFK) and the effect in K due to the surface pressure changes (DPSK), are also plotted as functions of time in Fig. 44. The major sources and sinks are the horizontal flux of K (HFK), the local production of K by cross-contour flow (GK), and the residual (RK).

The horizontal flux of K has values of -100.6 W m^{-2} at 0000 GMT 13 February and 26.0 W m^{-2} at 1200 GMT 15 February, increasing almost linearly with time. Since the upper troposphere has a significant influence on the KE budget due to its higher wind speed, it is helpful to examine the relative positions of the analyzed jet streaks and the storm volumes (Fig. 17). Early in the study period, the storm volume is situated to the southwest of the long wave trough. The jet streak at the base of this trough leads out of the storm volume, resulting in an export of kinetic energy. As the short wave which is associated with the AMTEX storm travels eastward, the corresponding jet streak appears at the inflow side of the storm volume, and the export of kinetic energy starts decreasing. The storm volume moves in the northeast direction after 1200 GMT 14 February. At 1200 GMT 15 February the major jet leads into the storm volume; therefore, HFK assumes a positive value. The export of kinetic energy during the early intensifying stage is also found in other studies of the extratropical cyclones (e.g., Vincent and Chang, 1975).

The ageostrophic component of the wind field generates kinetic energy at an average rate of 23.3 W m^{-2}. Term GK increases from 0000 to 1200 GMT 13 February, reaching a maximum of 33.0 W m^{-2} at 0000 GMT 14 February and gradually decreases afterwards. This temporal variation can be explained by the characteristics in the upper level flow (Soliz, 1977). While the short wave was entering the storm volume at 1200 GMT 13 February and 0000 GMT 14 February, an area of strong confluence developed just ahead of it. A temporary imbalance between the pressure gradient force and the Coriolis force caused the wind to blow across height contours toward the low center. Therefore, there is an increase in GK. Toward the end of the study period, less confluence can be seen in the storm volume and there is a decrease in GK. The maxima in the horizontal distributions of vertically integrated GK (Fig. 45) appear mostly along or to the east of the short wave. Vertically, the maxima occur in the upper troposphere or lower stratosphere (Fig. 46).

Note that term GK is an order of magnitude smaller than the term AW. As discussed in section 3, a large portion of the converted APE is used as boundary work for expansion. GK is of the same order of magnitude as the EAW term in APE budget II. However, no good correlation can be found among GK, AW and EAW.

To aid the discussion of the residual of the KE budget, the frictional dissipation in the planetary boundary layer is estimated using Lettau's (1961) formulation given by

$$D = \rho C_g^2 U_g^3 \cos\beta ,$$

where C_g, the geostrophic drag coefficient, is

$$C_g = k[\ln(U_g z_o^{-1} f^{-1}) - 1.865]^{-1} .$$

U_g, β, k and z_o are the same as those used in section 2 of Chapter IV, and f is the Coriolis parameter. As shown in Table 18, the boundary frictional dissipation of the AMTEX storm is of the order of 1 W m^{-2}. It had a minimum of 0.5 W m^{-2} at 1200 GMT 13 February and gradually increased up to 9.0 W m^{-2} at 1200 GMT 15 February. The average dissipation rate near the tropopause has been shown to be just over 1 W m^{-2} (Kung, 1966; Trout and Panofsky, 1969). Therefore, the total dissipation of KE of the AMTEX storm is probably of the order of 1 W m^{-2} and not much larger than 10 W m^{-2}.

If the residual of the KE budget represented only dissipation, RK would always be negative and the magnitude would be of the order of 1 W m^{-2} and not much larger than 10 W m^{-2}. The residual, RK, of the AMTEX storm is 73.2 W m^{-2} at 0000 GMT 13 February and -57.1 W m^{-2} at 1200 GMT 15 February, decreasing almost linearly with time. On the 13th and 14th, there appears to be a mechanism at work which can not only overcome the frictional dissipation, but also leads to a transfer of KE from the subgrid scale to the grid scale. This would suggest that there is a net generation or positive advection of KE at the subgrid scale. However, on the 15th, there is a net transfer of KE from the grid scale to the subgrid scale.

Soliz (1977) postulated that these subgrid scale processes may be associated with the cumulus activity, and/or may also be related to the turbulent wake which is often observed downstream from an obstructive object when the Reynolds number of the flow is larger than 2.4×10^4 (Landau and Lifshitz, 1959). In this case, the obstructive object is the Tibetan Plateau. The Reynolds number is estimated by Soliz to be around 1.5×10^6, which is larger than the critical Reynolds number.

It is difficult to explicitly identify any active mechanisms at the subgrid scale with the data resolution available. However, the importance of the subgrid scale processes cannot be ignored for either the APE or the KE budget.

CHAPTER VI

SUMMARY AND CONCLUSIONS

This research was directed at examining the energetics and the relationship between the diabatic processes and the immediate development of a cyclone over the East China Sea during the 1975 AMTEX. The available potential energy budgets, one formulated by Vincent and Chang (1973) and the other by Edmon (1978), and the kinetic energy budget are evaluated in a quasi-Lagrangian frame for areas of approximately 6 x 10^6 km^2 at 0000 and 1200 GMT 13-15 February 1975, which covers the incipient and intensifying stages.

Three components of the diabatic processes are considered. Both the stable and convective latent heat release are estimated; the latter is accomplished using Kuo's cumulus parameterization scheme. The sensible heat transferred from the ocean is computed by employing the bulk aerodynamic method. The radiational heating is estimated considering modeled cloud distributions. The net effect of the diabatic processes on the AMTEX storm is to generate the storm's APE. The average of the total generation during the period of study is 5.5 $W m^{-2}$. The contribution from the latent heat release is the largest and that from the radiational cooling is relatively small. The accuracy of the estimated diabatic heating rates may be improved with better parameterization methods. The generation of APE, however, probably will not increase by one or two orders of magnitude.

The APE budget I (Vincent and Chang, 1973) and the KE budget can best be summarized through the use of the energy diagram depicted in Fig. 2. With the exception of the horizontal flux and the residual in the KE budget, most of the larger terms do not change sign during the period of study. Therefore, the budgets are averaged in time and the resulting energy diagram is shown in Fig. 47.

In disagreement with past speculations, the diabatic heating is not an important energy source for the AMTEX storm. The in situ generation of APE by diabatic processes is small compared to the internal sources resulting from the temperature advection. In APE budget I, these internal sources are related to the horizontal divergence of the temperature flux (HFA + HAPR) and the change in the mass-potential temperature distribution due to vertical motion (VAPR). The average values of HFA + HAPR and VAPR are 157.5 and 203.9 $\mathrm{W\,m^{-2}}$, respectively. The major sinks in APE budget I are the conversion of APE (AW) and the residual (RA_I). The AMTEX storm's APE is converted to kinetic energy and boundary work through large scale vertical motion at an average rate of $-289.2\,\mathrm{W\,m^{-2}}$. If the observational errors and the errors accumulated through data manipulation are not significant, the grid scale APE is transferred to the subgrid scale at an average rate of -143.7 W m^{-2}.

One important factor in the KE budget is the relative position of the analyzed jet stream and the storm volume. Kinetic energy is advected out of the storm volumes from 0000 GMT 13 February to 0000 GMT 15 February and into the storm volume at 1200 GMT 15 February, with the mean flux being -37.7 W m^{-2}. The ageostrophic component of the wind serves to constantly produce kinetic energy at an average rate of 23.3 W m^{-2}. The residual has an average value of 11.5 W m^{-2}. Kinetic energy is transferred from the subgrid scale to the grid scale on the 13th and 14th, and the direction is reversed on the 15th.

In the mean for the AMTEX storm, available potential energy is converted to kinetic energy. This conversion process is accomplished through both grid and subgrid scale motions. The mean transfer of APE from the grid to the subgrid scale and the mean transfer of KE from the subgrid to the grid scale suggest that there is a net conversion of APE to KE at the subgrid scale. Although it is difficult to identify any active mechanisms at the subgrid scale, it is shown in this study that they are extremely important in describing the energetics of the extratropical cyclones. A significant portion of the converted APE through large-scale vertical motion is used as boundary work for expansion. This and the export of KE demonstrate that the interaction between the storm system and its environment is also very important.

The APE budget II (Edmon, 1978) is essentially the same as APE budget I. Two weak points of APE budget II are the lack of an explicit relationship between the conversion of APE (EAW) and the generation of KE (GK), as well as the difficulty in the physical interpretation of term DEDT which is one of the larger terms. However, the important findings from APE budget I are also supported by the budget II.

Shown in Fig. 48 is the energy cycle of the general circulation as estimated by Oort (1964) and Dutton and Johnson (1967). The present study is comparable with the lower half of the diagram, indicated by the subscript "E" meaning eddies. Since the reference state of a limited region is most likely different from the global one, it is difficult to compare the magnitude and the generation of APE. However, the amount and the local generation of KE of the AMTEX storm are several times larger than the global values. This illustrates the important role played by the atmospheric disturbances in the global energy balance.

This case study has demonstrated that the AMTEX storm derives a significant portion of its available potential energy from the baroclinicity in the atmosphere within the storm system. Comparatively speaking, the energy supplied from the ocean during air mass modification is not important in the immediate cyclone development. However, at a time scale longer than that of cyclone development, the continuous heating of the atmosphere by the ocean creates a situation where an invasion of cold, continental air gives rise to strong baroclinicity, which in turn is favorable for the development of extratropical cyclones. The results of this study suggest that numerical simulations of east-coast cyclogenesis may benefit more from improvement in the observational network and the representation of subgrid scale processes than from better modeling of the air-sea interaction.

BIBLIOGRAPHY

Agee, E. M. and R. P. Howley, 1977: Latent and sensible heat flux calculations at the air-sea interface during AMTEX '74. J. Appl. Meteor., 16, 443-447.

Amburn, S. A., 1975: Estimates of sensible and latent heat transfer at the air-sea interface during AMTEX '74. M.S. Thesis, University of Oklahoma, Norman, 126 pp.

Baxter, T. L., 1975: Meteorological analysis models. Final Report, Ocean Data Systems, Inc.

Chaplin, W. H., 1976: Radiation budgets of the troposphere over the east China Sea during the Air-Mass Transformation Experiment (AMTEX) 1974. Ph.D. Thesis, University of Oklahoma, Norman, 114 pp.

______ and J. F. Kimpel, 1978: Effects of clouds on the radiation budget of the troposphere during the Air-Mass Transformation Experiment (AMTEX). J. Meteor. Soc. Japan, 56, 121-129.

Deacon, E. L. and E. K. Webb, 1962: Interchange of properties between the sea and air. The Sea, 1, M. N. Hill, Ed., John Wiley and Sons, 43-87.

Deardorff, J. W., 1968: Dependence of air-sea transfer coefficients on bulk stability. J. Geophys. Res., 73, 2549-2557.

Dopplick, T. G., 1972: Radiative heating of the global atmosphere. J. Atmos. Sci., 29, 1278-1294.

Dutton, J. A. and D. R. Johnson, 1967: The theory of available potential energy and a variational approach to atmospheric energetics. Advances in Geophysics, 12, 333-436.

Edmon, H. J. and D. G. Vincent, 1976: An application of two tropical parameterization schemes of convective latent heat release in middle latitudes. Mon. Wea. Rev., 104, 1141-1153.

______ and ______, 1977: Energy budget analysis during the intensification of hurricane Carmen (1974). 11th Technical Conference on Hurricanes and Tropical Meteorology, Dec. 13-16, 1977, Miami Beach, Florida.

______, 1978: A reexamination of limited-area available potential energy budget equations. *J. Atmos. Sci.*, *35*, 1655-1659.

Gall, R. L. and D. R. Johnson, 1971: The generation of available potential energy by sensible heating: a case study. *Tellus*, *23*, 465-482.

GARP Report, 1973: *The Air-Mass Transformation Experiment*. Global Atmospheric Research Programme (GARP), Publ. Ser. No. 13, WMO, Geneva, 54 pp.

Haltiner, G. J., 1971: *Numerical Weather Prediction*. John Wiley & Sons, New York, 317 pp.

Holton, J. R., 1972: *An Introduction to Dynamic Meteorology*. Academic Press, 319 pp.

Johnson, D. R., 1970: The available potential energy of storms. *J. Atmos. Sci.*, *27*, 727-741.

Krishnamurti, T. N., M. Kanamitsu, B. F. Ceselski and M. B. Mathur, 1973: Florida State University's tropical prediction model. *Tellus*, *25*, 523-535.

Kung, E. C., 1966: Large-scale balance of kinetic energy in the atmosphere. *Mon. Wea. Rev.*, *94*, 627-640.

Kuo, H. L., 1974: Further studies of the parameterization of the influence of cumulus convection on large scale flow. *J. Atmos. Sci.*, *31*, 1232-1240.

Landau, L. D. and E. M. Lifshitz, 1959: *Fluid Dynamics*. Translation by J . B. Sykes and W. H. Reid, Pergamon Press, Addison-Wesley Publishing Co., Inc., 431 pp.

Lettau, H. H., 1961: Theoretical wind spirals in the boundary layer of a barotropic atmosphere. Annual Report, Contract DA-36-039-80282, Department of Meteorology, University of Wisconsin, Madison.

Lorenz, E. N., 1967: *The Nature and Theory of the General Circulation of the Atmosphere*. WMO, Geneva, 161 pp.

Mitsuta, Y. and T. Fujita, 1975: Boundary layer and radiation observations. *AMTEX '75 Data Report*, *4*.

______, N. Mongi and O. Tsukomoto, 1977: Bulk transfer coefficients as observed in AMTEX. Proceedings of the IAGA/IAMAP Joint Assembly, 22 Aug. - 3 Sept. 1977, Seattle, Washington.

Ninomiya, K., 1972: Heat and water vapor budget over the East China Sea in the winter season. J. Meteor. Soc. Japan, 50, 1-17.

Oort, A. H., 1964: On estimates of the atmospheric energy cycle. Mon. Wea. Rev., 92, 483-493.

Palmen, E., and C. W. Newton, 1969: Atmospheric Circulation Systems: Their Structure and Physical Interpretation. Academic Press, 603 pp.

Pant, G. B., 1976: Available potential energy and kinetic energy processes during the life cycle of an extratropical cyclone. Ph.D. Thesis, Purdue University, 99 pp.

Petterssen, S., 1950: Some aspects of the general circulation of the atmosphere. Cent. Proc. Roy. Meteor. Soc., 120-155.

Roll, H. U., 1965: Physics of the Marine Atmosphere. Academic Press, New York.

Rossby, C. G. and R. B. Montgomery, 1935: The layer of frictional influence in wind and ocean currents. Papers in Physical Oceanography and Meteorology, 3 (3). Massachusetts Institute of Technology and Woods Hole Oceanographic Institute.

Sasaki, Y. K., 1970: Some basic formalisms in numerical variational analysis. Mon. Wea. Rev., 98, 875-883.

Sheppard, P. A., 1958: Transfer across the earth's surface through the air above. Quart. J. Roy. Meteor. Soc., 78, 583-539.

Soliz, P., 1977: A diagnostic analysis of kinetic energy balances of a developing cyclone over the East China Sea during AMTEX 1975. Ph.D. Thesis, University of Oklahoma, Norman.

Stephens, P. L., 1978: The role of thermals in the turbulent processes of the convective boundary layer. M.S. Thesis, University of Oklahoma, Norman, 79 pp.

Trout, D. and H. A. Panofsky, 1969: Energy dissipation near the tropopause. Tellus, 21, 355-358.

Van Mieghem, J., 1956: The energy available in the atmosphere for conversion into kinetic energy. Beitr. Phys. Atmosphäre, 29, 129-142.

Vincent, D. G. and L. N. Chang, 1973: Some further considerations concerning energy budgets of moving systems. Tellus, 25, 224-232.

______ and ______, 1975: Kinetic energy budgets of moving systems: case studies for an extratropical cyclone and hurricane Celia, 1970. Tellus, 27, 215-233.

______, G. B. Pant and H. J. Edmon, 1977: Generation of available potential energy of an extratropical cyclone system. Mon. Wea. Rev., 105, 1252-1265.

Wildman, T. J., 1977: Comparison of several methods of determining turbulent transfer in the surface layer using the AMTEX data. M.S. Thesis, University of Oklahoma, Norman, 84 pp.

APPENDIX A

THE TOTAL POTENTIAL ENERGY OF THE REFERENCE STATE

In Chapter II, the reference state has been defined as a horizontally invariant and hydrostatically stable density distribution achieved by isentropically redistributing the mass in the natural state without any boundary work done to or advection into the system. The purpose of this appendix is to show that the total potential energy of this reference state is a minimum and its kinetic energy is a maximum. Following Van Mieghem (1956), the first and second derivatives of the total potential energy with respect to time will be shown to be zero and negative, respectively. The height coordinates will be used in this appendix instead of the pressure coordinates. Therefore,

$$\vec{V} = \frac{dx}{dt}\vec{i} + \frac{dy}{dt}\vec{j} + \frac{dz}{dt}\vec{k},$$

and

$$\nabla = \frac{\partial}{\partial x}\vec{i} + \frac{\partial}{\partial y}\vec{j} + \frac{\partial}{\partial z}\vec{k}.$$

Let ϕ and e represent the potential and internal energy per unit mass, respectively. The total potential energy of a fluid system is

$$\Phi + E = \int_{\tau} \rho(\phi + e)\, d\tau, \tag{A.1}$$

where $d\tau$ is a differential volume. The individual time rate of change of the total potential energy is given by

$$\frac{d}{dt}(\Phi + E) = \int_{\tau} \rho\left(\vec{V}\cdot\nabla\phi + \frac{de}{dt}\right) d\tau, \tag{A.2}$$

where

$$\rho\frac{d\phi}{dt} = \rho\vec{V}\cdot\nabla\phi = \rho g w, \tag{A.3}$$

and $w(= \frac{dz}{dt})$ is the vertical component of $\vec{V}$. Substitution of the first law of thermodynamics

$$\rho\frac{de}{dt} = -p\,\nabla\cdot\vec{V} - \nabla\cdot\vec{W} \tag{A.4}$$

and the identity

$$p\,\nabla\cdot\vec{V} = \nabla\cdot(p\vec{V}) - \vec{V}\cdot\nabla p \tag{A.5}$$

into (A.2) yields,

$$\frac{d}{dt}(\Phi + E) = \int_{\tau}(\rho\nabla\phi + \nabla p)\cdot\vec{V}\,d\tau - \oint_{\sigma}(W_N + pV_N)\,d\sigma, \tag{A.6}$$

where the subscript N represents the outward normal to the complete boundary of the fluid system, and W_N and V_N are the corresponding normal components of the heat flux $\vec{W}$ and the velocity $\vec{V}$.

The volume and surface integrals on the right hand side of (A.6) are both functions of time t only. Taking into account the well known relation

$$\frac{d}{dt}d\tau = d\tau\,\nabla\cdot\vec{V} \tag{A.7}$$

and the equation of continuity

$$\frac{d}{dt}(\rho\,d\tau) = \rho\,d\tau\left[\frac{1}{\rho}\frac{d\rho}{dt} + \nabla\cdot\vec{V}\right] = 0, \tag{A.8}$$

the second derivative of the total potential energy with respect to time is

$$\frac{d^2}{dt^2}(\Phi + E) = \int_\tau \left\{ \vec{V} \cdot (\rho \nabla\nabla\phi + \nabla\nabla p) \cdot \vec{V} + \left[\nabla \frac{\partial p}{\partial t} + (\nabla \cdot \vec{V}) \nabla p \right] \cdot \vec{V} \right.$$

$$\left. + (\rho \nabla\phi + \nabla p) \cdot \frac{d\vec{V}}{dt} \right\} d\tau - \frac{d}{dt} \oint_\sigma (W_N + pV_N)\, d\sigma. \qquad \text{(A.9)}$$

For a thermally and mechanically insulated system, the net flux of heat and mechanical energy is zero. Thus,

$$\oint_\sigma (W_N + pV_N)\, d\sigma = 0 \qquad \text{(A.10)}$$

and

$$\frac{d}{dt} \oint_\sigma (W_N + pV_N)\, d\sigma = 0. \qquad \text{(A.11)}$$

If the hydrostatic equilibrium is realized at time $t = t_e$, then

$$\rho_e \nabla\phi + \nabla p_e = 0. \qquad \text{(A.11)}$$

By virtue of (A.10) and (A.12), the first derivative of $\Phi + E$ with respect to time satisfies the extremum condition, i.e.,

$$\left\{ \frac{d}{dt}(\Phi + E) \right\}_e = 0. \qquad \text{(A.13)}$$

Consequently, when a thermally and mechanically insulated and frictionless fluid reaches a state of hydrostatic equilbrium, the total potential energy assumes an extremum value.

Applying the del operator ∇ to (A.12) produces

$$\nabla\rho_e \nabla\phi + \rho_e \nabla\nabla\phi + \nabla\nabla p_e = 0. \qquad \text{(A.14)}$$

Substitution of (A.11), (A.12), (A.14) and the identity

$$\vec{V} \cdot \nabla\left(\frac{\partial p}{\partial t}\right) = \nabla \cdot \left(\vec{V} \frac{\partial p}{\partial t}\right) - \frac{\partial p}{\partial t} \nabla \cdot \vec{V} \qquad \text{(A.15)}$$

into (A.9) yields

$$\left\{ \frac{d^2}{dt^2}(\Phi - E) \right\}_e = \int_{\tau_e} \left\{ -(\vec{V}_e \cdot \nabla\rho_e)(\vec{V}_e \cdot \nabla\phi) + \nabla \cdot \vec{V}_e \left[\vec{V}_e \cdot \nabla p_e - \left(\frac{\partial p}{\partial t}\right)_e \right] \right\} d\tau_e$$

$$+ \oint_{\sigma_e} \left(V_N \frac{\partial p}{\partial t} \right)_e d\sigma_e. \qquad \text{(A.16)}$$

In order to prove that the total potential energy of the reference state is a minimum, it is necessary to impose a constraint which is more strict than (A.10). The redistribution of mass leading toward a horizontal stratification of the fluid will be assumed to occur under adiabatic flow, i.e.,

$$\nabla \cdot \overrightarrow{W} = 0. \qquad \text{(A.17)}$$

If the fluid is dry air only, for any dry adiabatic processes, the following holds true:

$$-\frac{\rho}{\theta}\frac{d\theta}{dt} = \frac{d\rho}{dt} - \frac{1}{c^2}\frac{dp}{dt} = 0, \qquad \text{(A.18)}$$

where θ is the potential temperature and c is the speed of sound. Substitution of the equation of continuity into (A.18) renders

$$\frac{\partial p}{\partial t} + \vec{V} \cdot \nabla p + c^2 \rho \nabla \cdot \vec{V} = 0. \qquad \text{(A.19)}$$

From Poisson's equation, it is easy to obtain

$$\frac{\rho}{\theta}\nabla\theta = -\nabla\rho + \frac{1}{c^2}\nabla p. \qquad \text{(A.20)}$$

Elimination of $\frac{\partial p}{\partial t}$ between (A.19) and (A.16) and substitution of (A.20) leads to

$$\left\{\frac{d^2}{dt^2}(\Xi + \Xi)\right\}_e = \int_{\tau_e}\left\{(\vec{V}_e \cdot \frac{\nabla\theta_e}{\theta_e})(\vec{V}_e \cdot \nabla\dot{\varphi}) + \frac{1}{c_e^2}(c_e^2 \nabla \cdot \vec{V}_e - \vec{V}_e \cdot \nabla\dot{\varphi})^2\right\}\rho_e \, d\tau_e$$

$$+ \oint_{\sigma_e} (V_N \frac{\partial p}{\partial t})_e \, d\sigma_e. \qquad \text{(A.21)}$$

The volume and surface integrals in (A.21) can be simplified. From (A.12) it is clear that the pressure p_e, density ρ_e and potential temperature θ_e are functions of height only when the hydrostatic equilibrium is realized. Therefore,

$$\left\{\begin{aligned} \vec{V}_e\cdot\nabla\phi &= \frac{d\phi}{dz}w_e = g\,w_e\,, \\ \vec{V}_e\cdot\nabla p_e &= \frac{dp_e}{dz}w_e = -g\,\rho_e\,w_e\,, \\ \vec{V}_e\cdot\nabla\theta_e &= \frac{d\theta_e}{dz}w_e\,. \end{aligned}\right. \tag{A.22}$$

Substituting (A.22) in the first half of the volume integral of (A.21) yields,

$$\int_{\tau_e}\frac{\rho_e}{\theta_e}(\vec{V}_e\cdot\nabla\theta_e)(\vec{V}_e\cdot\nabla\phi)\,d\tau_e = \int_{\tau_e}\frac{g}{\theta_e}\frac{d\theta_e}{dz}w_e^2\,\rho_e\,d\tau_e\,. \tag{A.23}$$

Utilizing (A.12) and (A.19), the second half of the volume integral becomes,

$$\begin{aligned}\int_{\tau_e}\frac{\rho_e}{c_e^2}(c_e^2\,\nabla\cdot\vec{V}_e-\vec{V}_e\cdot\nabla\phi)^2\,d\tau_e &= \int_{\tau_e}\frac{\rho_e}{c_e^2}(c_e^2\,\nabla\cdot\vec{V}_e+\frac{1}{\rho_e}\vec{V}_e\cdot\nabla p_e)^2\,d\tau_e \\ &= \int_{\tau_e}\left(\frac{1}{\rho c}\frac{\partial p}{\partial t}\right)_e^2\rho_e\,d\tau_e\,. \end{aligned} \tag{A.24}$$

The surface integral in (A.21) remains to be simplified. It is reasonable to assume that the fluid system is bounded by solid walls σ_s where $V_N = 0$ and by free surfaces σ_f where $\frac{dp}{dt} = 0$. When the hydrostatic equilibrium is attained at time t_e, the following two relations exist along the free surface of the fluid:

$$\begin{aligned}\left(\frac{dp}{dt}\right)_e &= \left(\frac{\partial p}{\partial t}\right)_e + \vec{V}_e\cdot(\nabla p)_e = \left(\frac{\partial p}{\partial t}\right)_e + w_e\frac{dp_e}{dz} \\ &= \left(\frac{\partial p}{\partial t}\right)_e - g\,\rho_e\,w_e = 0 \end{aligned} \tag{A.25}$$

and $$(V_N)_e = \overline{w}_e .$$

The reason for (A.26) is that the free surface, being necessarily an isobaric surface, coincides with a geopotential surface. Utilizing (A.25) and (A.26), the surface integral in (A.21) is,

$$\oint_{\sigma_e} (V_N \frac{\partial p}{\partial t})_e \, d\sigma_e = \int_{\sigma_e, free} (V_N \frac{\partial p}{\partial t})_e \, d\sigma_e = \int_{\sigma_e, free} g \rho_e \overline{w}_e^2 \, d\sigma_e . \quad \text{(A.26)}$$

Combining (A.23), (A.24) and (A.27), $\{\frac{d^2}{dt^2}(\bar{\Phi} + E)\}_e$ reduces to

$$\{\frac{d^2}{dt^2}(\bar{\Phi} + E)\}_e = \int_{\tau_e} \{\frac{g}{\theta} \frac{d\theta_e}{dz} \overline{w}_e^2 + (\frac{1}{\rho c} \frac{\partial p}{\partial t})_e^2 \} \rho_e \, d\tau_e$$

$$+ \int_{\sigma_e, free} g \rho_e \overline{w}_e^2 \, d\sigma_e . \quad \text{(A.27)}$$

Now, consider the lower limit of the atmosphere as a solid boundary and the upper limit as a free surface where ρ_e vanishes. Applying (A.28) to the earth's atmosphere gives

$$\{\frac{d^2}{dt^2}(\bar{\Phi} + E)\}_e = \int_{atm} [\frac{g}{\theta_e} \frac{d\theta_e}{dz} \overline{w}_e^2 + (\frac{1}{\rho c} \frac{\partial p}{\partial t})_e^2] \rho_e \, d\tau_e , \quad \text{(A.28)}$$

Hence, when

$$\frac{d\theta_e}{dz} > 0 , \quad \text{(A.30)}$$

then

$$\{\frac{d^2}{dt^2}(\bar{\Phi} + E)\}_e > 0 , \quad \text{(A.31)}$$

the extremum value $(\bar{\Phi} + E)_e$ is a minimum of $\bar{\Phi} + E$ and thus the reference state is in a stable condition. The inequality $\frac{d\theta_e}{dz} > 0$ is a sufficient condition for $(\bar{\Phi} + E)_e$ to be a minimum of $\bar{\Phi} + E$.

Since the sum of the potential, internal and kinetic energy is conservative, a state of the atmosphere which possesses a minimum of total potential energy will likewise have a maximum of kinetic energy.

APPENDIX B

THE ENERGY BUDGET EQUATIONS

The equations for the quasi-Lagrangian time rate of change of APE and KE of a limited region will be derived. Let ψ represent any meteorological variable. The relationships between the quasi-Lagrangian time rate of change $\frac{\delta\psi}{\delta t}$ and the Eulerian time rate of change $\frac{\partial\psi}{\partial t}$, as well as the Lagrangian time rate of change $\frac{d\psi}{dt}$ are,

$$\frac{\delta\Psi}{\delta t} = \frac{\partial\Psi}{\partial t} + \nabla\cdot\Psi\mathbb{W} + \frac{\partial}{\partial p}\Psi\tilde{\omega} = \frac{d\Psi}{dt} - \nabla\cdot\Psi(\mathbb{V}-\mathbb{W}) - \frac{\partial}{\partial p}\Psi(\omega-\tilde{\omega}), \tag{B.1}$$

where $\mathbb{W} = \frac{\delta x}{\delta t}\vec{i} + \frac{\delta y}{\delta t}\vec{j}$ and $\tilde{\omega} = \frac{\delta p}{\delta t}$, which represent the horizontal and vertical velocities at which the storm volume moves.

The amount of APE for a limited region, as expressed in (14), is

$$A = \frac{c_p}{\sigma g}\iint_0^{p_s} \epsilon T \, dp \, d\sigma, \tag{B.2}$$

where

$$\epsilon = 1 - \left(\frac{p_r}{p}\right)^{\kappa}, \tag{B.3}$$

and

$$p_r = \frac{1}{\sigma}\iint_{\theta_T}^{\theta} \frac{\partial p}{\partial \phi} \, d\phi \, d\sigma. \tag{B.4}$$

The quasi-Lagrangian time rate of change of A is,

$$\frac{\delta A}{\delta t} = \frac{\delta}{\delta t}\left[\frac{c_p}{\sigma g}\iint_0^{p_s} \epsilon T \, dp \, d\sigma\right] = -\frac{A}{\sigma}\frac{\delta\sigma}{\delta t} + \frac{c_p}{\sigma g}\frac{\delta}{\delta t}\iint_0^{p_s} \epsilon T \, dp \, d\sigma. \tag{B.5}$$

Using Leibnitz's rule and the divergence theorem, (B.5) becomes,

$$\frac{\delta A}{\delta t} = -\frac{A}{\sigma}\frac{\delta \sigma}{\delta t} + \frac{c_p}{\sigma g}\iint_0^{P_s} \frac{\partial}{\partial t}(\epsilon T) + \nabla \cdot (\epsilon T \mathbb{W}) + \frac{\partial}{\partial p}(\epsilon T \tilde{\omega})\, dp\, d\sigma. \tag{B.6}$$

Since $\frac{\partial \Psi}{\partial t} = \frac{d\Psi}{dt} - \nabla \cdot \psi \mathbb{V} - \frac{\partial}{\partial p}\psi\omega,$

(B.6) can be written as

$$\frac{\delta A}{\delta t} = -\frac{A}{\sigma}\frac{\delta \sigma}{\delta t} + \frac{c_p}{\sigma g}\iint_0^{P_s} \frac{d}{dt}(\epsilon T) - \nabla \cdot [\epsilon T(\mathbb{V} - \mathbb{W})] - \frac{\partial}{\partial p}[\epsilon T(\omega - \tilde{\omega})]\, dp\, d\sigma. \tag{B.7}$$

Expanding the derivative of the first integrand and utilizing the first law of thermodynamics ($Q = c_p \frac{dT}{dt} - \alpha\,\omega$) give,

$$\frac{d}{dt}(\epsilon T) = \frac{\epsilon Q}{c_p} + \frac{\alpha \omega}{c_p} - \frac{T}{p^{\kappa}}\frac{d P_r^{\kappa}}{dt}. \tag{B.8}$$

Substitution of (B.8) into (B.7) yields,

$$\frac{\delta A}{\delta t} = -\frac{A}{\sigma}\frac{\delta \sigma}{\delta t} + \frac{c_p}{\sigma g}\iint_0^{P_s} \frac{\epsilon Q}{c_p} + \frac{\alpha \omega}{c_p} - \frac{T}{p^{\kappa}}\frac{d P_r^{\kappa}}{dt}$$

$$- \nabla \cdot [\epsilon T(\mathbb{V} - \mathbb{W})] - \frac{\partial}{\partial p}[\epsilon T(\omega - \tilde{\omega})]\, dp\, d\sigma. \tag{B.9}$$

This formulation was derived by Vincent and Chang (1973). Since the pressure coordinate is used in this study, $\tilde{\omega}$ is zero everywhere except at the surface due to changes in the surface pressure. The following two expressions will be used interchangeably;

$$\frac{c_p}{\sigma g}\iint_0^{P_s} \frac{\partial}{\partial p}(\epsilon T \tilde{\omega})\, dp\, d\sigma = \frac{c_p}{\sigma g}\int \epsilon_s T_s \frac{\delta P_s}{\delta t}\, d\sigma. \tag{B.10}$$

Following Edmon (1978), (B.5) may be written as

$$\frac{\delta A}{\delta t} = -\frac{A}{\sigma}\frac{\delta \sigma}{\delta t} + \frac{c_p}{\sigma g}\iint_0^{P_s} \epsilon \frac{\delta' T}{\delta t} + T\frac{\delta' \epsilon}{\delta t} + \frac{\partial}{\partial p}(\epsilon T \tilde{\omega})\, dp\, d\sigma, \tag{B.11}$$

where

$$\frac{\delta' \Psi}{\delta t} = \frac{\partial \Psi}{\partial t} + \nabla \cdot \psi \mathbb{W}. \tag{B.12}$$

Since

$$\frac{\delta' T}{\delta t} = \frac{dT}{dt} - (\mathbb{V}-\mathbb{W})\cdot\nabla T - \omega\frac{\partial T}{\partial p} = \frac{Q}{c_p} + \frac{\alpha\omega}{c_p} - (\mathbb{V}-\mathbb{W})\cdot\nabla T - \omega\frac{\partial T}{\partial p}\,, \qquad \text{(B.13)}$$

(B.11) becomes,

$$\frac{\delta A}{\delta t} = -\frac{A}{\sigma}\frac{\delta\sigma}{\delta t} + \frac{c_p}{\sigma g}\iint_0^{p_s} \frac{\epsilon Q}{c_p} + \frac{\epsilon\alpha\omega}{c_p} - \epsilon(\mathbb{V}-\mathbb{W})\cdot\nabla T - \epsilon\omega\frac{\partial T}{\partial p}$$

$$+ T\frac{\delta'\epsilon}{\delta t}\,dp\,d\sigma + \frac{c_p}{\sigma g}\int \epsilon_s T_s \frac{\delta p_s}{\delta t}\,d\sigma. \qquad \text{(B.14)}$$

To show that (B.9) and (B.14) are equivalent, first expand $\frac{dp_r^{\kappa}}{dt}$ and rewrite (B.9);

$$\underset{(1)}{\frac{\delta A}{\delta t}} = \underset{(2)}{-\frac{A}{\sigma}\frac{\delta\sigma}{\delta t}} + \frac{c_p}{\sigma g}\iint_0^{p_s} \underset{(3)}{\frac{\epsilon Q}{c_p}} + \underset{(4)}{\frac{\alpha\omega}{c_p}} - \underset{(5)}{\frac{T}{p^{\kappa}}\frac{\delta' p_r^{\kappa}}{\delta t}} - \underset{(6)}{\frac{T}{p^{\kappa}}(\mathbb{V}-\mathbb{W})\cdot\nabla p_r^{\kappa}}$$

$$\underset{(7)}{-\frac{T}{p^{\kappa}}\omega\frac{\partial p_r^{\kappa}}{\partial p}} - \underset{(8)}{\nabla\cdot[\epsilon T(\mathbb{V}-\mathbb{W})]} - \underset{(9)}{\frac{\partial}{\partial p}(\epsilon T\omega)}\,dp\,d\sigma + \underset{(10)}{\frac{c_p}{\sigma g}\int \epsilon_s T_s \frac{\delta p_s}{\delta t}\,d\sigma}. \qquad \text{(B.15)}$$

By the properties of derivatives,

$$\frac{\partial p^{\kappa}}{\partial p} = \kappa p^{\kappa-1}\,, \qquad \text{(B.16)}$$

therefore,

$$\frac{1}{p} = \frac{1}{\kappa p^{\kappa}}\frac{\partial p^{\kappa}}{\partial p}\,. \qquad \text{(B.17)}$$

Applying the equation of state and (B.17), term (4) in (B.15) may be written as

$$\text{term (4)} = \frac{c_p}{\sigma g}\iint \frac{RT}{c_p p}\omega\,dp\,d\sigma = \frac{c_p}{\sigma g}\iint \frac{T\omega}{p^{\kappa}}\frac{\partial p^{\kappa}}{\partial p}\,dp\,d\sigma. \qquad \text{(B.18)}$$

The sum of terms (4) and (7), therefore, is,

$$\text{term (4)} + \text{term (7)} = \frac{c_p}{\sigma g}\iint \frac{T\omega}{p^{\kappa}}\frac{\partial}{\partial p}(p^{\kappa} - p_r^{\kappa})\,dp\,d\sigma$$

$$= \frac{c_p}{\sigma g}\iint \frac{T\omega}{p^{\kappa}}\frac{\partial}{\partial p}(\epsilon p^{\kappa})\,dp\,d\sigma = \frac{c_p}{\sigma g}\iint \frac{T\omega}{p^{\kappa}}\left(\epsilon\frac{\partial p^{\kappa}}{\partial p} + p^{\kappa}\frac{\partial\epsilon}{\partial p}\right)dp\,d\sigma$$

$$= \frac{c_p}{\sigma g}\iint \frac{T\omega}{p^{\kappa}}\left(\epsilon\kappa p^{\kappa-1} + p^{\kappa}\frac{\partial\epsilon}{\partial p}\right)dp\,d\sigma = \frac{c_p}{\sigma g}\iint \frac{\epsilon\alpha\omega}{c_p} + T\omega\frac{\partial\epsilon}{\partial p}\,dp\,d\sigma. \qquad \text{(B.19)}$$

Since

$$\nabla\epsilon = \nabla\left(1-\frac{p_r^{\kappa}}{p^{\kappa}}\right) = -\nabla\left(\frac{p_r^{\kappa}}{p^{\kappa}}\right) \qquad \text{(B.20)}$$

and

$$\frac{\delta'\epsilon}{\delta t} = -\frac{\delta'}{\delta t}\left(\frac{p_r^{\kappa}}{p^{\kappa}}\right), \qquad \text{(B.21)}$$

terms (5) and (6) are respectively,

$$\text{term (5)} = T\frac{\delta'\epsilon}{\delta t} \qquad \text{(B.22)}$$

and

$$\text{term (6)} = T(\mathbb{V}-\mathbb{W})\cdot\nabla\epsilon\,. \qquad \text{(B.23)}$$

Substituting (B.19), (B.22) and (B.23) into (B.15) and expanding the derivatives in terms (8) and (9) lead to,

$$\frac{\delta A}{\delta t} = -\frac{A}{\sigma}\frac{\delta\sigma}{\delta t} + \frac{c_p}{\sigma g}\iint_0^{p_s}\frac{\epsilon Q}{c_p} + \frac{\epsilon\alpha\omega}{c_p} + T\omega\frac{\partial\epsilon}{\partial p} + T\frac{\delta'\epsilon}{\delta t} + T(\mathbb{V}-\mathbb{W})\cdot\nabla\epsilon$$

$$-\epsilon(\mathbb{V}-\mathbb{W})\cdot\nabla T - \epsilon T\nabla\cdot(\mathbb{V}-\mathbb{W}) - T(\mathbb{V}-\mathbb{W})\cdot\nabla\epsilon - \epsilon\omega\frac{\partial T}{\partial p}$$

$$-\epsilon T\frac{\partial\omega}{\partial p} - T\omega\frac{\partial\epsilon}{\partial p}\,dp\,d\sigma + \frac{c_p}{\sigma g}\int\epsilon_s T_s\frac{\delta p_s}{\delta t}\,d\sigma. \qquad \text{(B.24)}$$

Use of the continuity equation and the cancellation of similar terms with opposite signs give,

$$\frac{\delta A}{\delta t} = -\frac{A}{\sigma}\frac{\delta\sigma}{\delta t} + \frac{c_p}{\sigma g}\iint_0^{p_s}\frac{\epsilon Q}{c_p} + \frac{\epsilon\alpha\omega}{c_p} - \epsilon(\mathbb{V}-\mathbb{W})\cdot\nabla T - \epsilon\omega\frac{\partial T}{\partial p}$$

$$+T\frac{\delta'\epsilon}{\delta t}\,dp\,d\sigma + \frac{c_p}{\sigma g}\int\epsilon_s T_s\frac{\delta p_s}{\delta t}\,d\sigma,$$

which is the same as (B.14).

Since $\tilde{\omega}$ is zero everywhere except at the surface, $\frac{\delta\psi}{\delta t}$ will be assumed to be equal to $\frac{\delta\psi}{\delta t}$. (B.14) becomes,

$$\frac{\delta A}{\delta t} = -\frac{A}{\sigma}\frac{\delta\sigma}{\delta t} + \frac{c_p}{\sigma g}\iint_0^{p_s}\frac{\epsilon Q}{c_p} + \frac{\epsilon\alpha\omega}{c_p} - \epsilon(\mathbb{V}-\mathbb{W})\cdot\nabla T - \epsilon\omega\frac{\partial T}{\partial p}$$

$$+T\frac{\delta\epsilon}{\delta t}\,dp\,d\sigma + \frac{c_p}{\sigma g}\int\epsilon_s T_s\frac{\delta p_s}{\delta t}\,d\sigma, \qquad \text{(B.25)}$$

and this is the original formulation derived by Edmon.

The amount of KE per unit area for a limited region is,

$$K = \frac{1}{\sigma g}\iint_0^{P_s} k \; dp \, d\sigma. \tag{B.26}$$

where $k = \frac{1}{2}\mathbb{V}\cdot\mathbb{V}$, which is the horizontal KE per unit mass relative to the earth. The quasi-Lagrangian time rate of change of K is,

$$\frac{\delta K}{\delta t} = -\frac{K}{\sigma}\frac{\delta \sigma}{\delta t} + \frac{1}{\sigma g}\frac{\delta}{\delta t}\iint_0^{P_s} k \; dp \, d\sigma$$

$$= -\frac{K}{\sigma}\frac{\delta \sigma}{\delta t} + \frac{1}{\sigma g}\iint_0^{P_s}\frac{dk}{dt} - \nabla\cdot[k(\mathbb{V}-\mathbb{W})] - \frac{\partial}{\partial p}[k(\omega-\tilde{\omega})]\, dp \, d\sigma. \tag{B.27}$$

If ϕ denotes the geopotential and $\mathbb{F}$ is the horizontal frictional force, the following may be obtained from the horizontal equations of motion;

$$\frac{dk}{dt} = -\mathbb{V}\cdot\nabla\phi + \mathbb{V}\cdot\mathbb{F}. \tag{B.28}$$

Substitution of (B.28) into (B.27) yields,

$$\frac{\delta K}{\delta t} = -\frac{K}{\sigma}\frac{\delta \sigma}{\delta t} + \frac{1}{\sigma g}\iint_0^{P_s} -\mathbb{V}\cdot\nabla\phi - \nabla\cdot[k(\mathbb{V}-\mathbb{W})] - \frac{\partial}{\partial p}(k\omega)$$

$$+ \mathbb{V}\cdot\mathbb{F}\; dp\, d\sigma + \frac{1}{\sigma g}\int k_s \frac{\delta P_s}{\delta t}\, d\sigma. \tag{B.29}$$

Note that $\frac{1}{\sigma g}\iint_0^{P_s}\frac{\partial}{\partial p}(k\tilde{\omega})\, dp\, d\sigma$ and $\frac{1}{\sigma g}\int k_s \frac{\delta P_s}{\delta t}\, d\sigma$ are equivalent.

Any meteorological variable ψ can be decomposed into two parts, $\bar{\psi}$ and ψ'. The overbared quantity is a spatial average defined by

$$\bar{\psi}(x, y, p) = \frac{1}{\Delta x \, \Delta y \, \Delta p}\int_{x-\frac{\Delta x}{2}}^{x+\frac{\Delta x}{2}}\int_{y-\frac{\Delta y}{2}}^{y+\frac{\Delta y}{2}}\int_{p-\frac{\Delta p}{2}}^{p-\frac{\Delta p}{2}} \psi \quad dx\, dy\, dp.$$

where Δx, Δy and Δp are the grid spacing in the x, y and p directions, respectively. The primed quantity is the deviation of ψ from $\overline{\psi}$. It is easily seen that $\overline{\psi'} = 0$. Due to discrete sampling, atmospheric information is not in a continuous form. The value at each grid point is often assumed to be representative of a spatial average. The atmospheric motion, therefore, can be divided into two parts. The part defined by grid point numbers will be called the grid scale, and the part which may occur in nature but cannot be resolved by the grid will be called the subgrid scale.

The amount of APE can be expressed in the following form (Lorenz, 1955),

$$A = \frac{C_p\, 1000^{-\kappa}}{\sigma g\,(1+\kappa)} \iint_0^\infty \left(p^{1+\kappa} - p_r^{1+\kappa} \right) d\theta\, d\sigma \qquad \text{(B.31)}$$

Let $\overline{A}$ represent the amount of APE which would exist if the field of mass only contained the grid scale motion, and A' the excess of A over $\overline{A}$. Then,

$$\overline{A} = \frac{C_p\, 1000^{-\kappa}}{\sigma g\,(1+\kappa)} \iint_0^\infty \left(\overline{p}^{\,1+\kappa} - p_r^{1+\kappa} \right) d\theta\, d\sigma, \qquad \text{(B.32)}$$

$$A' = \frac{C_p\, 1000^{-\kappa}}{\sigma g\,(1+\kappa)} \iint_0^\infty \left(p^{1+\kappa} - \overline{p}^{\,1+\kappa} \right) d\theta\, d\sigma. \qquad \text{(B.33)}$$

Meanwhile,

$$\overline{K} = \frac{1}{\sigma g} \iint_0^{p_s} \frac{1}{2}\, \overline{\mathbb{V}} \cdot \overline{\mathbb{V}}\; dp\, d\sigma, \qquad \text{(B.34)}$$

$$K' = \frac{1}{\sigma g} \iint_0^{p_s} \frac{1}{2}\, \overline{\mathbb{V}' \cdot \mathbb{V}'}\; dp\, d\sigma. \qquad \text{(B.35)}$$

Decomposition of (B.9), (B.25) and (B.29) gives,

$$\begin{aligned}\frac{\delta\bar{A}}{\delta t} = &-\frac{\bar{A}}{\sigma}\frac{\delta\sigma}{\delta t} + \frac{1}{\sigma g}\int\bar{\epsilon}\bar{Q}\,dV + \frac{1}{\sigma g}\int\bar{\alpha}\bar{\omega}\,dV - \frac{c_p}{\sigma g}\int\frac{\bar{T}}{p^\kappa}\frac{\delta\bar{P}_r^\kappa}{\delta t}\,dV\\ &-\frac{c_p}{\sigma g}\int\frac{\bar{T}}{p^\kappa}(\bar{\mathbb{V}}-\bar{\mathbb{W}})\cdot\nabla\bar{P}_r^\kappa\,dV - \frac{c_p}{\sigma g}\int\frac{\bar{T}}{p^\kappa}\bar{\omega}\frac{\partial\bar{P}_r^\kappa}{\partial p}\,dV - \frac{c_p}{\sigma g}\int\nabla\cdot[\bar{\epsilon}\bar{T}(\bar{\mathbb{V}}-\bar{\mathbb{W}})]\,dV\\ &-\frac{c_p}{\sigma g}\int\frac{\partial}{\partial p}(\bar{\epsilon}\bar{T}\bar{\omega})\,dV + \frac{c_p}{\sigma g}\int\bar{\epsilon}_s\bar{T}_s\frac{\delta P_s}{\delta t}\,d\sigma + RA_I, \qquad \text{(B.36)}\end{aligned}$$

$$\begin{aligned}\frac{\delta\bar{A}}{\delta t} = &-\frac{\bar{A}}{\sigma}\frac{\delta\sigma}{\delta t} + \frac{1}{\sigma g}\int\bar{\epsilon}\bar{Q}\,dV + \frac{1}{\sigma g}\int\bar{\epsilon}\bar{\alpha}\bar{\omega}\,dV - \frac{c_p}{\sigma g}\int\bar{\epsilon}(\bar{\mathbb{V}}-\bar{\mathbb{W}})\cdot\nabla\bar{T}\,dV\\ &-\frac{c_p}{\sigma g}\int\bar{\epsilon}\bar{\omega}\frac{\partial\bar{T}}{\partial p}\,dV + \frac{c_p}{\sigma g}\int\bar{T}\frac{\delta\bar{\epsilon}}{\delta t}\,dV + \frac{c_p}{\sigma g}\int\bar{\epsilon}_s\bar{T}_s\frac{\delta P_s}{\delta t}\,d\sigma + RA_{II}. \qquad \text{(B.37)}\end{aligned}$$

$$\begin{aligned}\frac{\delta\bar{K}}{\delta t} = &-\frac{\bar{K}}{\sigma}\frac{\delta\sigma}{\delta t} - \frac{1}{\sigma g}\int\bar{\mathbb{V}}\cdot\nabla\bar{\phi}\,dV - \frac{1}{\sigma g}\int\nabla\cdot[\bar{k}(\bar{\mathbb{V}}-\bar{\mathbb{W}})]\,dV\\ &-\frac{1}{\sigma g}\int\frac{\partial}{\partial p}(\bar{k}\bar{\omega})\,dV + \frac{1}{\sigma g}\int\bar{k}_s\frac{\delta P_s}{\delta t}\,d\sigma + RK, \qquad \text{(B.38)}\end{aligned}$$

where dV = dx·dy·dp,

$$P_r^\kappa \simeq \bar{P}_r^\kappa + \kappa P_r'\bar{P}_r^{\kappa-1},$$

$$\begin{aligned}RA_I = &-\frac{\delta A'}{\delta t} - \frac{A'}{\sigma}\frac{\delta\sigma}{\delta t} + \frac{c_p}{\sigma g}\int\Big\{\frac{\overline{\epsilon'Q'}}{c_p} + \frac{\overline{\alpha'\omega'}}{c_p} - \frac{1}{p^\kappa}\overline{T'\frac{\delta}{\delta t}(\kappa P_r'\bar{P}_r^{\kappa-1})}\\ &-\frac{\bar{T}}{p^\kappa}[\overline{(\mathbb{V}'-\mathbb{W}')\cdot\nabla(\kappa P_r'\bar{P}_r^{\kappa-1})}] - \frac{(\bar{\mathbb{V}}-\bar{\mathbb{W}})}{p^\kappa}\cdot[\overline{T'\nabla(\kappa P_r'\bar{P}_r^{\kappa-1})}]\\ &-\frac{1}{p^\kappa}[\overline{T'(\mathbb{V}'-\mathbb{W}')}]\cdot\nabla\bar{P}_r^\kappa - \frac{1}{p^\kappa}[\overline{T'(\mathbb{V}'-\mathbb{W}')\cdot\nabla(\kappa P_r'\bar{P}_r^{\kappa-1})}]\\ &-\frac{\bar{T}}{p^\kappa}\overline{\omega'\frac{\partial}{\partial p}(\kappa P_r'\bar{P}_r^{\kappa-1})} - \frac{\bar{\omega}}{p^\kappa}\overline{T'\frac{\partial}{\partial p}(\kappa P_r'\bar{P}_r^{\kappa-1})}\\ &-\frac{1}{p^\kappa}\overline{T'\omega'}\frac{\partial\bar{P}_r^\kappa}{\partial p} - \frac{1}{p^\kappa}\overline{T'\omega'\frac{\partial}{\partial p}(\kappa P_r'\bar{P}_r^{\kappa-1})}\\ &-\nabla\cdot[\bar{\epsilon}\,\overline{T'(\mathbb{V}'-\mathbb{W}')} - \bar{T}\,\overline{\epsilon'(\mathbb{V}'-\mathbb{W}')} - \overline{\epsilon'T'}(\bar{\mathbb{V}}-\bar{\mathbb{W}}) - \overline{\epsilon'T'(\mathbb{V}'-\mathbb{W}')}]\\ &-\frac{\partial}{\partial p}[\bar{\epsilon}\,\overline{T'(\omega'-\tilde{\omega}')} - \bar{T}\,\overline{\epsilon'(\omega'-\tilde{\omega}')} - \overline{\epsilon'T'}(\bar{\omega}-\bar{\tilde{\omega}}) - \overline{\epsilon'T'(\omega'-\tilde{\omega}')}]\Big\}\,dV, \qquad \text{(B.39)}\end{aligned}$$

$$\begin{aligned} RA_{II} = {} & -\frac{\delta A'}{\delta t} - \frac{A'}{\sigma}\frac{\delta \sigma}{\delta t} + \frac{C_p}{\sigma g}\int \Big\{ \frac{\overline{\epsilon' Q'}}{C_p} + \frac{\bar{\epsilon}\,\overline{\alpha'\omega'}}{C_p} + \frac{\bar{\alpha}\,\overline{\epsilon'\omega'}}{C_p} + \frac{\bar{\omega}\,\overline{\epsilon'\alpha'}}{C_p} \\ & + \frac{\overline{\epsilon'\alpha'\omega'}}{C_p} - \bar{\epsilon}\,\overline{(\mathbb{V}' - \mathbb{W}')\cdot\nabla T'} - (\bar{\mathbb{V}} - \bar{\mathbb{W}})\cdot\overline{\epsilon'\nabla T'} - \overline{\epsilon'(\mathbb{V}' - \mathbb{W}')}\cdot\nabla\bar{T} \\ & - \overline{\epsilon'(\mathbb{V}' - \mathbb{W}')\cdot\nabla T'} - \bar{\epsilon}\,\overline{\omega'\frac{\partial T'}{\partial p}} - \bar{\omega}\,\overline{\epsilon'\frac{\partial T'}{\partial p}} - \overline{\epsilon'\omega'}\frac{\partial \bar{T}}{\partial p} \\ & - \overline{\epsilon'\omega'\frac{\partial T'}{\partial p}} + \overline{T'\frac{\delta \epsilon'}{\delta t}} \Big\}\, dV + \frac{C_p}{\sigma g}\int \overline{\epsilon_s' T_s'}\,\frac{\delta p_s}{\delta t}\, d\sigma, \end{aligned} \qquad (B.40)$$

$$\begin{aligned} RK = {} & -\frac{\delta K'}{\delta t} - \frac{K'}{\sigma}\frac{\delta \sigma}{\delta t} + \frac{1}{\sigma g}\int \Big\{ -\overline{\mathbb{V}'\cdot\nabla\phi'} - \nabla\cdot[\overline{k'(\mathbb{V}' - \mathbb{W}')}] \\ & - \frac{\partial}{\partial p}[\overline{k'(\omega' - \tilde{\omega}')}] + \bar{\mathbb{V}}\cdot\bar{\mathbb{F}} + \overline{\mathbb{V}'\cdot\mathbb{F}'} \Big\}\, dV. \end{aligned} \qquad (B.41)$$

Eqs. (B.36), (B.37) and (B.38) are referred to in the main text as APE budget I, APE budget II and KE budget, respectively. In symbolic form, the three budget equations are,

$$\begin{aligned} DADT = {} & DAREAA + GA + AW + DPRDT + HAPR + VAPR + HEA \\ & + VFA + DPSA + RA_I \end{aligned} \qquad (B.42)$$

$$\begin{aligned} DADT = {} & DAREAA + GA + EAW + EHAT + EVAT + DEDT \\ & + DPSA + RA_{II} \end{aligned} \qquad (B.43)$$

$$DKDT = DAREAK + GK + HFK + VFK + DPSK + RK\ . \qquad (B.44)$$

Table 1. Estimates of total and component generation of available potential energy (W m^{-2}) obtained at the University of Wisconsin for several storms (Johnson, 1970).

	Latent heat	Sensible heat	Infrared	Short-wave	Total	Boundary frictional dissipation
Hurricane Hilda[1]						
Anthes and Johnson (1968)						
Mature, 1200 GMT, 1/10/64	2.5		0.6	0.2	3.3	-
Extratropical cyclone[2]						
Bullock and Johnson (1971)						
Incipient 1200 GMT, 25/3/64	0.9	-	0.9	-	1.8	3.1
Mature, 0000 GMT, 26/3/64	8.0	-	1.2	-	9.2	5.1
Occluded, 1200 GMT, 26/3/64	6.0	-	1.1	-	7.1	9.1
Extratropical cyclone[2]						
Gall and Johnson (1971)						
Mature, 1200 GMT, 14/2/68						
Upper estimate		6.1				7.1
Lower estimate		3.1				

[1] Radius of storm area 1000 km.

[2] Radius of storm area 1700 km.

Table 2. The observed and estimated precipitation rates (x 10^{-2} mm hr^{-1}) at station 47678. The subscripts S and C represent stable and convective, respectively. The total precipitation rate P is the sum of the stable component estimated by Krishnamurti's method and the convective component. N represents the total cloud coverage, N_h is the cloud coverage for the low and/or middle clouds, C_L, C_M and C_H indicate the low, middle and high cloud types, respectively, and ww represent the present weather. A dash indicates missing data.

Date/Time	Observed P	N	N_h	C_L	C_M	C_H	ww	Krish. P_S	Haltiner P_S	Kuo P_C	Total $P = P_S + P_C$
13/00	0	6	6	△	0	0		0	0	0	0
13/06		1	1	⌓	0	0					
13/12	-	0	0	0	0	0	-○-	0	0	0	0
13/18		0	0	0	0	0	-○-				
14/00	46	6	1	⌓	ω	0	○̍	23	26	0	23
14/06		8	2	---	∠	-	○̍				
14/12	174	8	8	△	-	-	▽̇	23	37	0	23
14/18		8	8	△	-	-	▽̇				
15/00	206	8	8	△	-	-	▽̇	17	27	0	17
15/06		5	5	△	0	0	○̩				
15/12	-	1	1	⌓	0	0	○̩	0	0	0	0
15/18		2	2	△	0	0	○̍				

Table 3. Same as Table 2 except for station 47778.

Date/Time	Observed P	N	N_h	C_L	C_M	C_H	ww	Krish. P_S	Haltiner P_S	Kuo P_C	Total $P = P_S + P_C$
13/00	-	1	1	⌓	0	0		0	0	0	0
13/06		1	1	⌓	0	0					
13/12	0	1	0	0	0	↪	-○-	0	0	0	0
13/18		0	0	0	0	0	-○-				
14/00	17	8	1	⌓	∠	-	○̍	0	0	0	0
14/06		8	2	---	∡	-	••				
14/12	75	8	3	---	∡	-	••	23	45	0	23
14/18		8	2	△	∠ω	-	•]				
15/00	75	2	2	△	0	↪	-○-	0	0	0	0
15/06		5	5	△	0	0	○̩				
15/12	-	1	1	⌓	0	0	-○-	0	0	0	0
15/18		1	1	⌓	0	0	○̩				

Table 4. Same as Table 2 except for station 47827.

Date/Time	Observed P	N	N_h	C_L	C_M	C_H	ww	Krish. P_S	Haltiner P_S	Kuo P_C	Total $P = P_S + P_C$
13/00	0	0	0	0	0	0		0	0	0	0
13/06		2	1	0	ω	⌐					
13/12	0	3	3	0	ω	0	○	18	25	0	18
13/18		8	3	△	∡	-	○				
14/00	75	8	6	---	∠	-	∴	19	30	0	19
14/06		8	8	△	-	-	∇̇				
14/12	-	8	2	---	∠	-	••	0	0	0	0
14/18		0	0	0	0	0	○				
15/00	-	6	6	△	0	0	○	0	0	0	0
15/06		1	1	⌓	0	0	○				
15/12	-	0	0	0	0	0	○	0	0	0	0
15/18		1	1	⌓	0	0	○				

Table 5. Same as Table 2 except for station 47945.

Date/Time	Observed P	N	N_h	C_L	C_M	C_H	ww	Krish. P_S	Haltiner P_S	Kuo P_C	Total $P = P_S + P_C$
13/00	39	8	4	△	ω	-		2	1	0	2
13/06		8	5	---	∠	-					
13/12	-	8	4	---	∠	-	••	38	44	0	38
13/18		7	7	△	-	-	•▽]				
14/00	-	7	4	△	ω	-	○	78	73	0	78
14/06		7	6	△	ω	-	○				
14/12	-	8	6	⧖	ω	-	•▽	92	98	0	92
14/18		7	7	△	-	-	○				
15/00	-	6	6	△	-	-	○	5	4	0	5
15/06		6	6	⟁	0	0	-				
15/12	-	7	7	△	-	-	○	3	2	0	3
15/18		6	6	△	0	0	○				

Table 6. Same as Table 2 except for station 47909.

Date/Time	Observed P	N	N_h	C_L	C_M	C_H	ww	Krish. P_S	Haltiner P_S	Kuo P_C	Total $P = P_S + P_C$
13/00	0	6	6	⌂	0	0		0	0	0	0
13/06		7	4	⌂	ω	0					
13/12	133	8	8	⌂	–	–	Ó	2	2	0	2
13/18		8	8	⌂	–	–	∇̇				
14/00	408	8	8	⌂	–	–	∇̇	161	176	405	566
14/06		8	8	0	∠	–	•]				
14/12	–	7	7	⌂	–	–	∇̇]	0	0	0	0
14/18		8	8	⌂	–	–	∇̇				
15/00	–	7	7	⌂	–	–	∇̇]	0	0	0	0
15/06		2	2	⌂	0	0	Q				
15/12	–	7	7	⌂	0	0	∇̇]	0	0	0	0
15/18		7	7	⌂	–	–	∇̇]				

Table 7. Same as Table 2 except for station 47936.

Date/Time	Observed P	N	N_h	C_L	C_M	C_H	ww	Krish. P_S	Haltiner P_S	Kuo P_C	Total $P = P_S + P_C$
13/00	0	7	7	△	ω	0		0	0	0	0
13/06		5	2	△	ω	0					
13/12	22	7	3	△	ω	–	○	50	54	0	50
13/18		8	7	△	ϭ	–	▽̇				
14/00	361	7	7	△	ϭ	–	○	136	126	279	415
14/06		8	7	⧖	ϭ	–	▽̇				
14/12	–	6	6	△	0	0	ϙ	30	33	0	30
14/18		2	2	△	0	0	○				
15/00	–	6	6	△	0	0	○	0	0	0	0
15/06		6	6	◡	0	–	○				
15/12	–	7	7	△	–	–	○	5	5	0	5
15/18		6	6	△	0	0	○				

Table 8. Same as Table 2 except for station 47927.

Date/Time	Observed P	N	N_h	C_L	C_M	C_H	ww	Krish. P_S	Haltiner P_S	Kuo P_C	Total $P = P_S + P_C$
13/00	0	7	6	$\tilde{\Delta}$	ω	-		3	2	0	3
13/06		7	7	Δ	-	-					
13/12	11	8	6	Δ	ꝏ	-	$\dot{\nabla}$	74	73	0	74
13/18		8	6	Δ	ꝏ	-	$\dot{\nabla}$]				
14/00	447	8	6	Δ	ꝏ	-	$\dot{\nabla}$	139	136	428	567
14/06		8	6	Δ	ꝏ	-	$\dot{\nabla}$				
14/12	0	6	6	Δ	0	0	○	7	6	0	7
14/18		6	5	Δ	ꝏ	0	○				
15/00	0	7	7	Δ	0	0	○	0	0	0	0
15/06		7	7	Δ	-	-	○				
15/12	-	8	8	Δ	-	-	$\dot{\nabla}$	0	0	0	0
15/18		7	7	Δ	-	-	○				

Table 9. Same as Table 2 except for station 47918.

Date/Time	Observed P	N	N_h	C_L	C_M	C_H	ww	Krish. P_S	Haltiner P_S	Kuo P_C	Total $P = P_S + P_C$
13/00	13	7	4	△	ω	0		10	9	0	10
13/06		6	6	△	0	0					
13/12	4	5	2	△	ω	0	∇̇]	73	67	129	202
13/18		7	7	△	-	-	-○-				
14/00	142	7	4	⧖	ϭ	-	∇̇	78	83	0	78
14/06		7	2	∼	ϭ	-	-○-				
14/12	0	6	6	△̆	0	0	-○-	7	6	0	7
14/18		7	7	△	-	-	-○-				
15/00	0	7	7	-○-	0	0	-○-	0	0	0	0
15/06		6	6	△̆	0	0	-○-				
15/12	-	7	7	△̆	-	-	∇̇]	0	0	0	0
15/18		7	7	△̆	-	-	-○-				

Table 10. The estimates of the drag coefficient, sensible and latent heat fluxes (ly day^{-1}) and the Bowen ratio, averaged over the 5 x 7 grid mesh shown in Fig. 23.

Date/Time	C_D	F_S	LE	F_S + LE	B
13/00	1.71×10^{-3}	220	712	932	0.33
13/12	1.71×10^{-3}	178	588	766	0.28
14/00	1.88×10^{-3}	177	540	717	0.23
14/12	1.98×10^{-3}	343	965	1308	0.32
15/00	1.88×10^{-3}	436	1247	1683	0.35
15/12	1.83×10^{-3}	357	1013	1370	0.34
Average	1.83×10^{-3}	285	844	1129	0.31

Table 11. The bulk transfer coefficients estimated by Mitsuta, Mongi and Tsukomoto (1977) using all of the AMTEX flux measurements except the on-land tower measurements when the wind was from inland.

	Non-neutral Stability	Neutral Stability
C_D (momentum)	1.52×10^{-3}	1.33×10^{-3}
C_H (heat)	2.63×10^{-3}	2.18×10^{-3}
C_E (moisture)	2.15×10^{-3}	1.97×10^{-3}

Table 12. Estimates of the sensible and latent heat fluxes (ly day^{-1}) made over the AMTEX region.

	F_S	LE	F_S + LE	B
AMTEX'75 flux measurements				
Miyakojima	279	1433	1712	0.19
Taramajima	201	964	1165	0.21
Ninomiya (1972)				
budget calculation	340	640	980	0.53
aerodynamic method	270	660	930	0.39
Agee and Howley (1977)				
warm period	49	182	231	0.27
cold period	485	1099	1584	0.44
14-day period	174	472	646	0.37
Amburn (1976), Method 2				
warm period	19	80	99	0.24
cold period	281	367	648	0.77
14-day period	111	182	293	0.61
Amburn (1976), Method 3				
warm period	73	286	359	0.26
cold period	1040	1491	2531	0.70
14-day period	418	717	1135	0.58

Table 13. The estimates of the drag coefficient, sensible and latent heat fluxes (ly day^{-1}) and the Bowen ratio, averaged within the storm volumes.

Date/Time	C_D	F_S	LE	F_S + LE	B
13/00	1.65×10^{-3}	138	518	656	0.32
13/12	1.55×10^{-3}	104	404	508	0.29
14/00	1.68×10^{-3}	113	421	534	0.27
14/12	1.83×10^{-3}	188	615	803	0.28
15/00	1.96×10^{-3}	246	628	874	0.55
15/12	2.06×10^{-3}	230	553	783	0.49

Table 14. Net radiational cooling rates (K day^{-1}) from surface to 100 mb and from surface to 850 mb for eight different cloud combinations.

Cloud Type	Cooling rate$]_{sfc}^{100}$	Cooling rate$]_{sfc}^{850}$
$S_c + A_c$	1.56	2.10
S_c	1.40	2.30
A_c	1.25	0.45
$S_c + A_c + C_i$	1.06	1.50
$S_c + C_i$	0.95	1.58
$A_c + C_i$	0.84	0.60
Clear	0.80	1.26
C_i	0.44	0.55

Table 15. The ratios (%) of APE to TPE and KE to APE for the AMTEX storm in comparison with those for the general circulation (Holton, 1972).

Date/Time	13/00	13/12	14/00	14/12	15/00	15/12	Global
$\frac{\text{APE}}{\text{TPE}}$	0.52	0.52	0.71	0.41	0.32	0.12	0.5
$\frac{\text{KE}}{\text{APE}}$	44	40	29	57	74	155	20

Table 16. The available potential energy budget I (W m^{-2}) of the AMTEX storm.

Date/Time	13/00	13/12	14/00	14/12	15/00	15/12	Average
DADT	1.5	53.6	-30.0	-111.6	-81.9	-106.4	-45.8
DAREAA	0.0	0.0	-1.7	-15.5	-15.0	-3.8	-6.0
GA	3.0	2.4	7.4	4.9	14.0	1.5	5.5
AW	-171.8	-330.9	-370.6	-254.3	-347.5	-260.1	-289.2
DPRDT	76.1	65.4	30.7	-25.3	-11.7	-43.8	29.8
HAPR	137.4	-559.8	-391.9	975.2	836.3	-304.2	115.5
VAPR	67.7	319.4	307.8	163.7	229.7	135.3	203.9
HFA	35.2	601.2	512.8	-768.1	-630.4	501.1	42.0
VFA	18.6	9.8	11.4	5.5	-0.0	0.0	7.6
DPSA	-1.9	-3.0	-5.2	-12.7	-22.2	-22.3	-11.2
RA_I	-162.8	-50.8	-130.5	-185.0	-135.3	-197.8	-143.7
HFA + HAPR	172.6	41.3	120.9	207.1	205.9	196.9	157.5

Table 17. The available potential energy budget II (W m^{-2}) of the AMTEX storm.

Date/Time	13/00	13/12	14/00	14/12	15/00	15/12	Average
DADT	1.5	53.6	-30.0	-111.6	-81.9	-106.4	-45.8
DAREAA	0.0	0.0	-1.7	-15.5	-15.0	-3.8	-6.0
GA	3.0	2.4	7.4	4.9	14.0	1.5	5.5
EAW	-23.0	-2.2	-18.6	-35.5	-23.9	-20.1	-20.6
EHAT	7.4	9.8	13.6	45.9	6.2	-11.2	12.0
EVAT	12.7	1.4	10.6	19.4	12.9	10.4	11.2
DEDT	73.1	62.8	26.8	-34.2	-22.6	34.1	23.3
DPSA	-1.9	-3.0	-5.2	-12.7	-22.2	-22.3	-11.2
RA_{II}	-70.0	-17.6	-62.8	-84.0	-31.4	-95.0	-60.1

Table 18. The kinetic energy budget (W m^{-2}) of the AMTEX storm.

Date/Time	13/00	13/12	14/00	14/12	15/00	15/12	Average
DKDT	-10.9	-6.4	7.3	6.5	-14.8	-26.3	-7.4
DAREAK	0.0	0.0	-0.5	-8.9	-11.1	-5.9	-4.4
GK	16.8	32.2	33.0	27.5	19.2	10.9	23.3
HFK	-100.6	-70.9	-51.7	-21.5	-7.2	26.0	-37.7
VFK	-0.3	-0.2	-0.0	0.1	0.0	0.0	-0.1
DPSK	-0.0	-0.0	-0.0	-0.1	-0.2	-0.2	-0.1
RK	73.2	32.5	26.5	9.4	-15.6	-57.1	11.5
Boundary Frictional Dissipation	-1.1	-0.5	-1.2	-3.1	-4.7	-9.0	-3.3

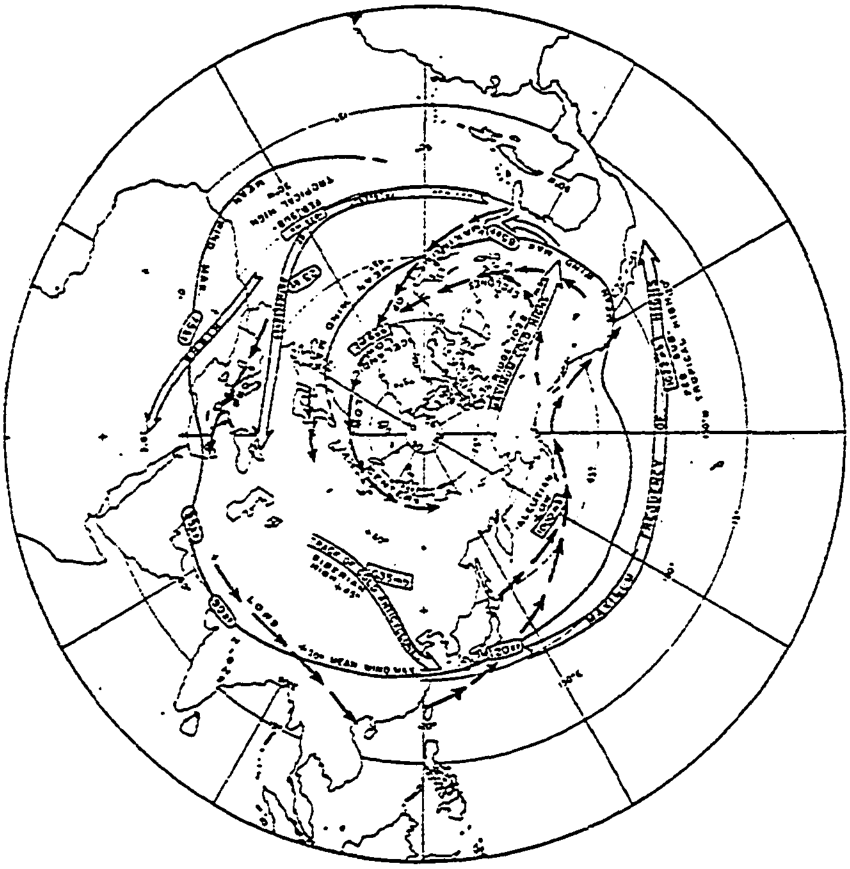

Fig. 1. Axis of mean maximum wind (heavy line) and simplified axes of maximum frequency of occurrence of cyclones (short arrows) and anti-cyclones (double-shafted arrows) based on the maps by Petterssen (1950) for the winter season. Rectangles show mean sea-level pressures in principal semipermanent low and high centers, and ellipses show regions of maximum upper winds. (from Palmen and Newton, 1969)

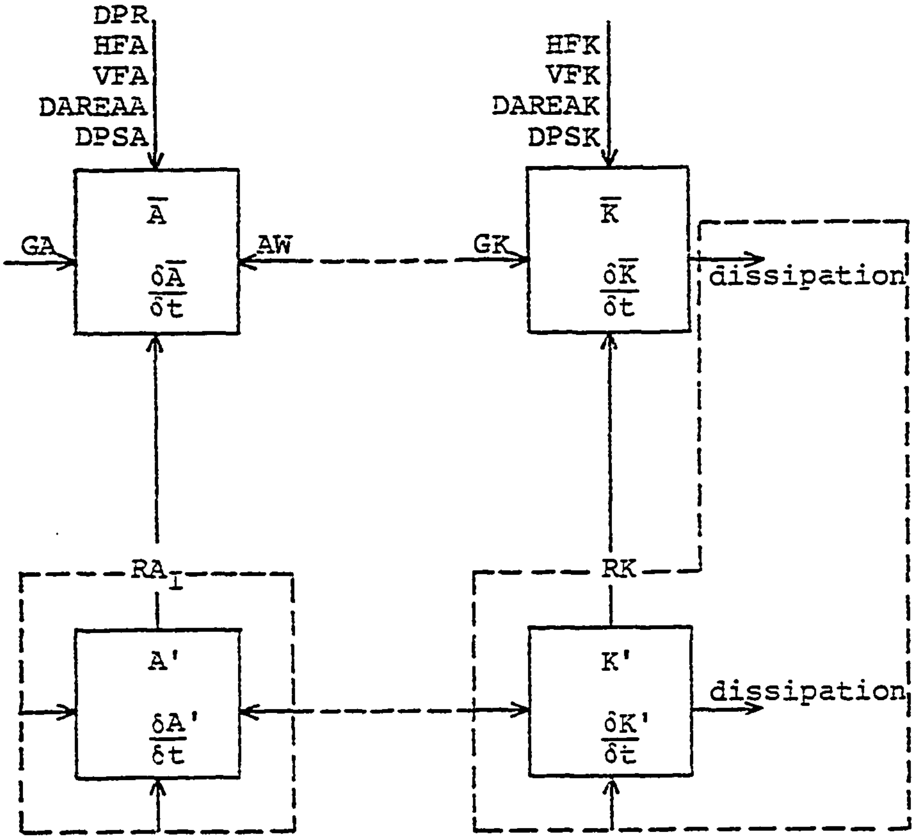

Fig. 2. The energy diagram for an open moving system. The overbar and prime represent the grid and subgrid scales, respectively. The abbreviations for the grid-scale terms are defined in the text of Chapter II. The unlabled arrows within the dashed boxes symbolically represent the individual terms in the equations for RA_I and RK which are defined in Appendix B.

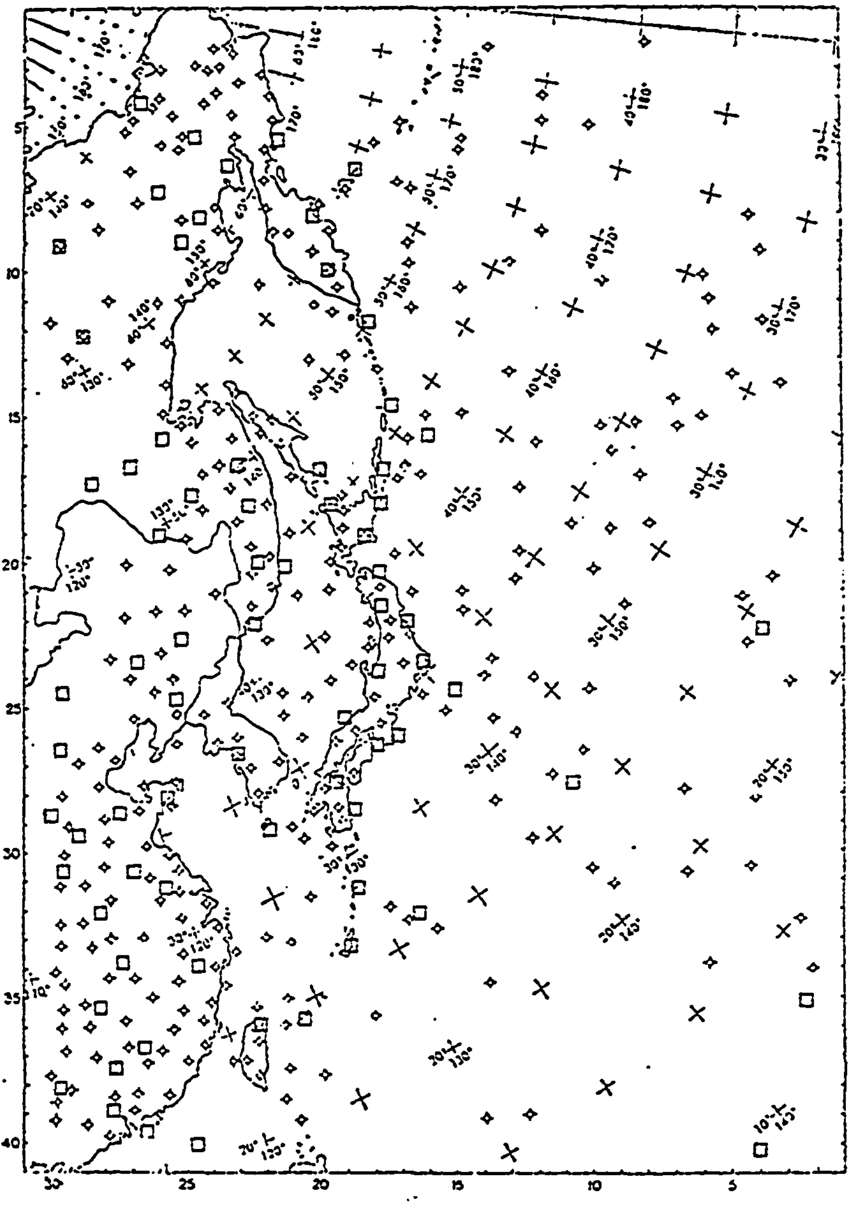

Fig. 3. The objective analysis grid used in this study with surface observations and transient ship reports marked "✧", and upper air observations given by "□". Not all surface observations sites are marked due to the high density in some areas. (from Soliz, 1977)

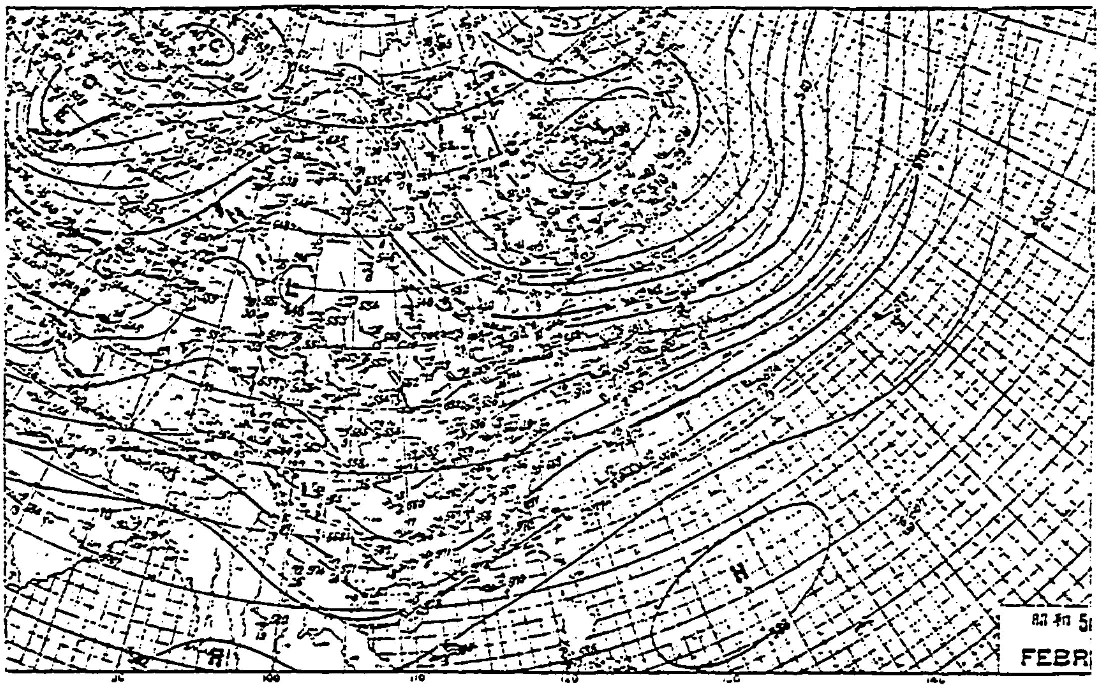

Fig. 4. 500 mb height analysis at 1200 GMT 13 February by Japan Meteorological Agency (JMA).

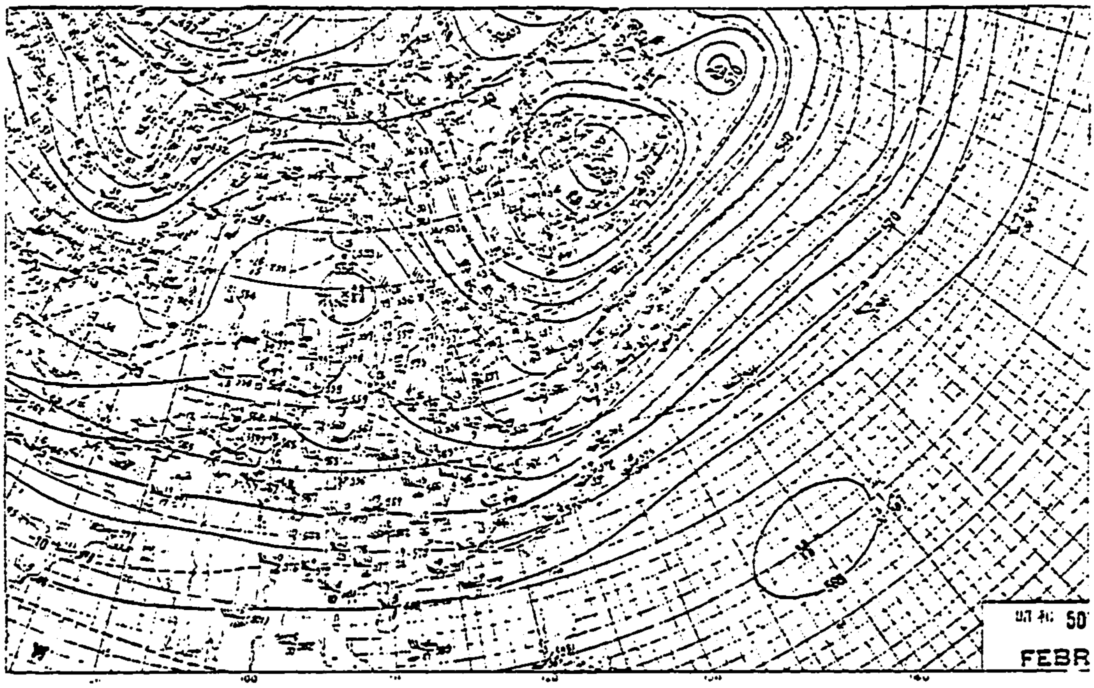

Fig. 5. 500 mb height analysis at 1200 GMT 14 February by JMA.

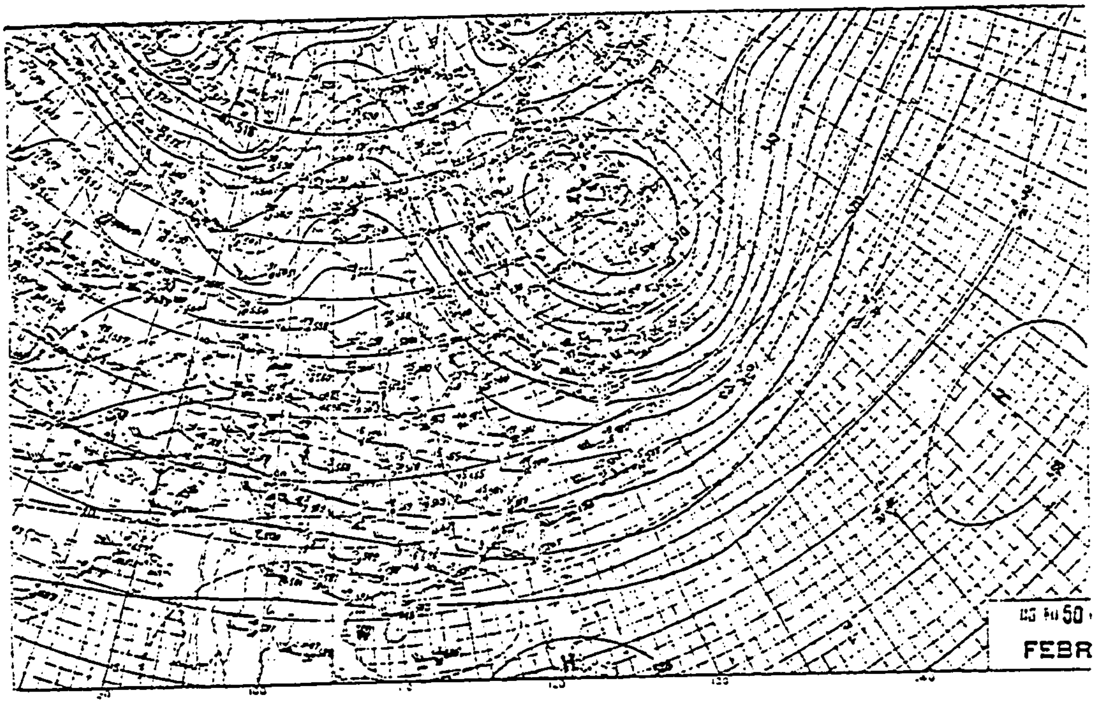

Fig. 6. 500 mb height analysis at 1200 GMT 15 February by JMA.

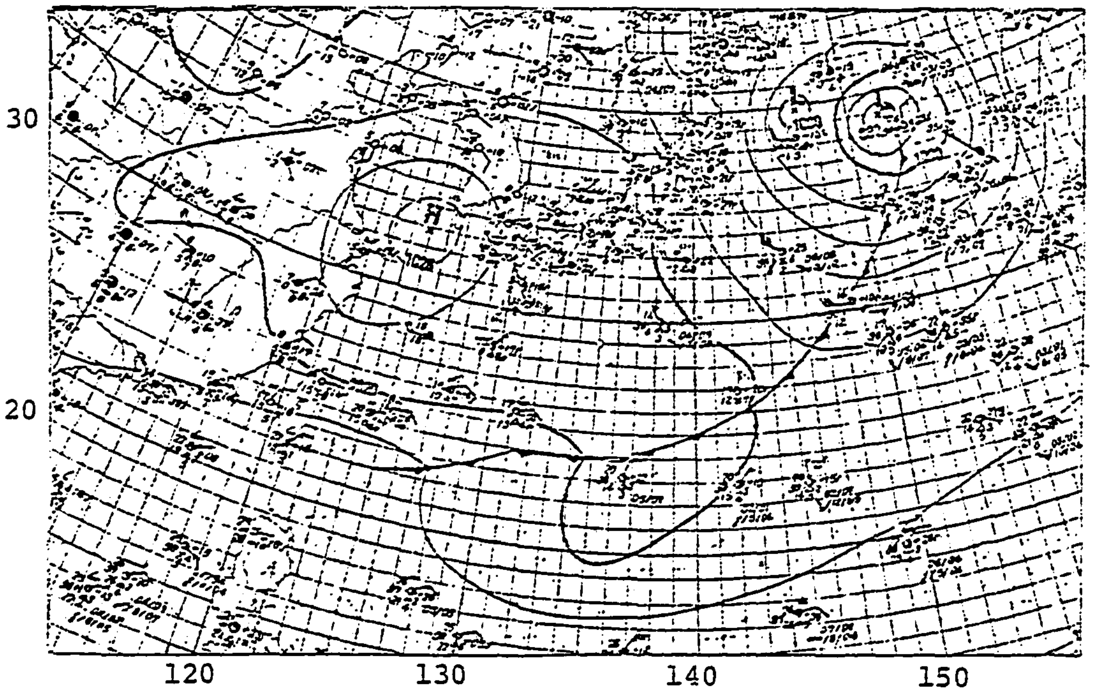

Fig. 7. Surface pressure analysis at 0000 GMT 13 February by JMA.

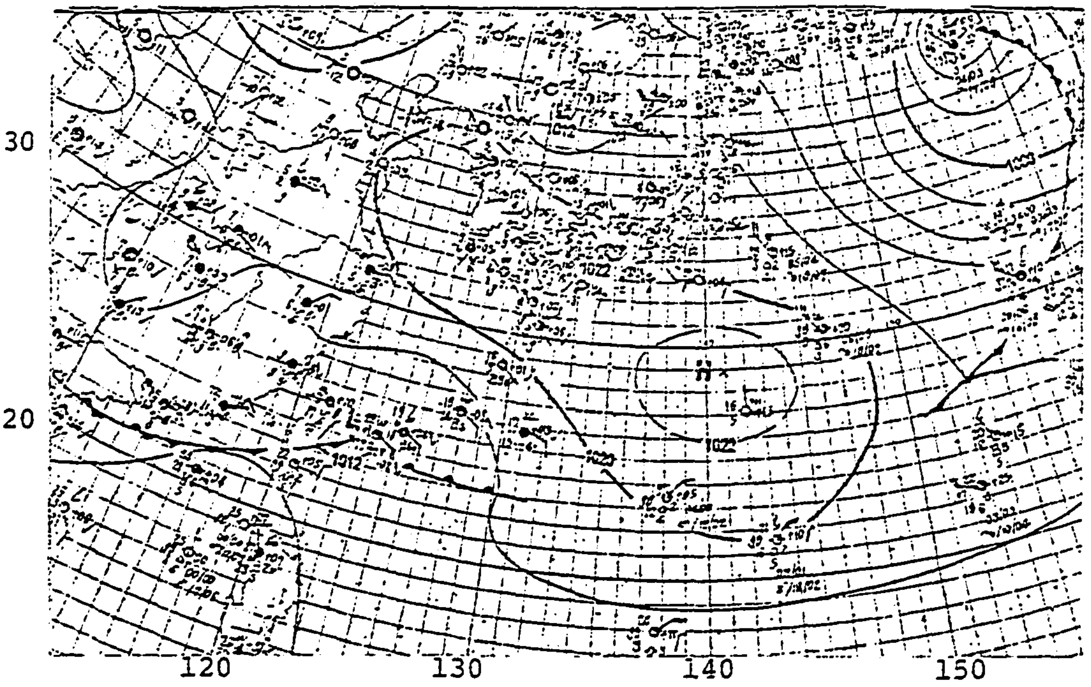

Fig. 8. Surface pressure analysis at 1200 GMT 13 February by JMA.

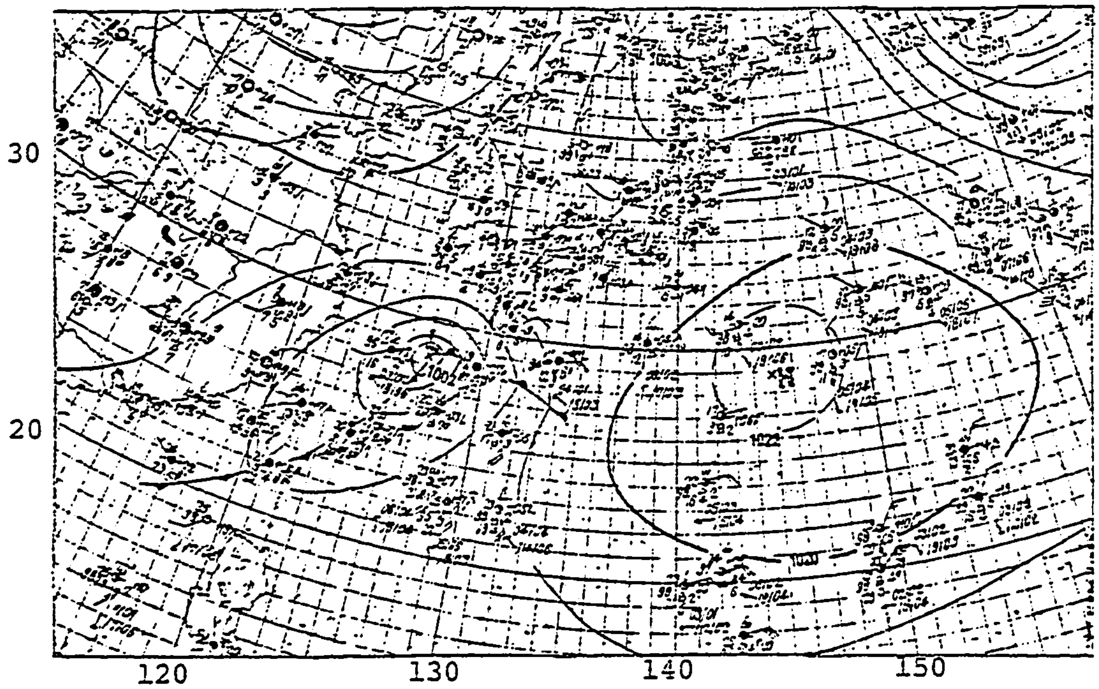

Fig. 9. Surface pressure analysis at 0000 GMT 14 February by JMA.

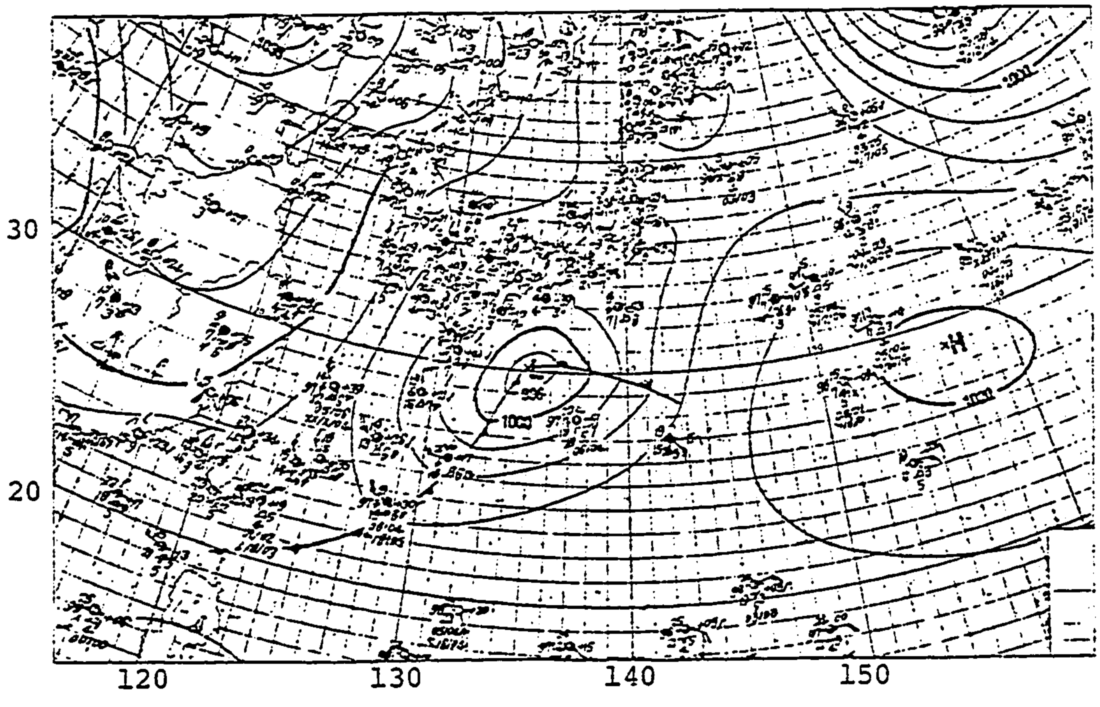

Fig. 10. Surface pressure analysis at 1200 GMT 14 February by JMA.

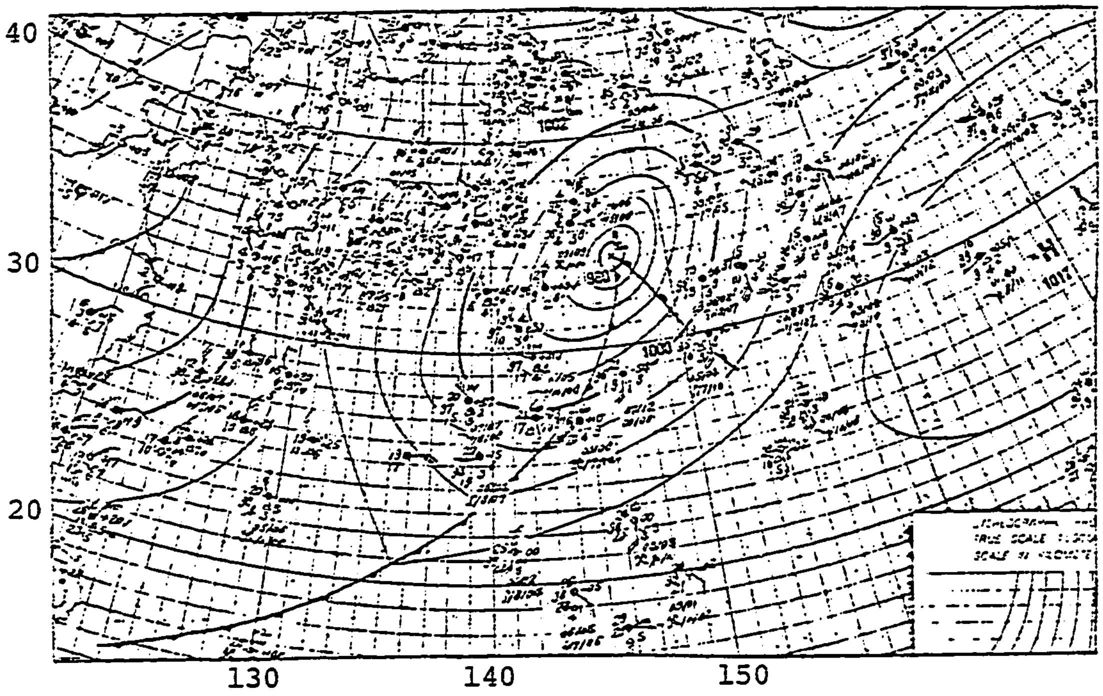

Fig. 11. Surface pressure analysis at 0000 GMT 15 February by JMA.

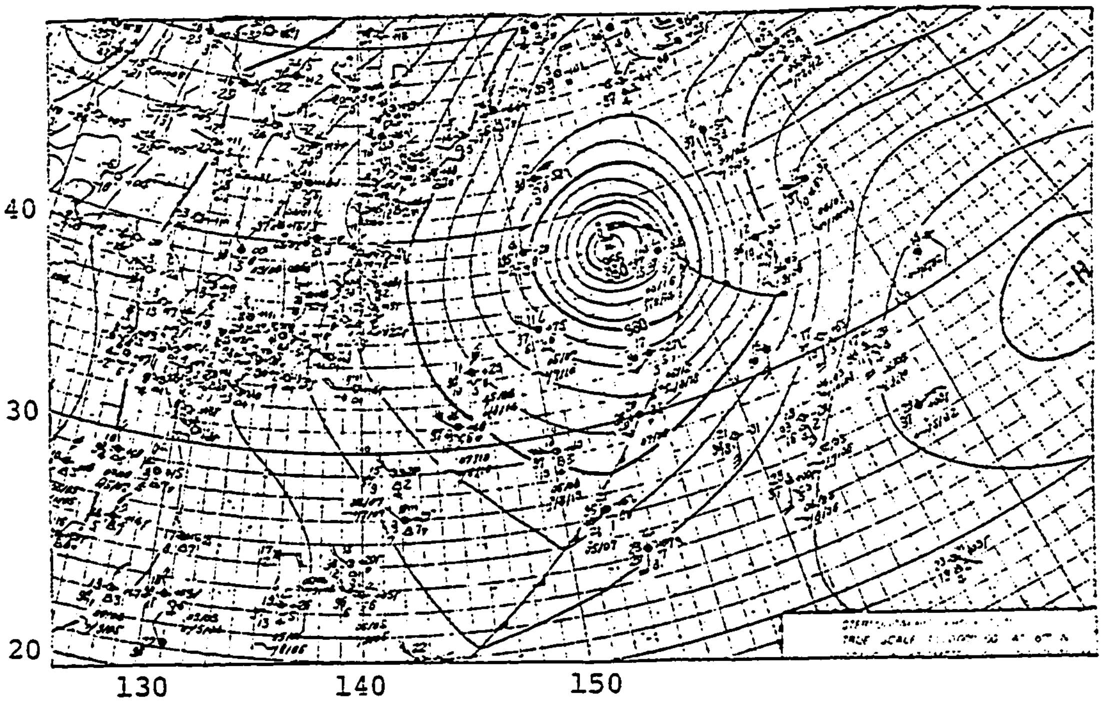

Fig. 12. Surface pressure analysis at 1200 GMT 15 February by JMA.

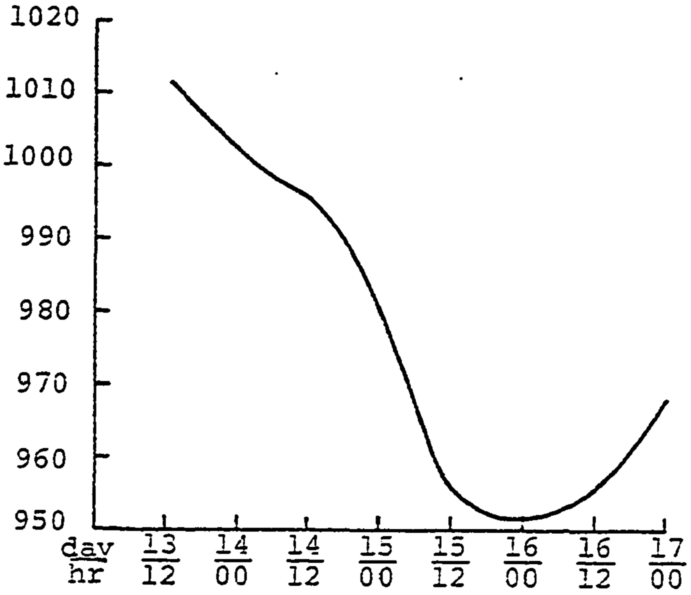

Fig. 13. The surface central pressure (mb) of the AMTEX storm plotted as a function of time.

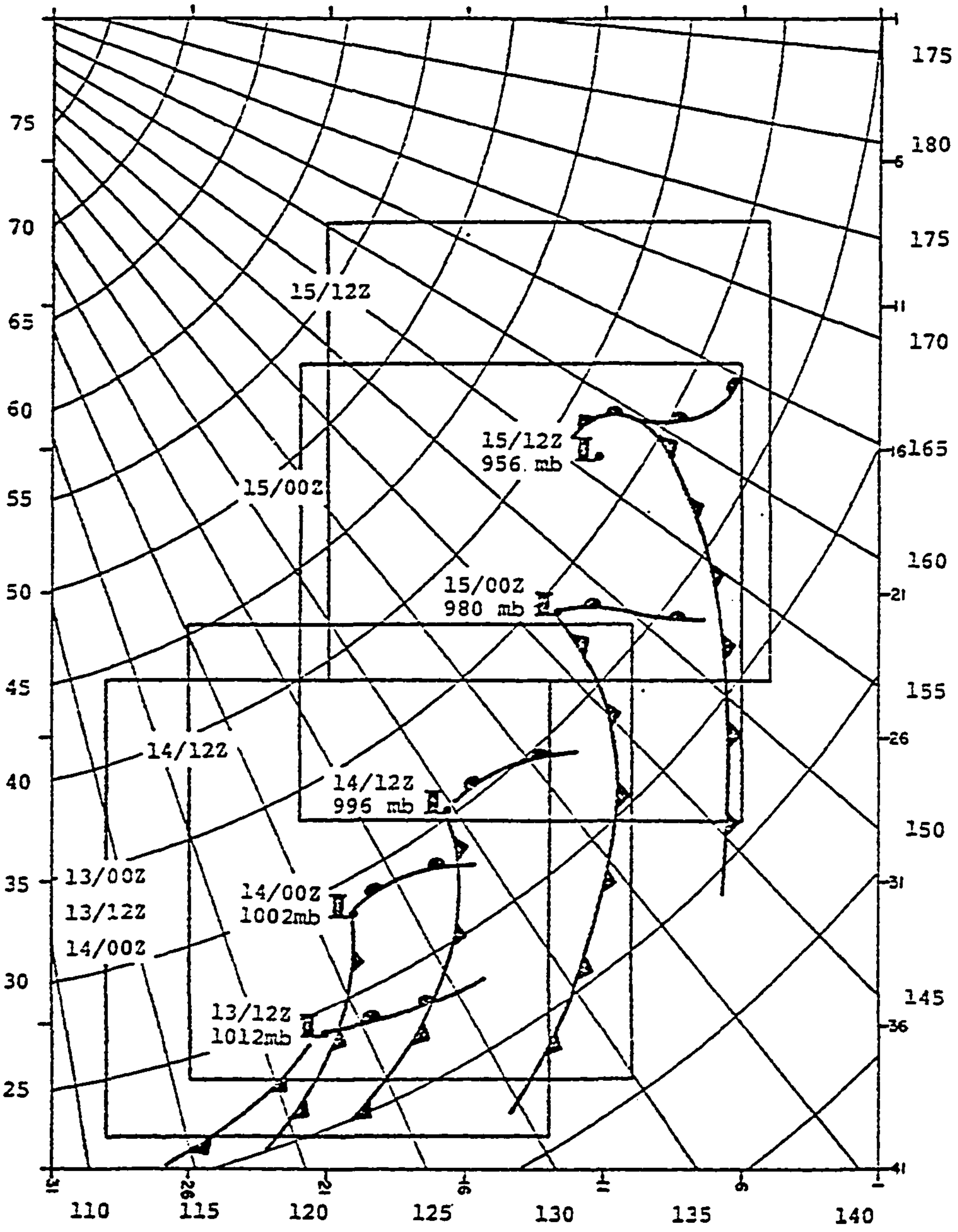

Fig. 14. The square boxes outline the horizontal extent of the storm volumes. The positions of the surface low center and fronts, and the central pressure are also indicated. The large numbers along the right side and bottom are the longitude in degrees; those along the left side are the latitude. The small numbers along the right side and bottom indicate the position of the grid points.

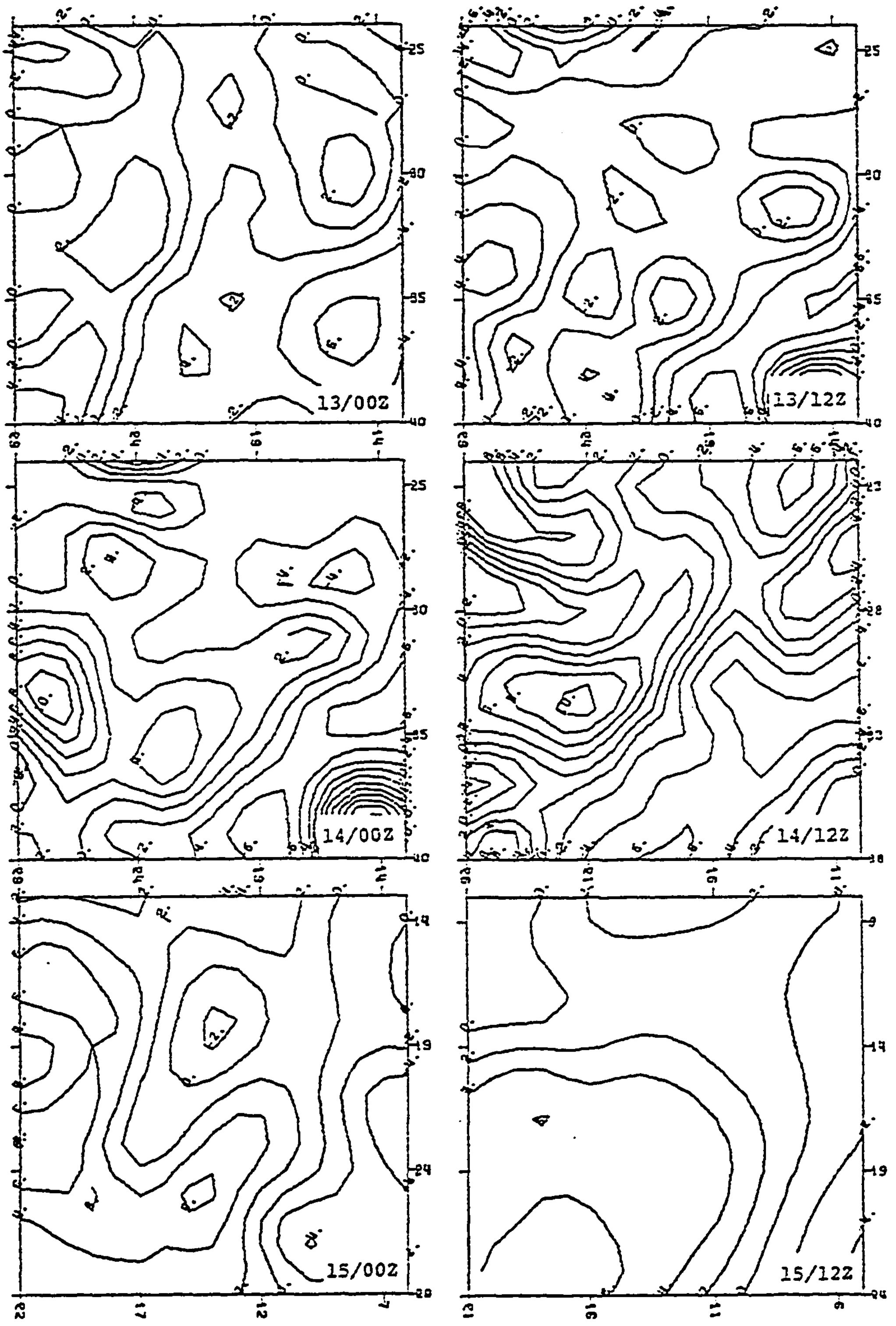

Fig. 15. The analyses of 500 mb relative vorticity ($x\ 10^{-5}\ sec^{-1}$) within the storm volumes. The numbers along the right side and bottom in increments of 5 indicate the position of the grid points in relation to the 31 x 41 analysis grid.

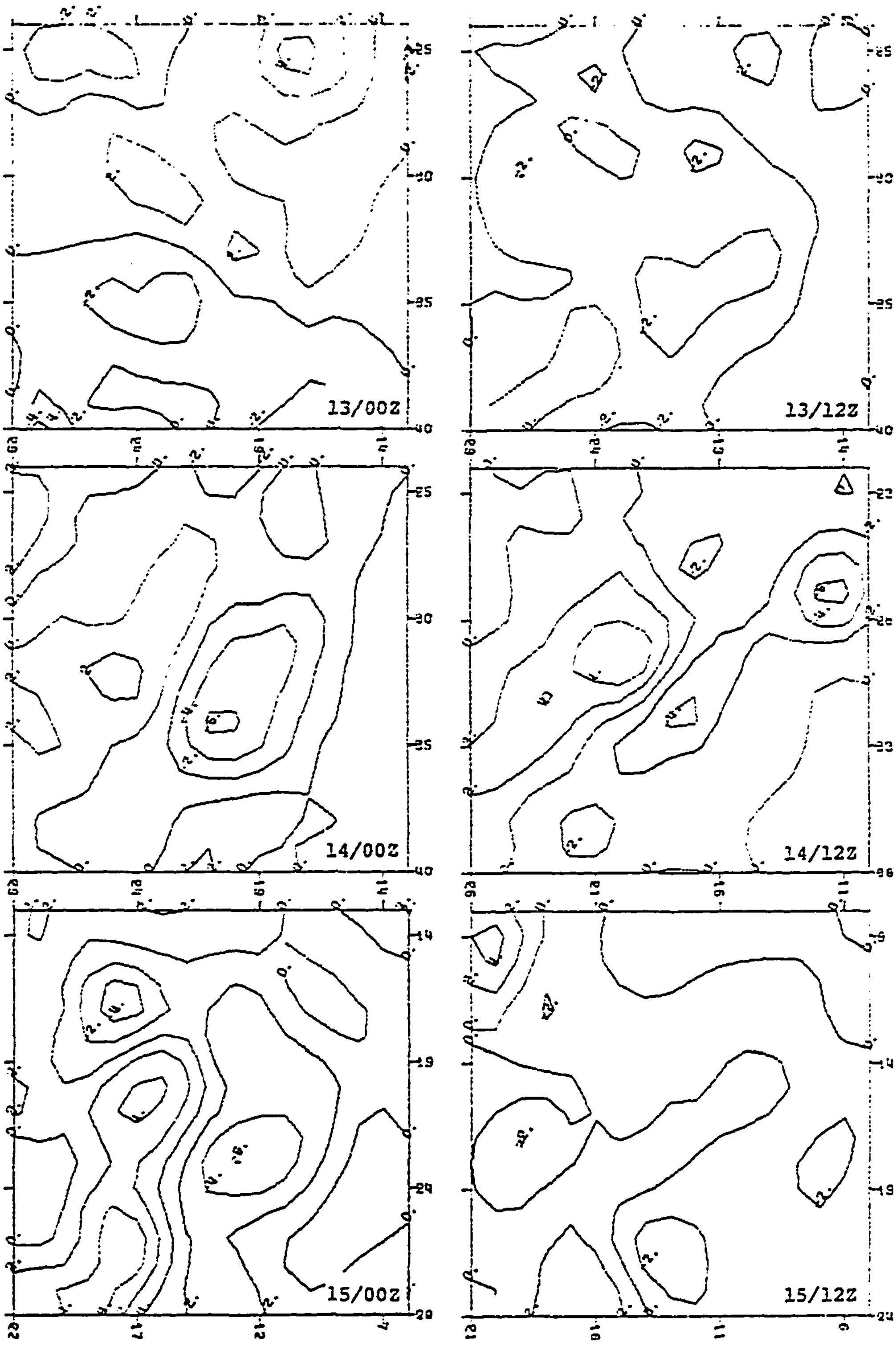

Fig. 16. The analyses of 500 mb vertical motion ($x10^{-3}$ mb sec^{-1}) within the storm volumes.

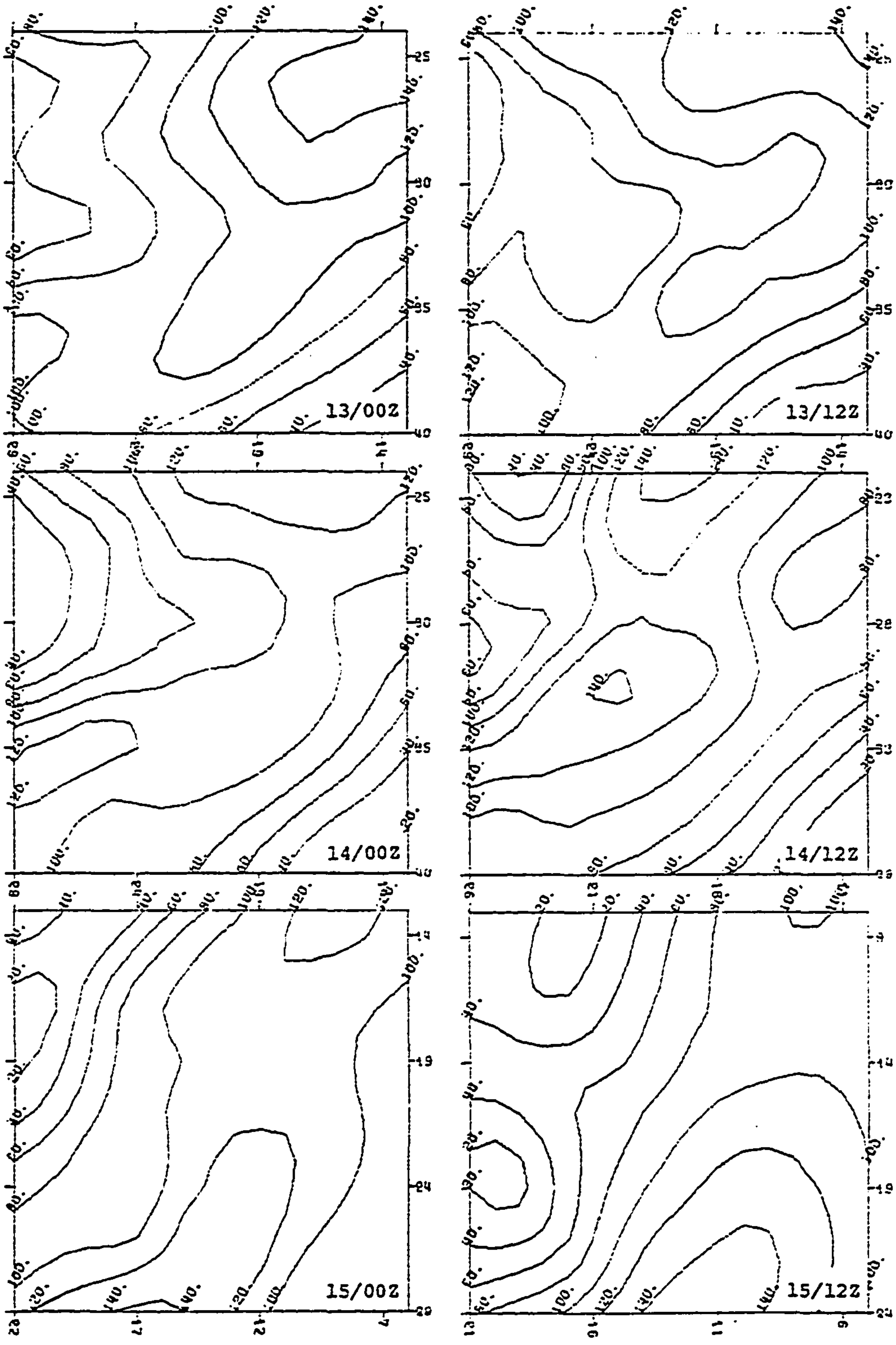

Fig. 17. The isotachs at 300 mb (knots) within the storm volumes.

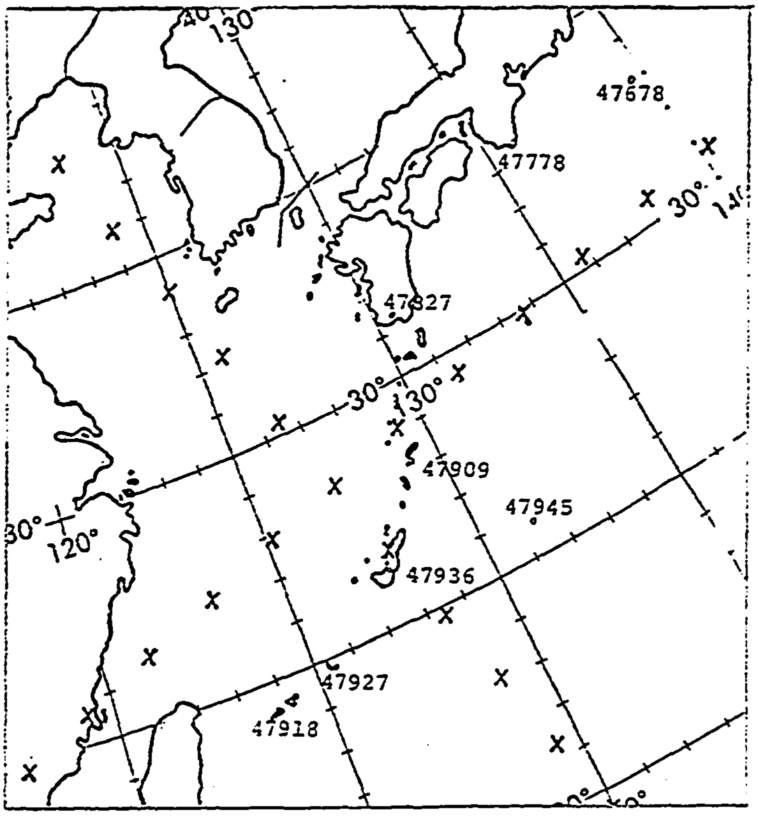

Fig. 18. The locations of the eight stations used in the comparison of the observed and estimated precipitation rates.

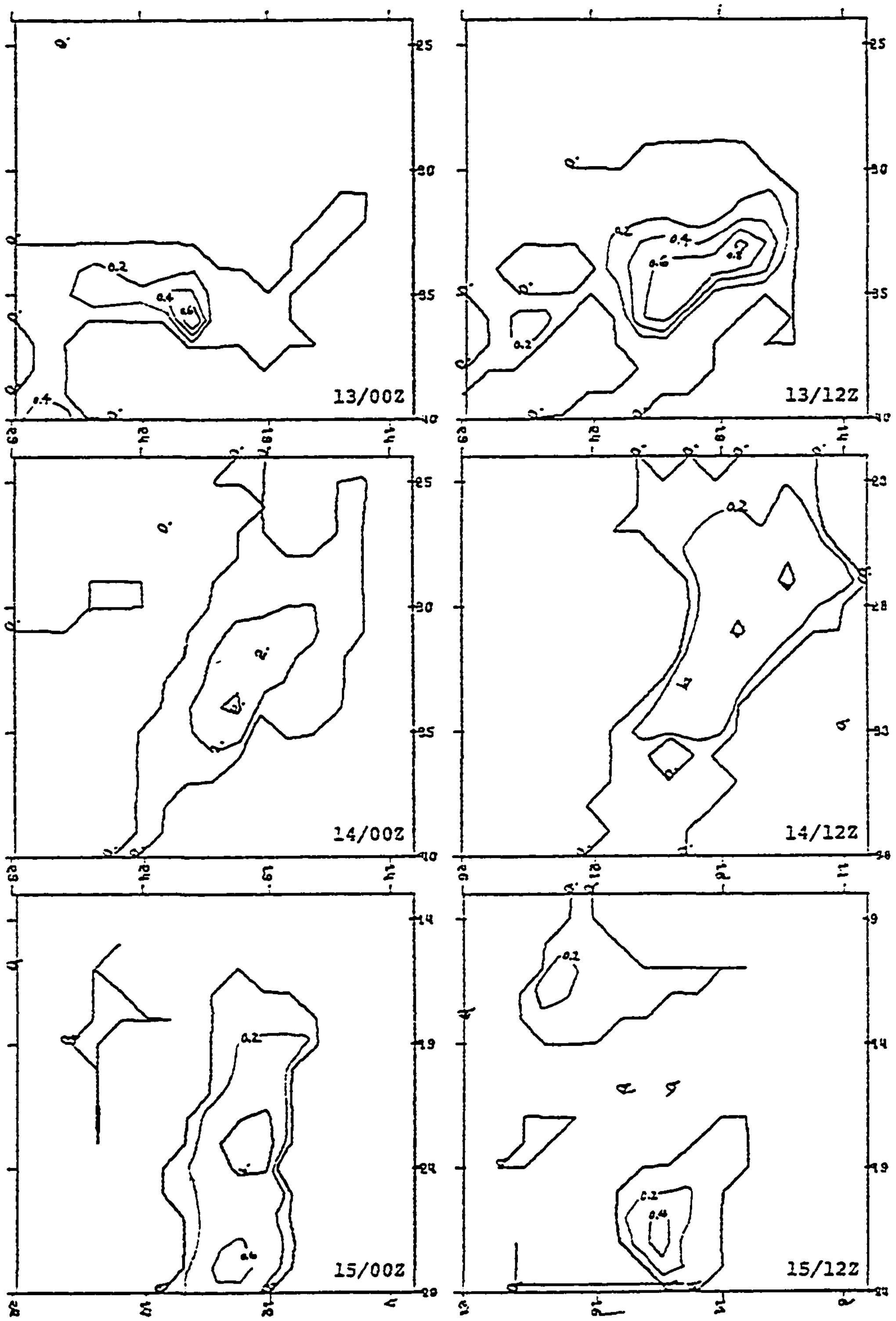

Fig. 19. The estimated precipitation rates (mm hr^{-1}) due to large scale lifting within the storm volumes.

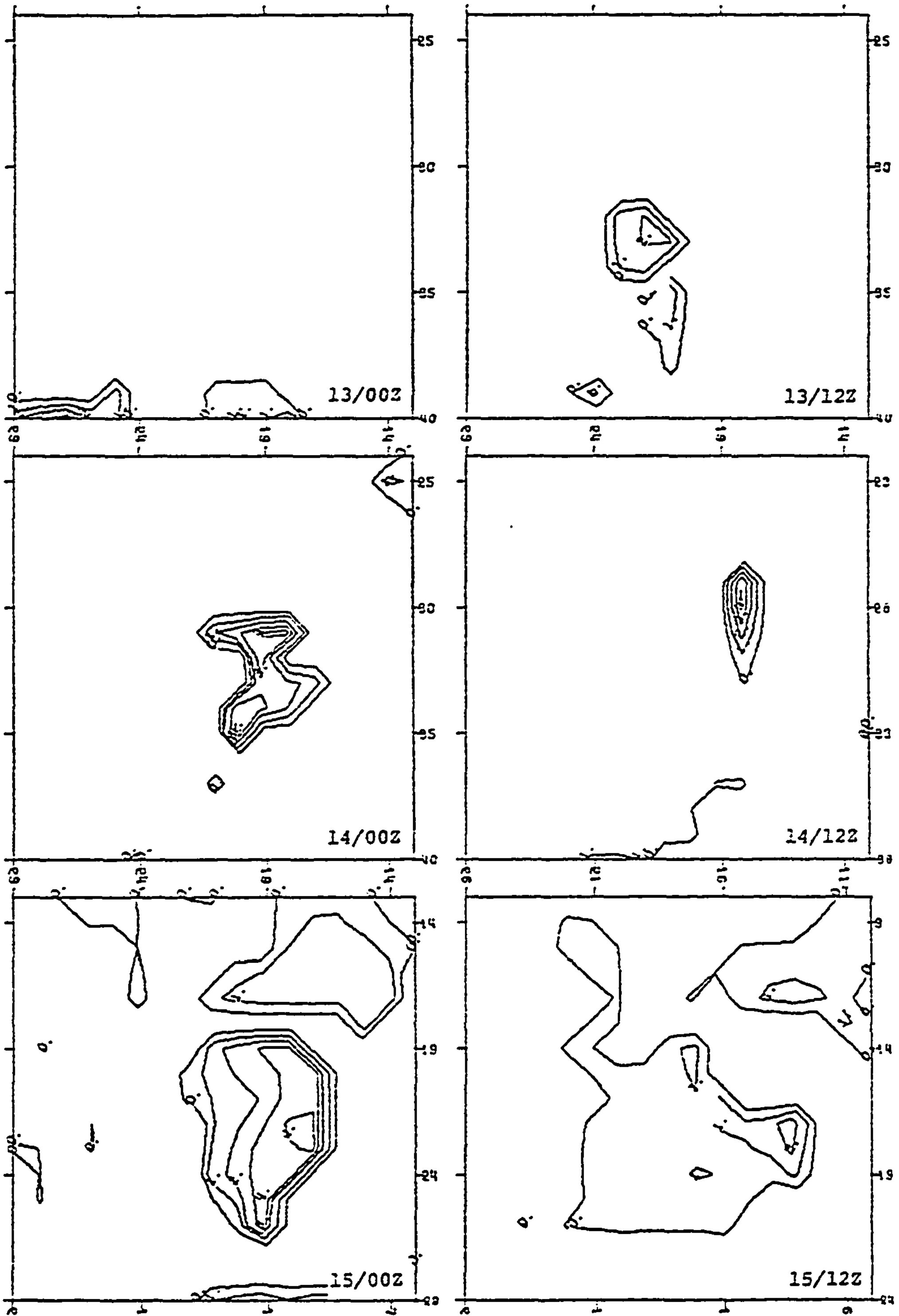

Fig. 20. The estimated precipitation rates (mm hr^{-1}) due to convective activity within the storm volumes.

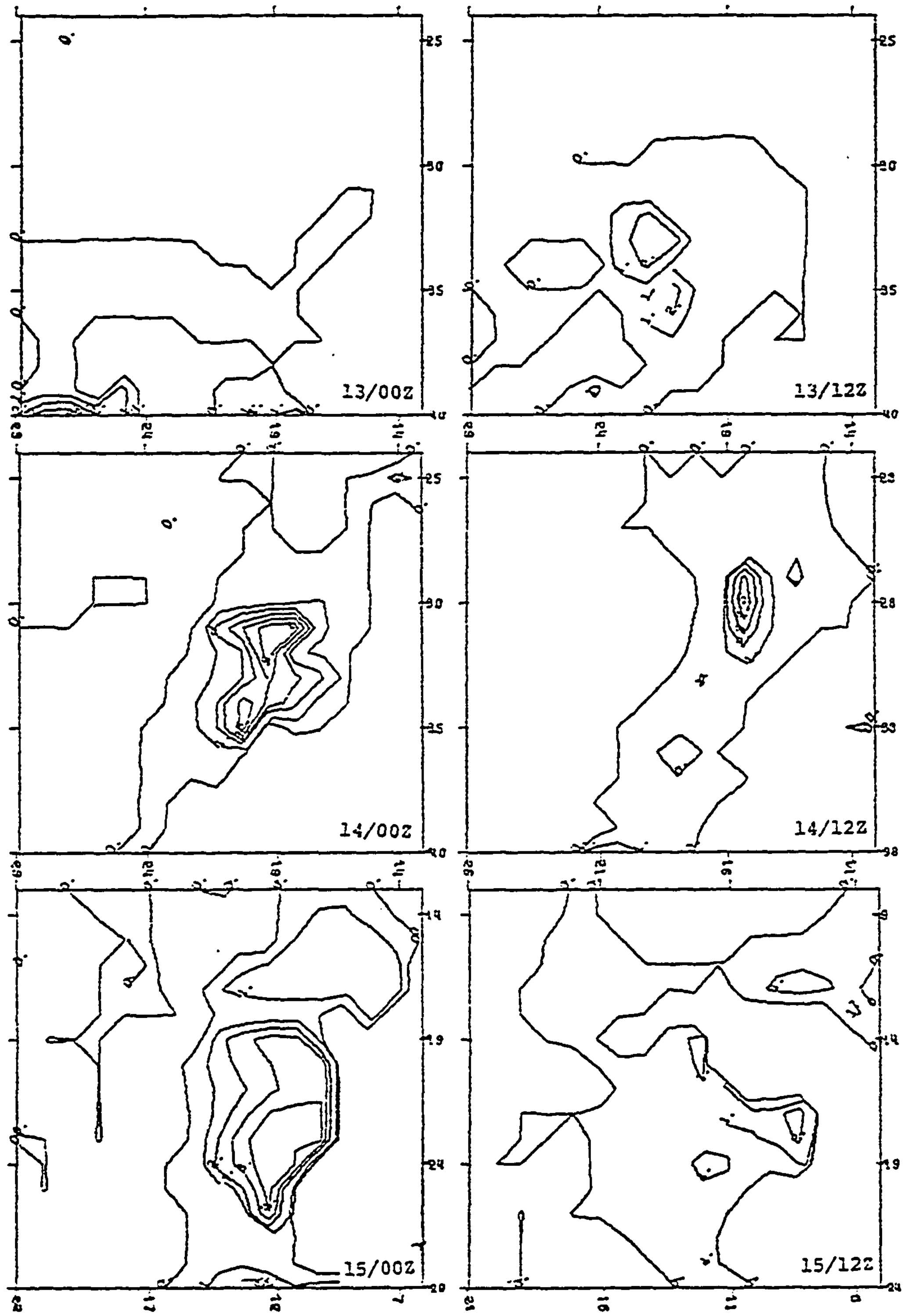

Fig. 21. The estimated total precipitation rates (mm hr^{-1}) within the storm volumes.

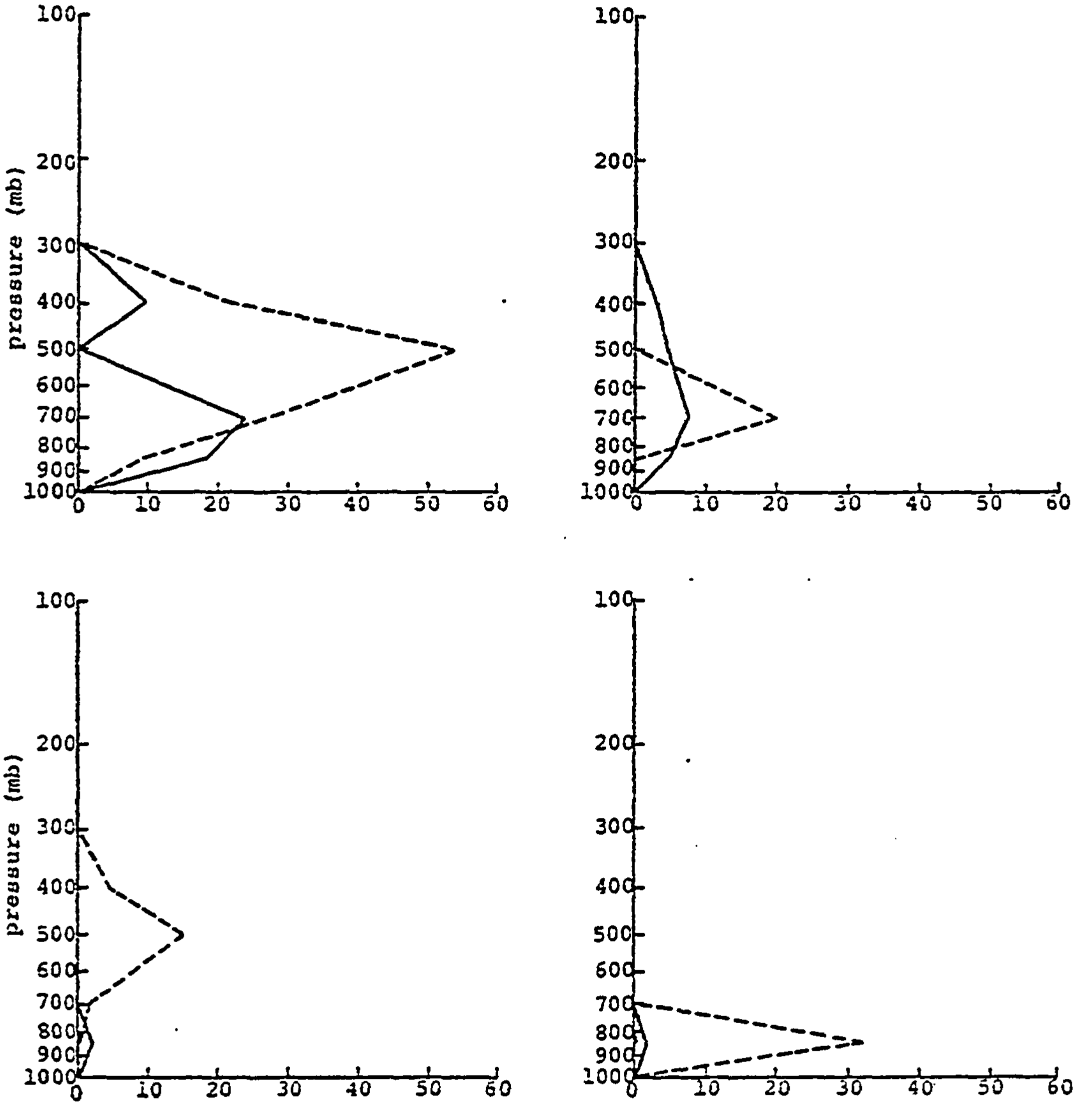

Fig. 22. Examples of the vertical profiles of stable (solid line) and convective (dashed line) latent heat release (K day^{-1}).

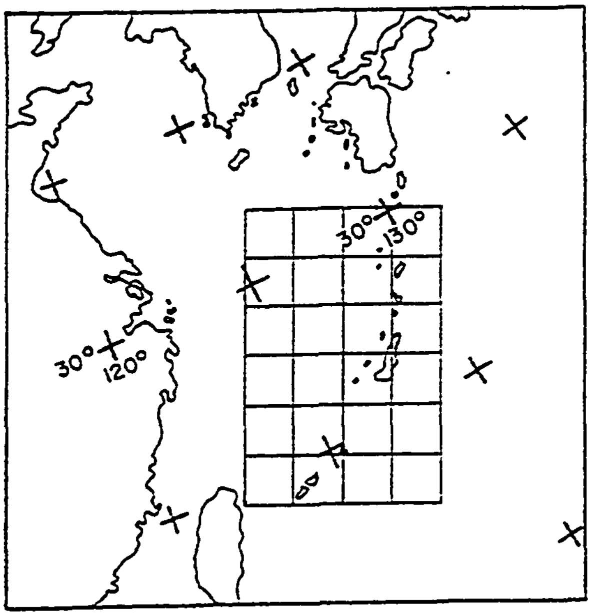

Fig. 23. The 5 x 7 grid mesh used in the comparison of sensible and latent heat fluxes with other estimates made over the AMTEX region.

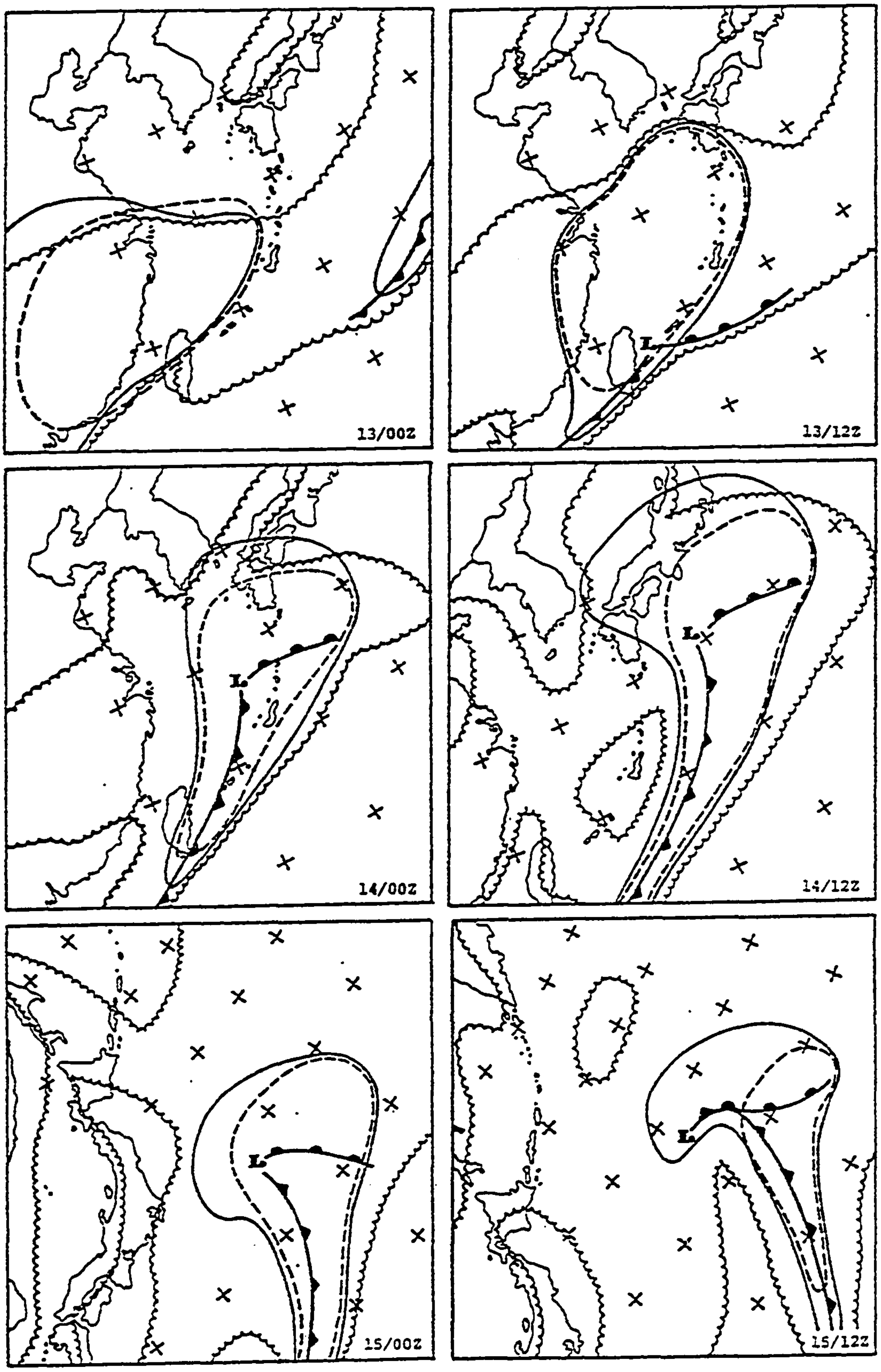

Fig. 24. Distributions of low (scalloped line), middle (solid line) and high (dashed line) clouds.

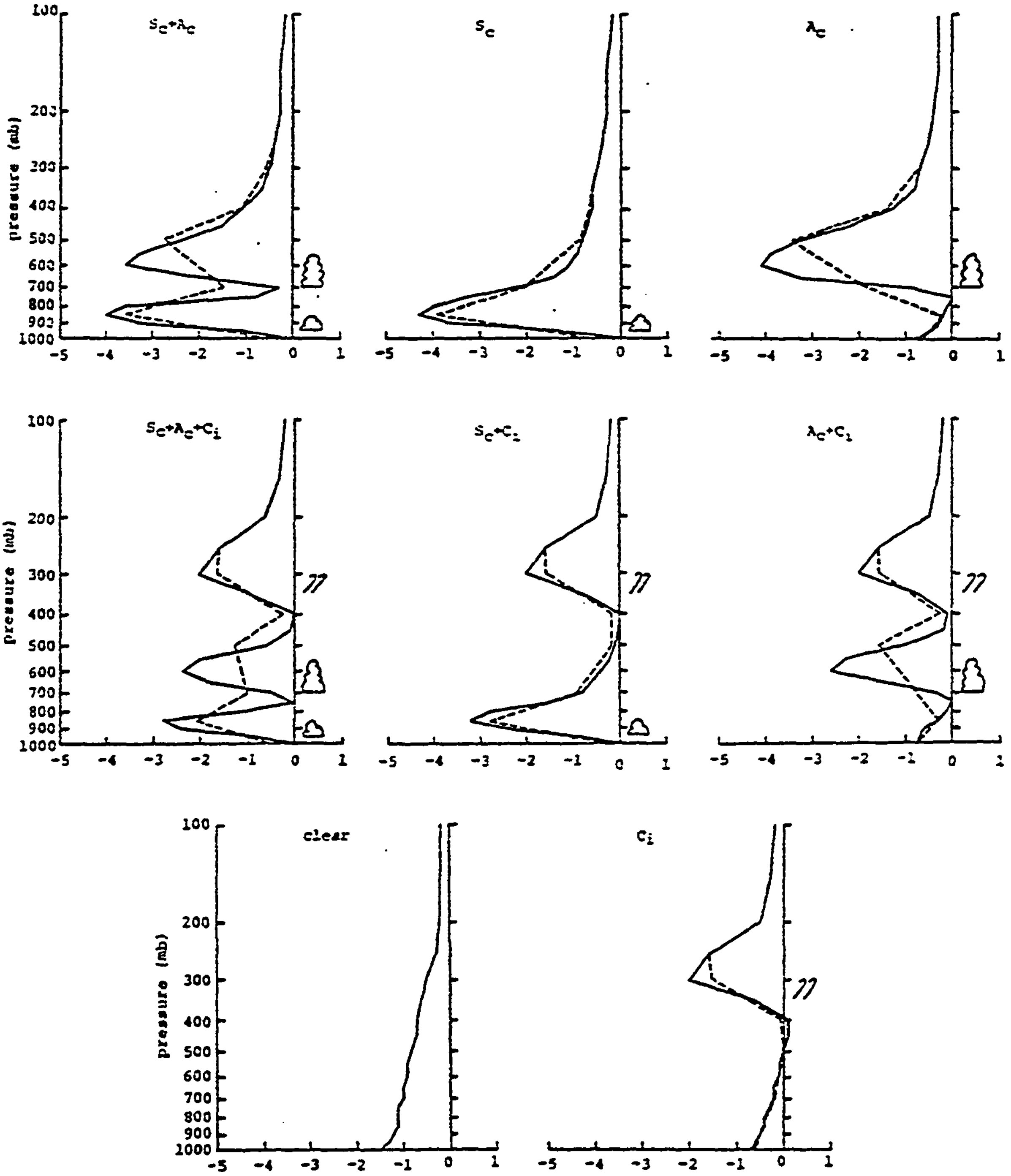

Fig. 25. The vertical profiles of the estimated radiational heating rates (K day^{-1}) for eight different cloud combinations. The solid lines are at 50 mb intervals and the dashed lines are at the standard levels used in this study.

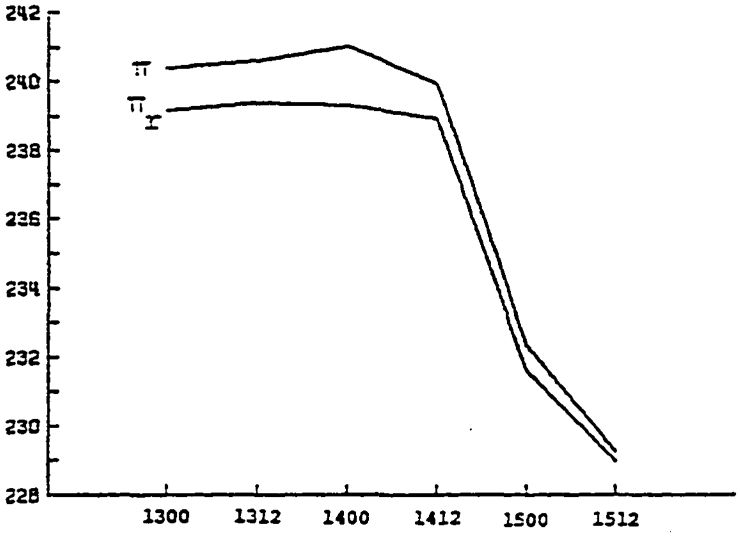

Fig. 26. The amount of the TPE ($x10^7$ J m^{-2}) of the atmosphere within the storm volumes and their respective reference states as a function of time.

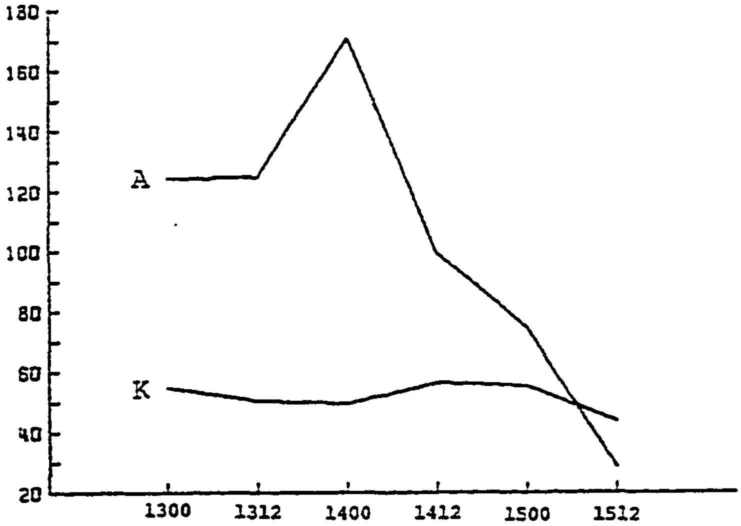

Fig. 27. The amount of APE and KE ($x10^5$ J m^{-2}) of the atmosphere within the storm volumes as a function of time.

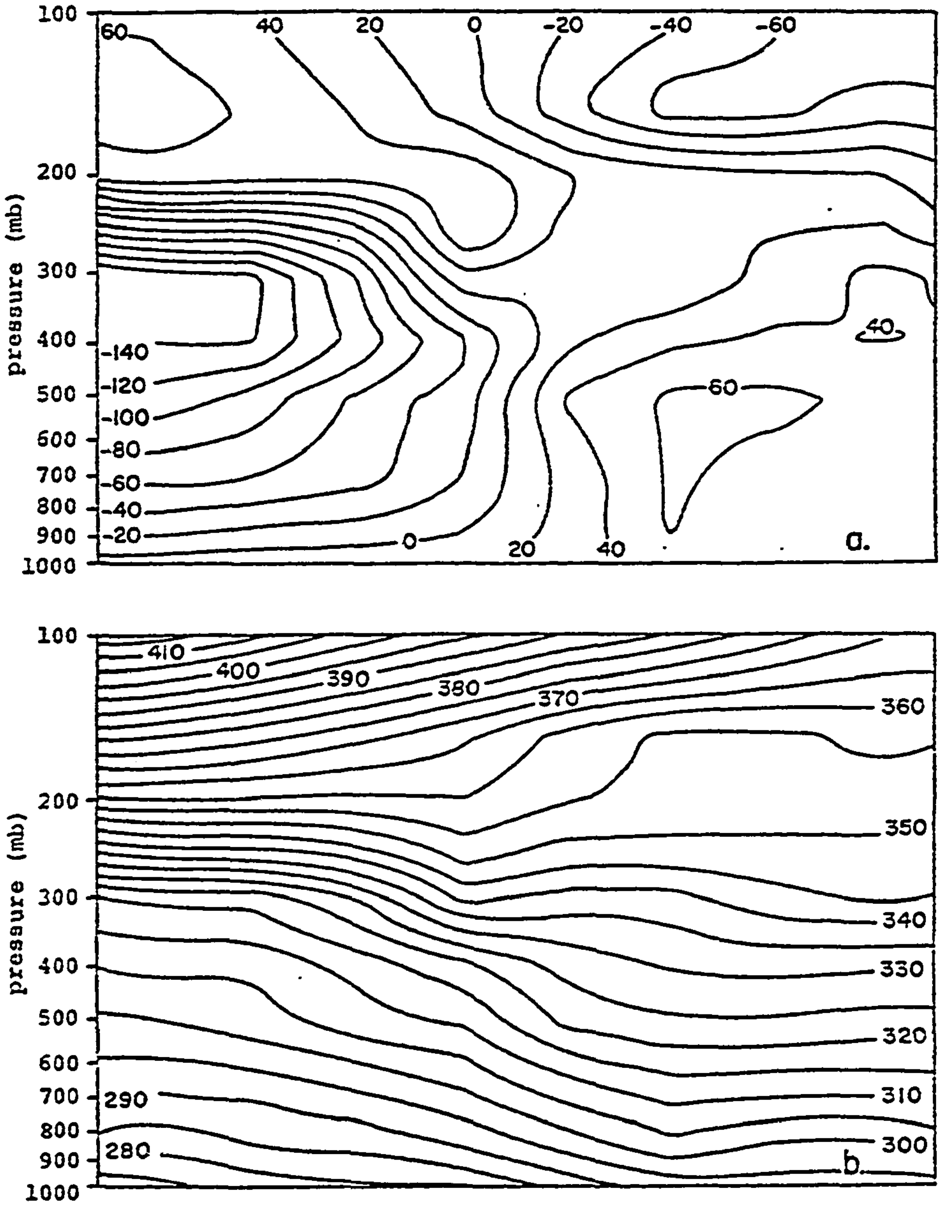

Fig. 28. Figs. a and b depicts respectively the distributions of the efficiency factor (x10^{-3}) and potential temperature (K) along a cross-section oriented approximately northwest-southeast just to the southwest of the storm center at 1200 GMT 14 February.

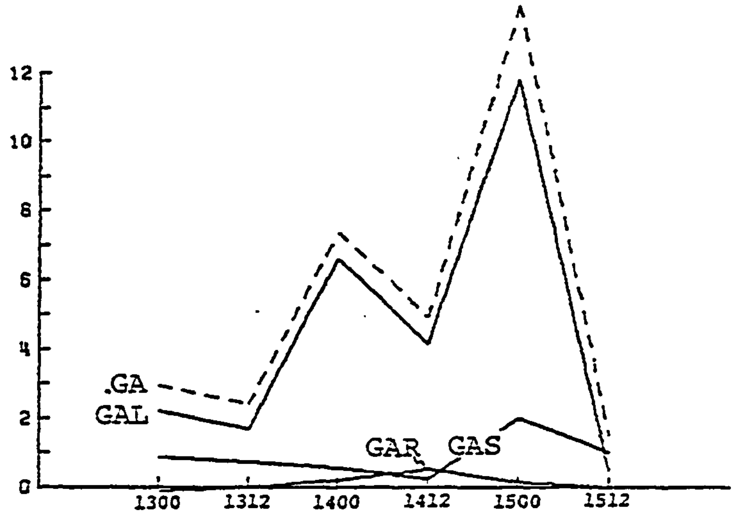

Fig. 29. The total generation of APE (GA) and the contributions from latent heat release (GAL), sensible heat addition (GAS) and radiational heating (GAR) in W m^{-2}.

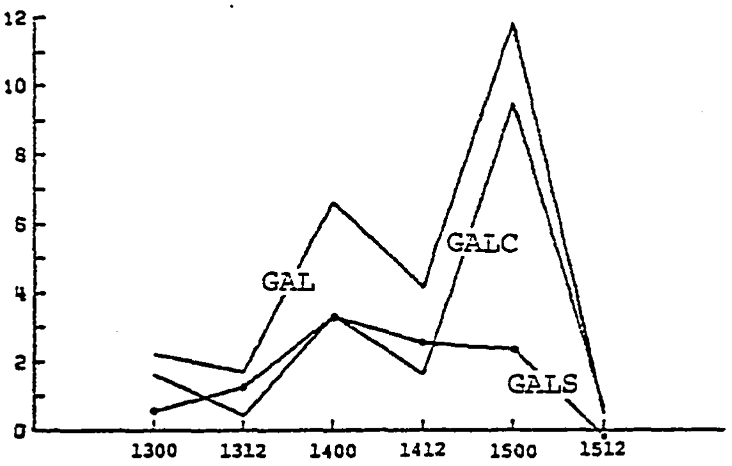

Fig. 30. The generation of APE due to stable (GALS) and convective (GALC) latent heat release and the sum of the two (GAL) in W m^{-2}.

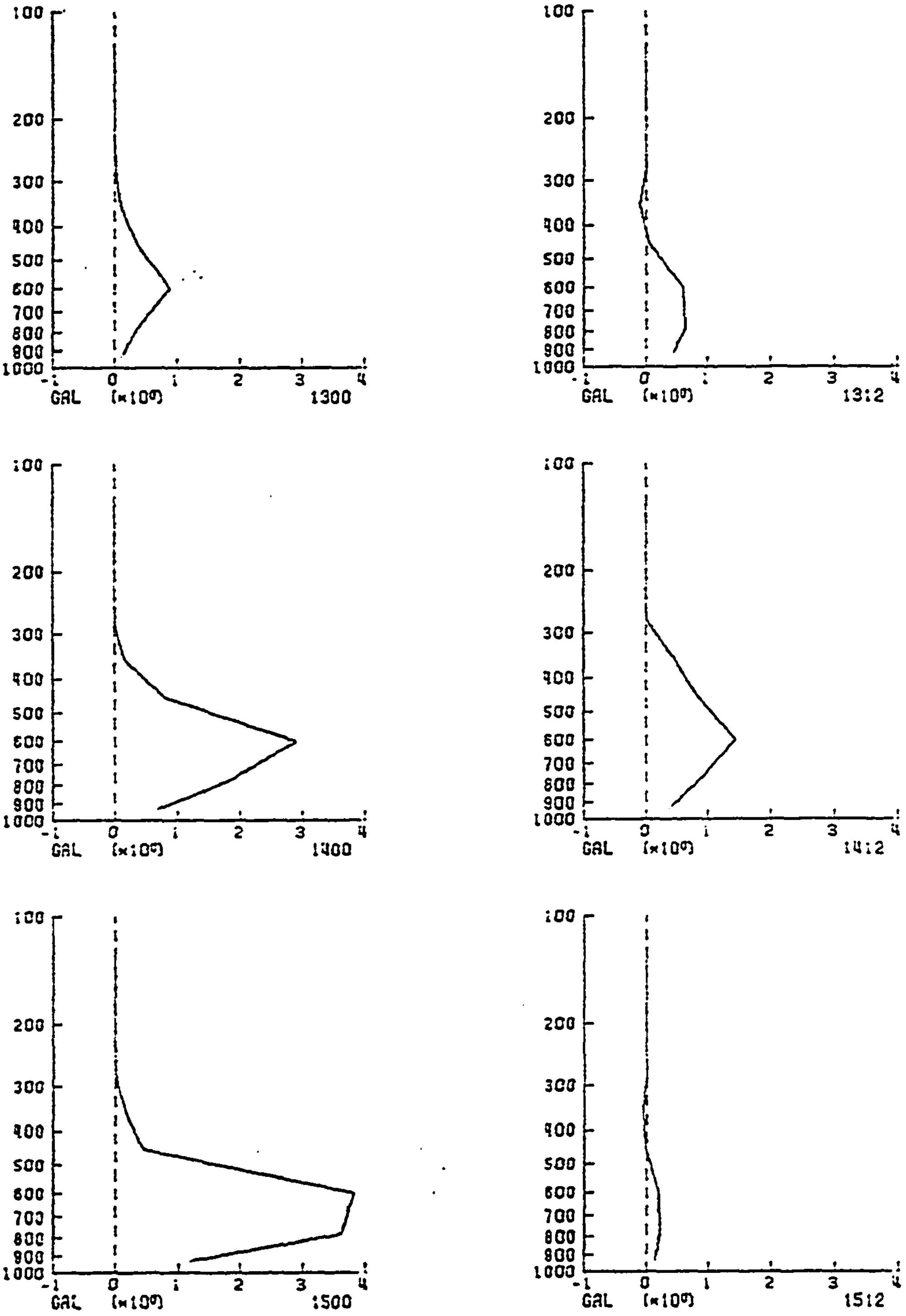

Fig. 31. Vertical profiles of the generation of APE by latent heat release (GAL) in W m^{-2}.

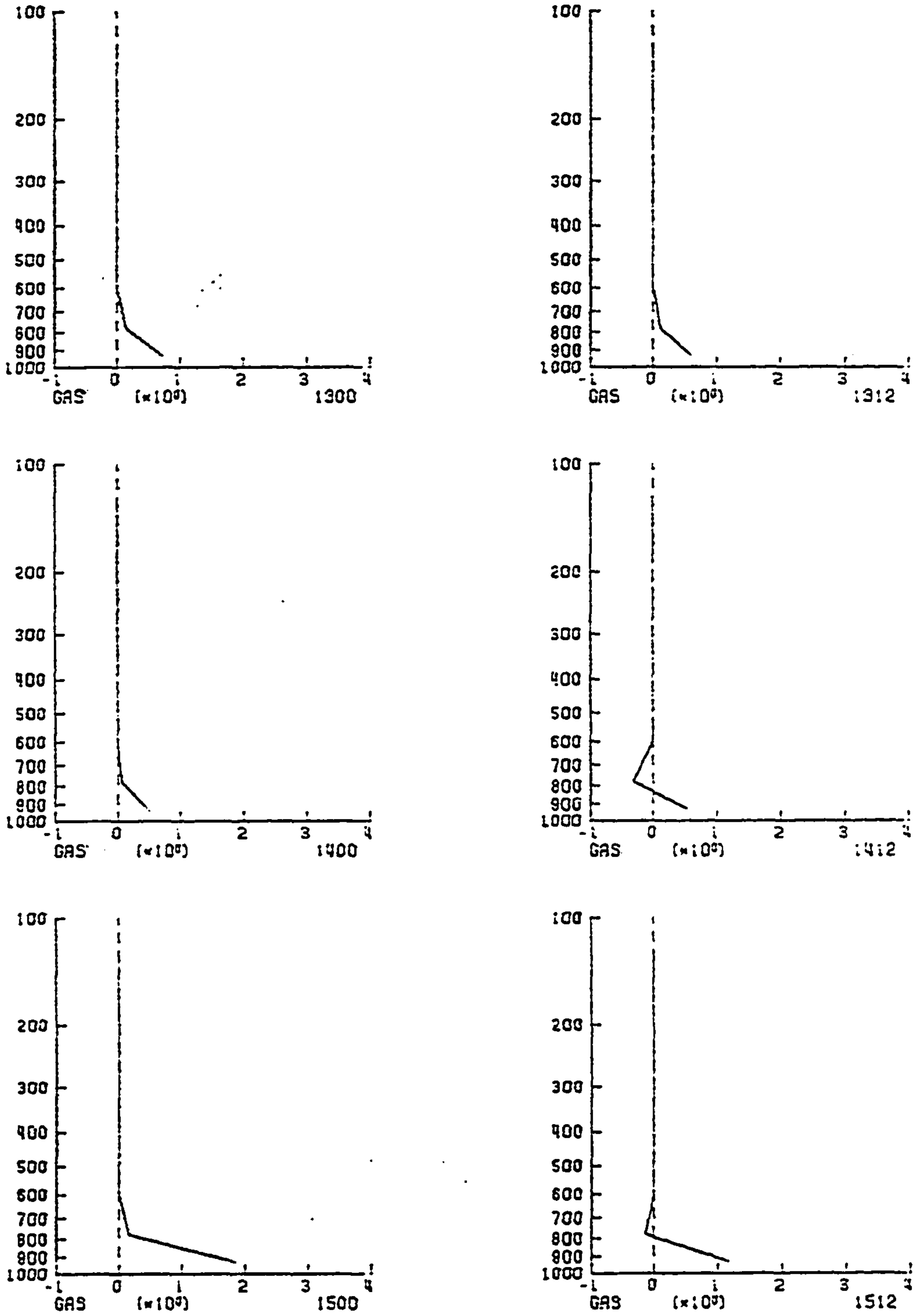

Fig. 32. Vertical profiles of the generation of APE by sensible heat addition (GAS) in W m^{-2}.

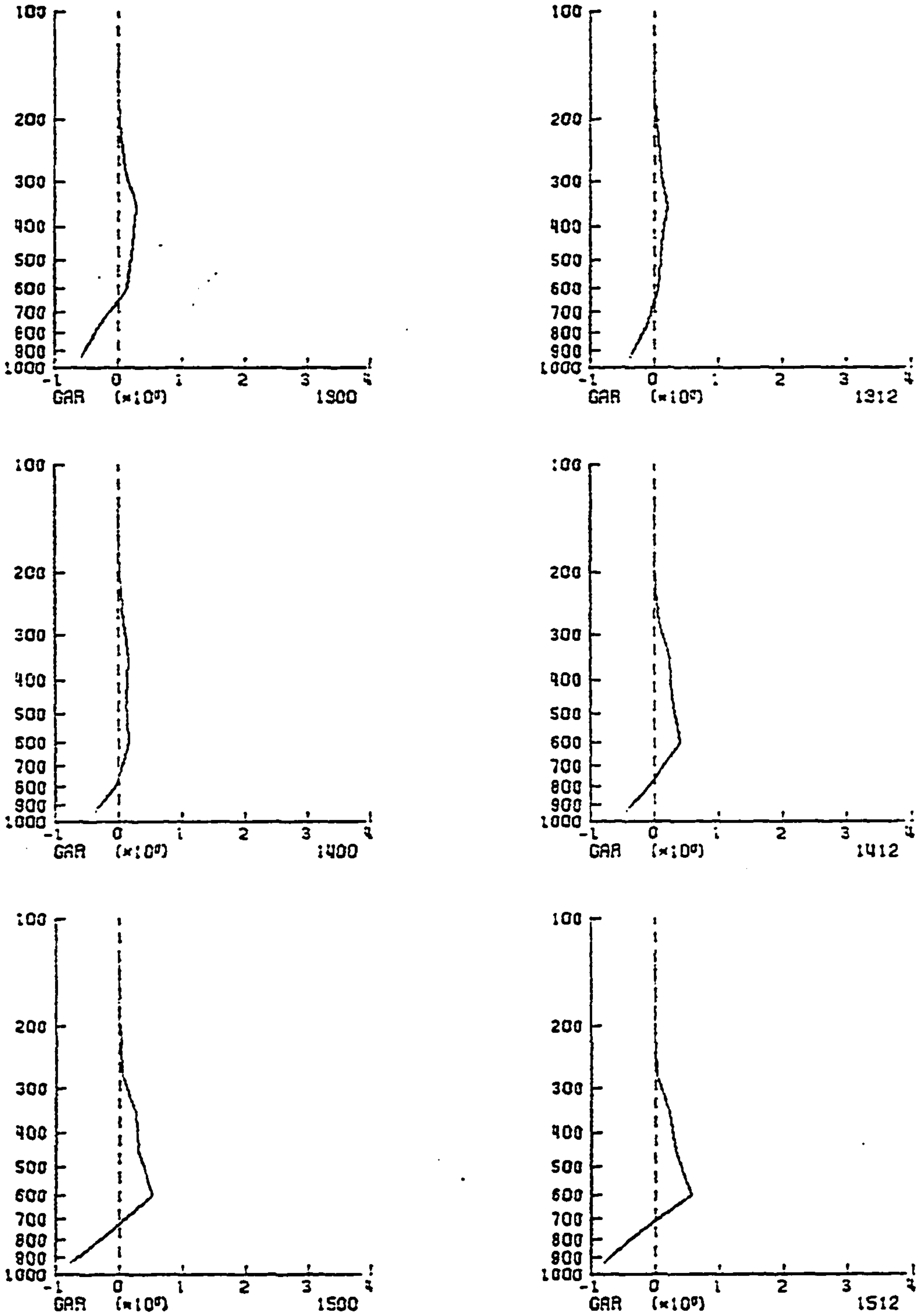

Fig. 33. Vertical profiles of the generation of APE by radiational heating (GAR) in W m^{-2}.

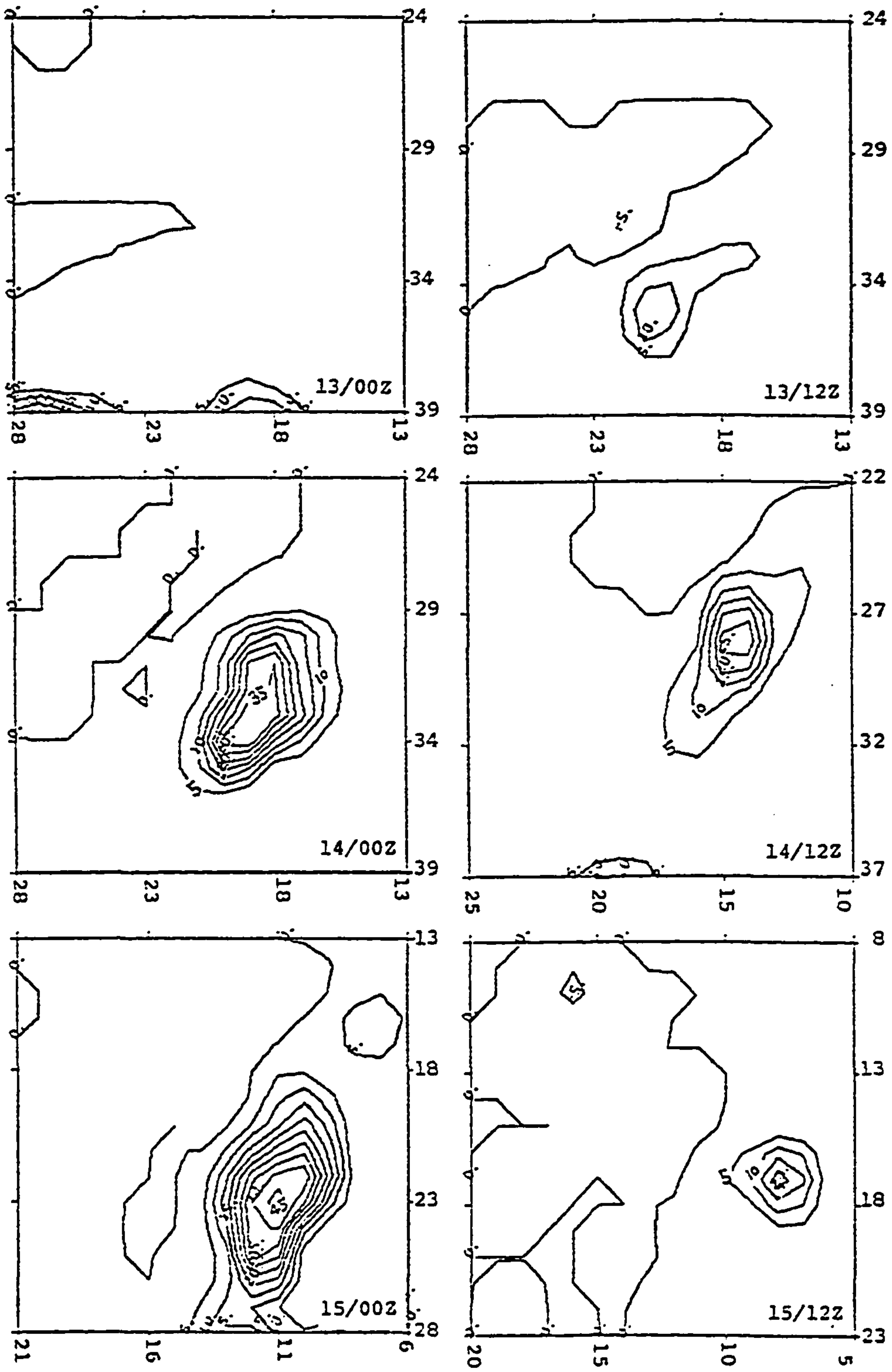

Fig. 34. Horizontal distributions of the generation of APE by latent heat release (GAL) in 10^{-2} W m^{-2}.

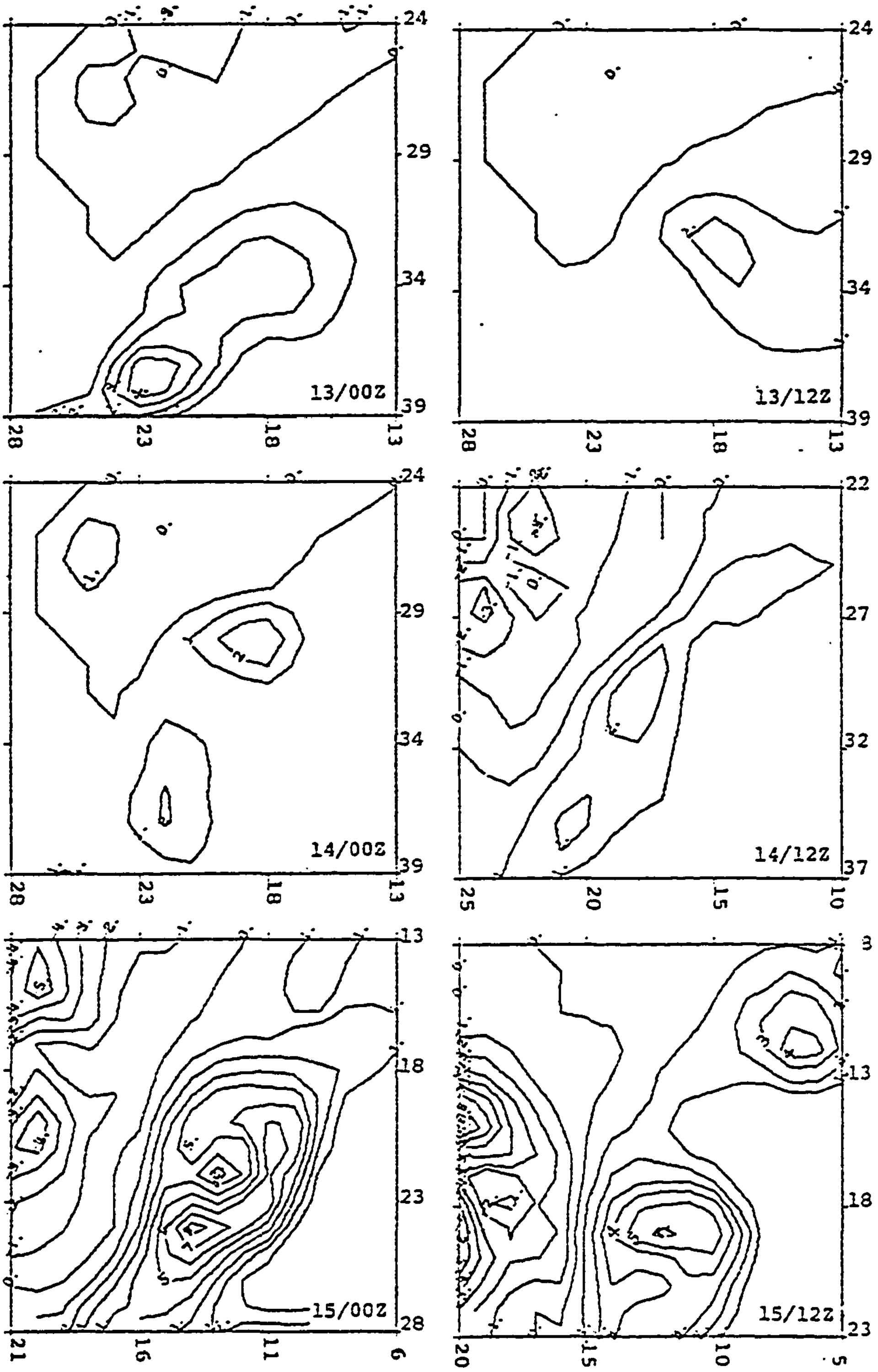

Fig. 35. Horizontal distributions of the generation of APE by sensible heat addition (GAS) in 10^{-2} W m^{-2}.

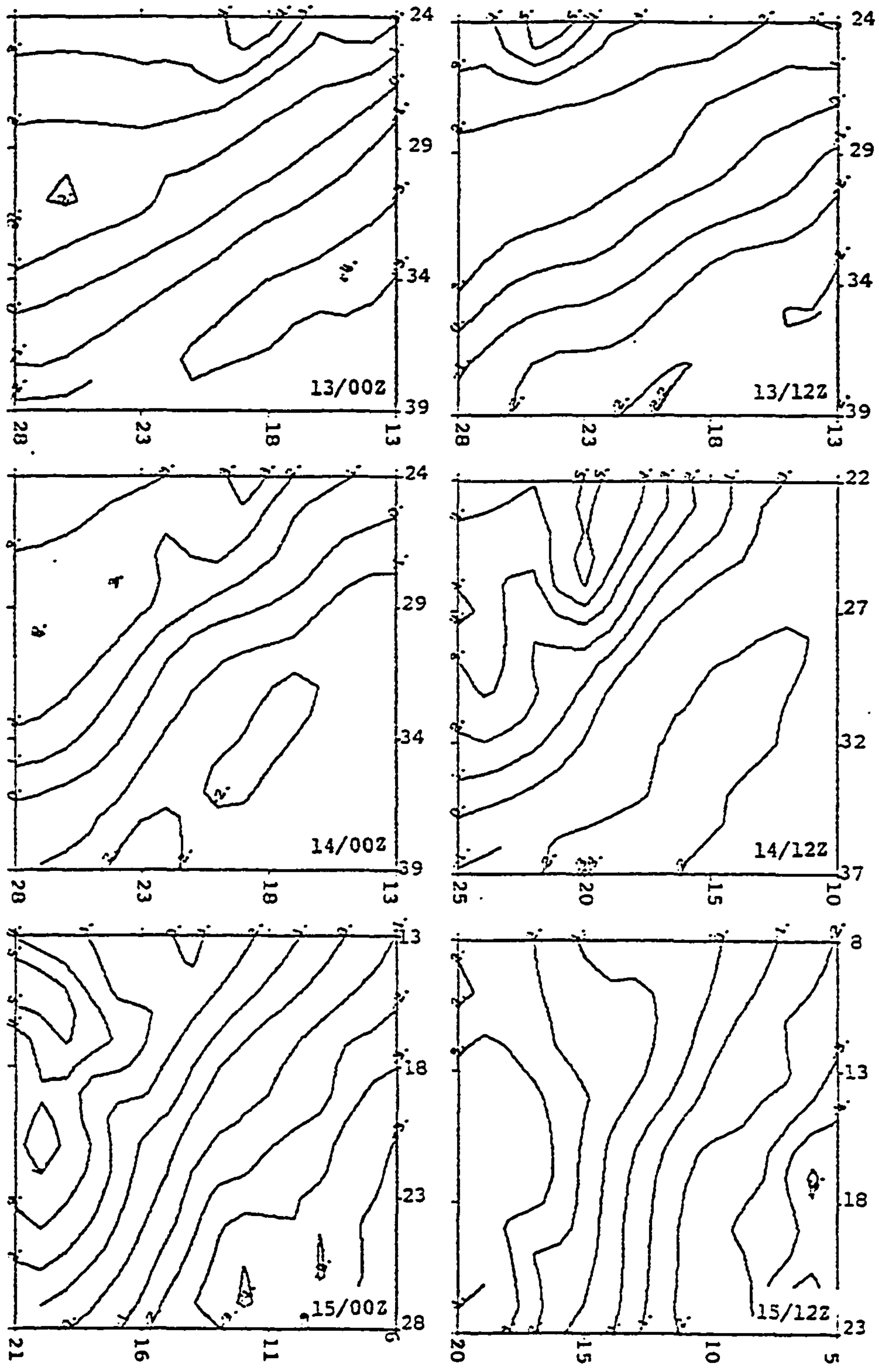

Fig. 36. Horizontal distributions of the generation of APE by radiational heating (GAR) in 10^{-2} W m^{-2}.

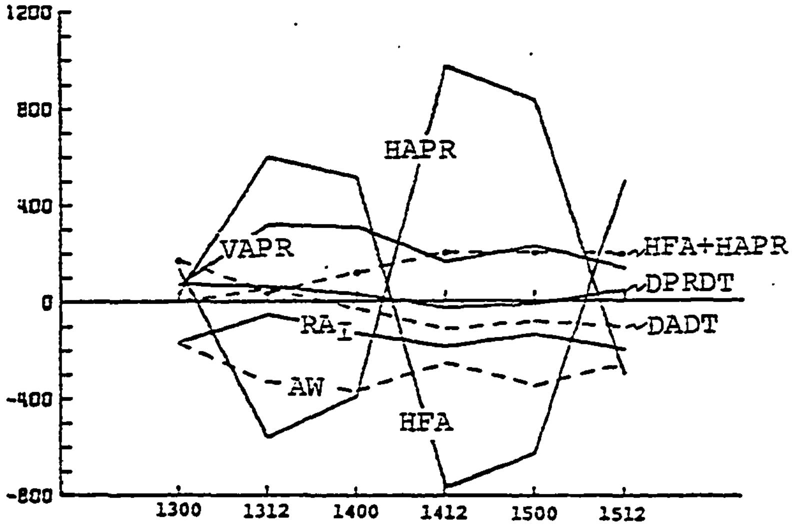

Fig. 37. The available potential energy budget I (W m^{-2}) of the AMTEX storm plotted as a function of time. DAREAA, DPSA, VFA and GA are not shown due to relatively small magnitude.

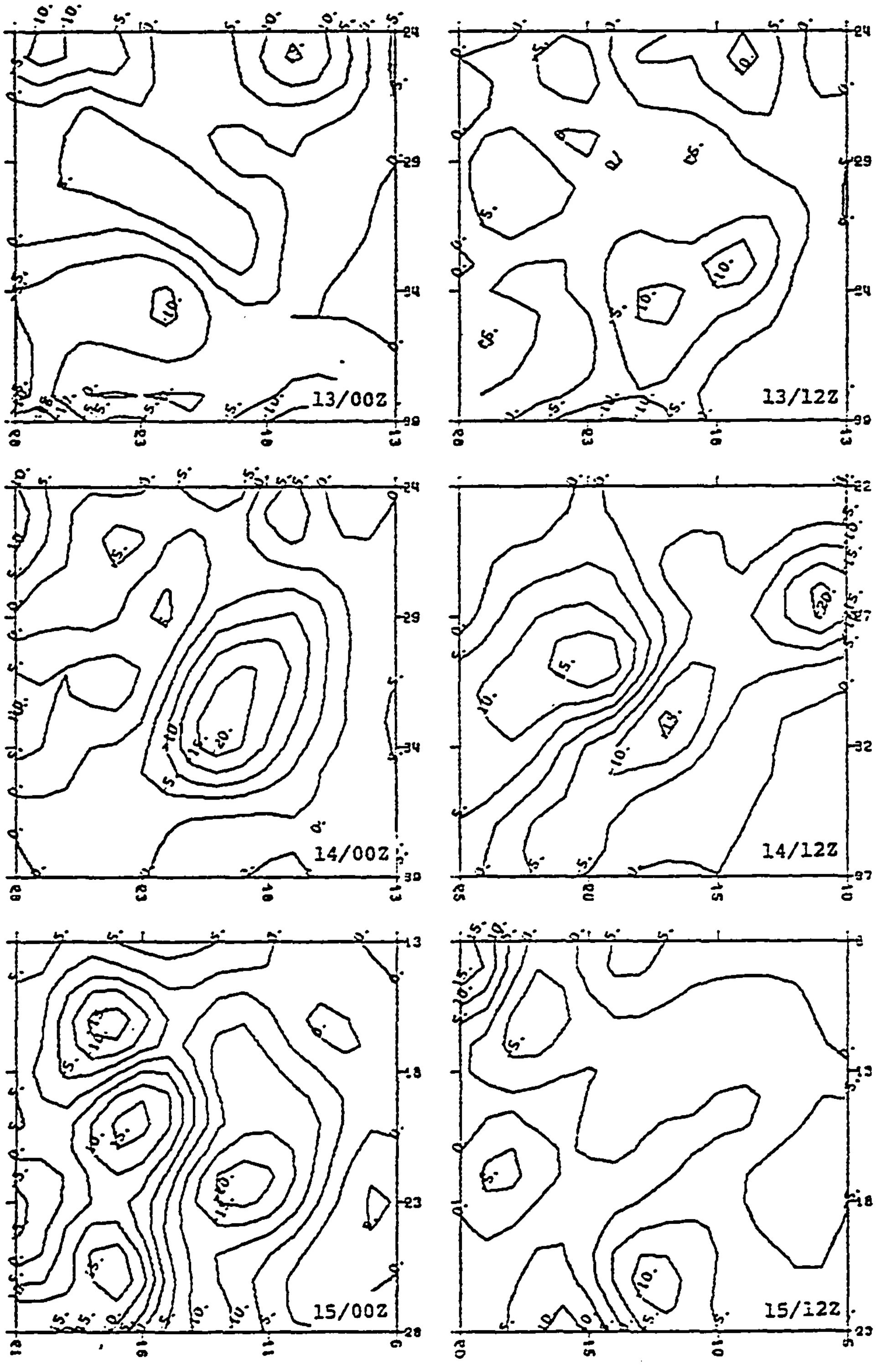

Fig. 38. Horizontal distributions of the vertically averaged AW in W m^{-2}.

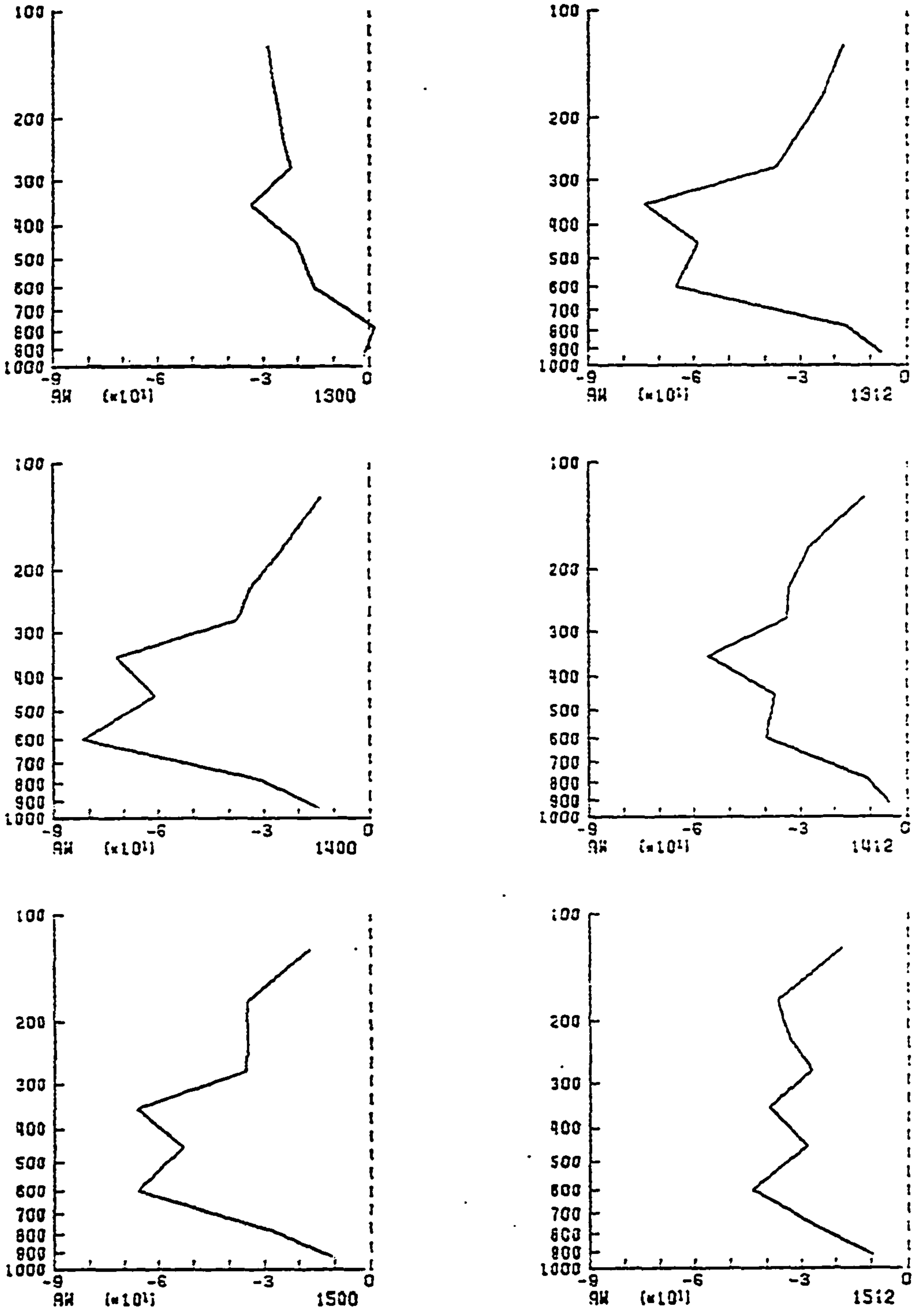

Fig. 39. Vertical profiles of the horizontally averaged AW in W m^{-2}.

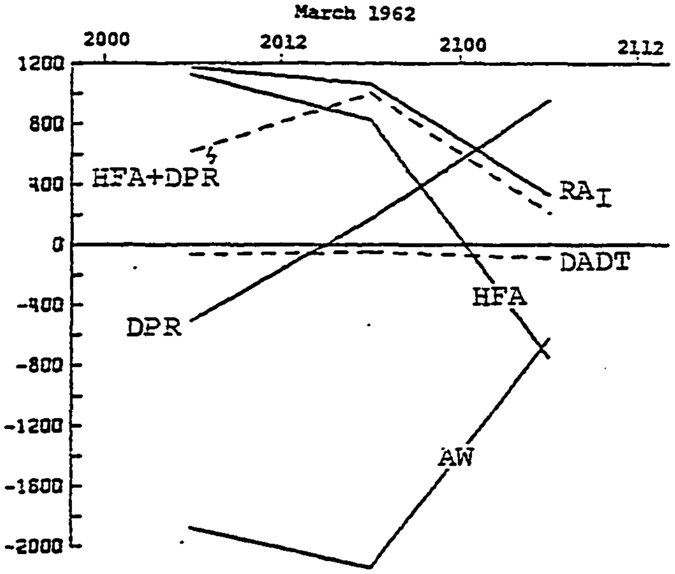

Fig. 40. The available potential energy budget I (W m^{-2}) evaluated by Pant (1976) for the developing, mature and occluded stages of a continental U.S. cyclone.

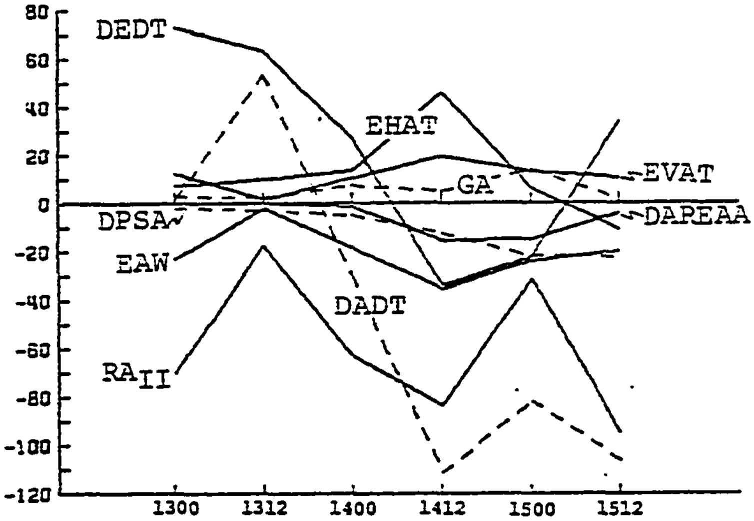

Fig. 41. The available potential energy budget II (W m^{-2}) of the AMTEX storm plotted as a function of time.

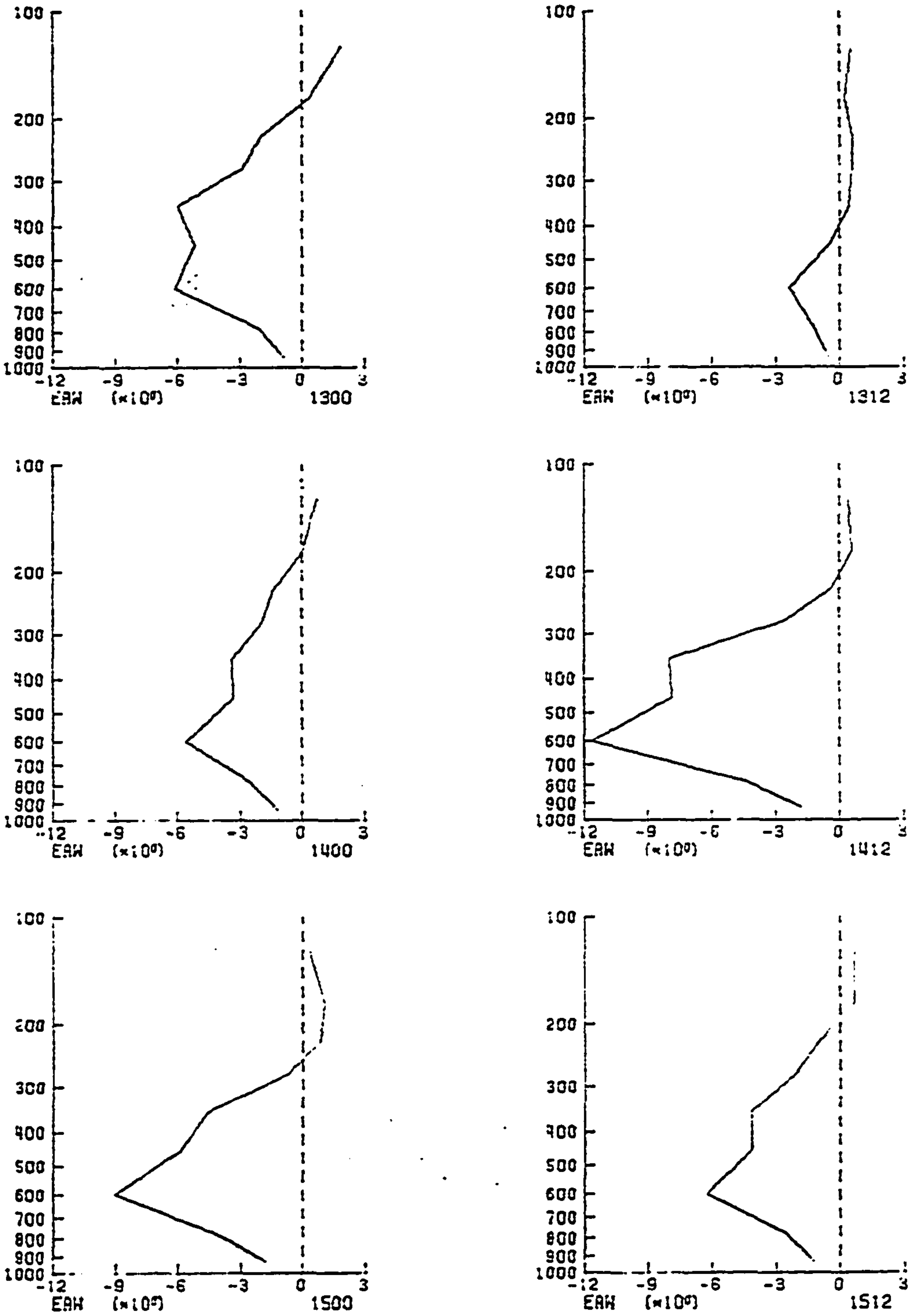

Fig. 42. Vertical profiles of horizontally averaged EAW in W m^{-2}.

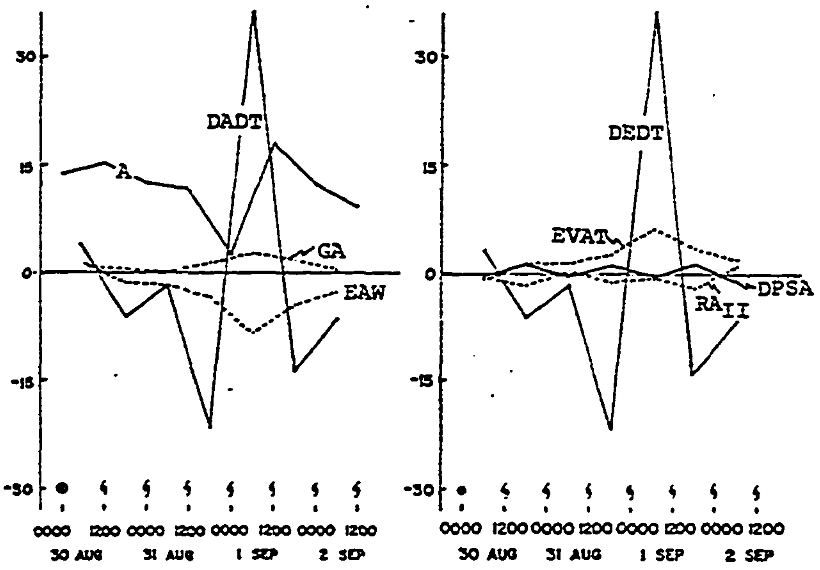

Fig. 43. The available potential energy budget II of hurricane Carmen evaluated by Edmon and Vincent (1977). A is in 10^5 Jm^{-2}, and all others in W m^{-2}.

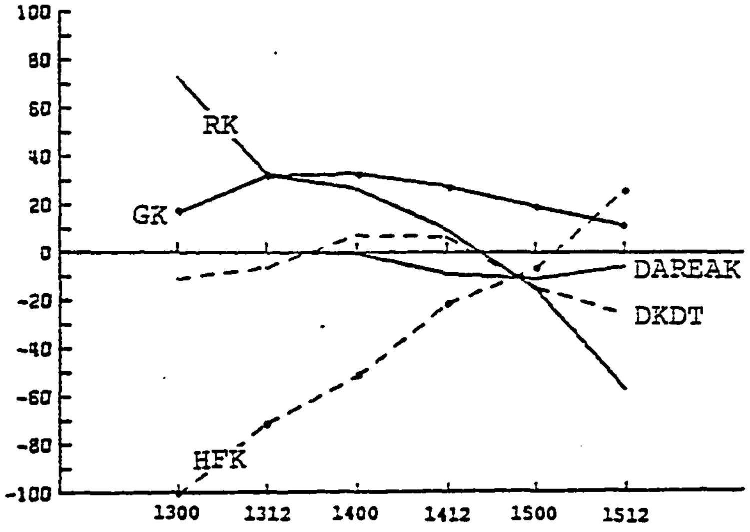

Fig. 44. The kinetic energy budget (W m^{-2}) of the AMTEX storm plotted as a function of time. VFK and DPSK are not shown due to relatively small magnitude.

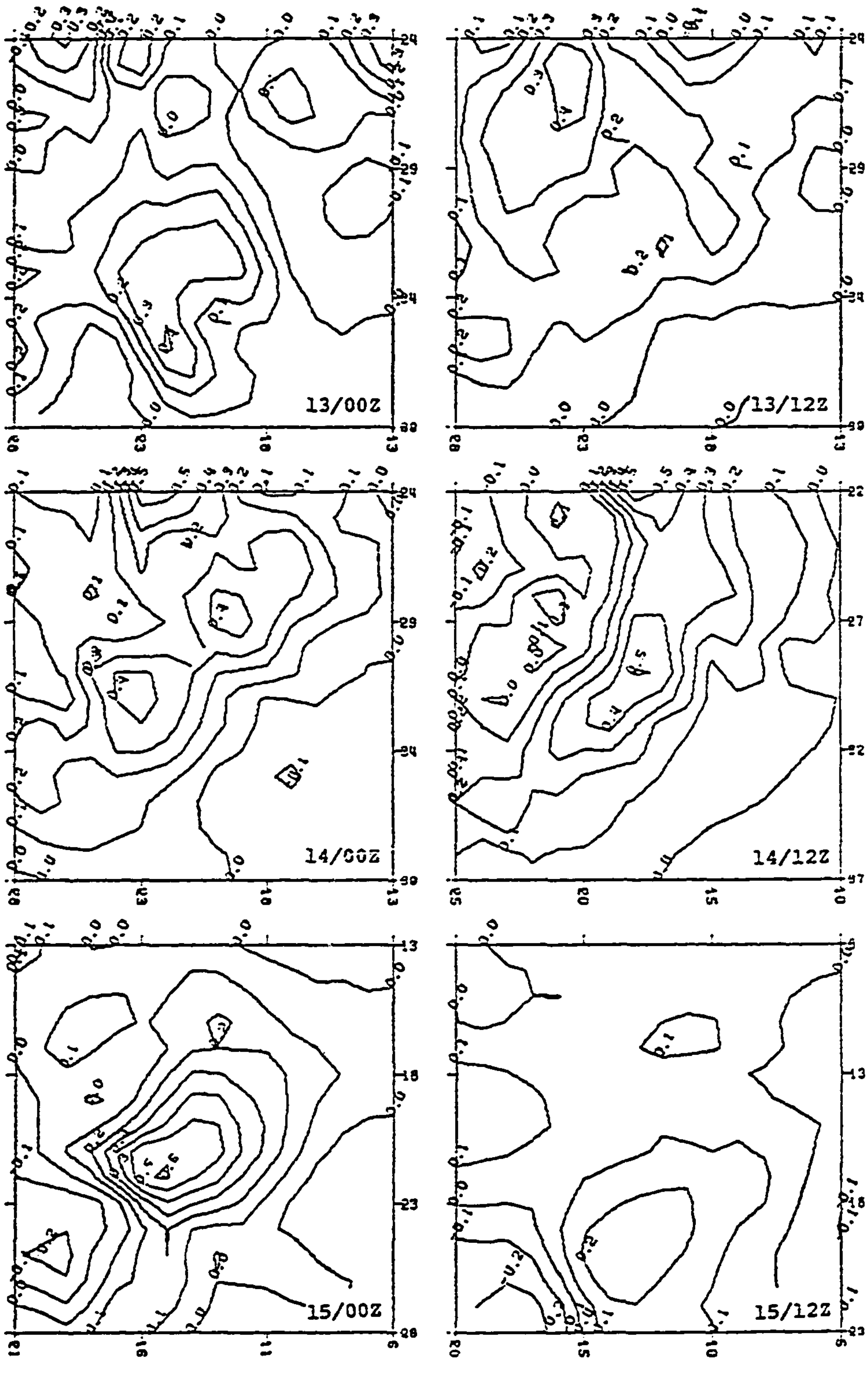

Fig. 45. Horizontal distributions of the vertically averaged GK in W m^{-2}.

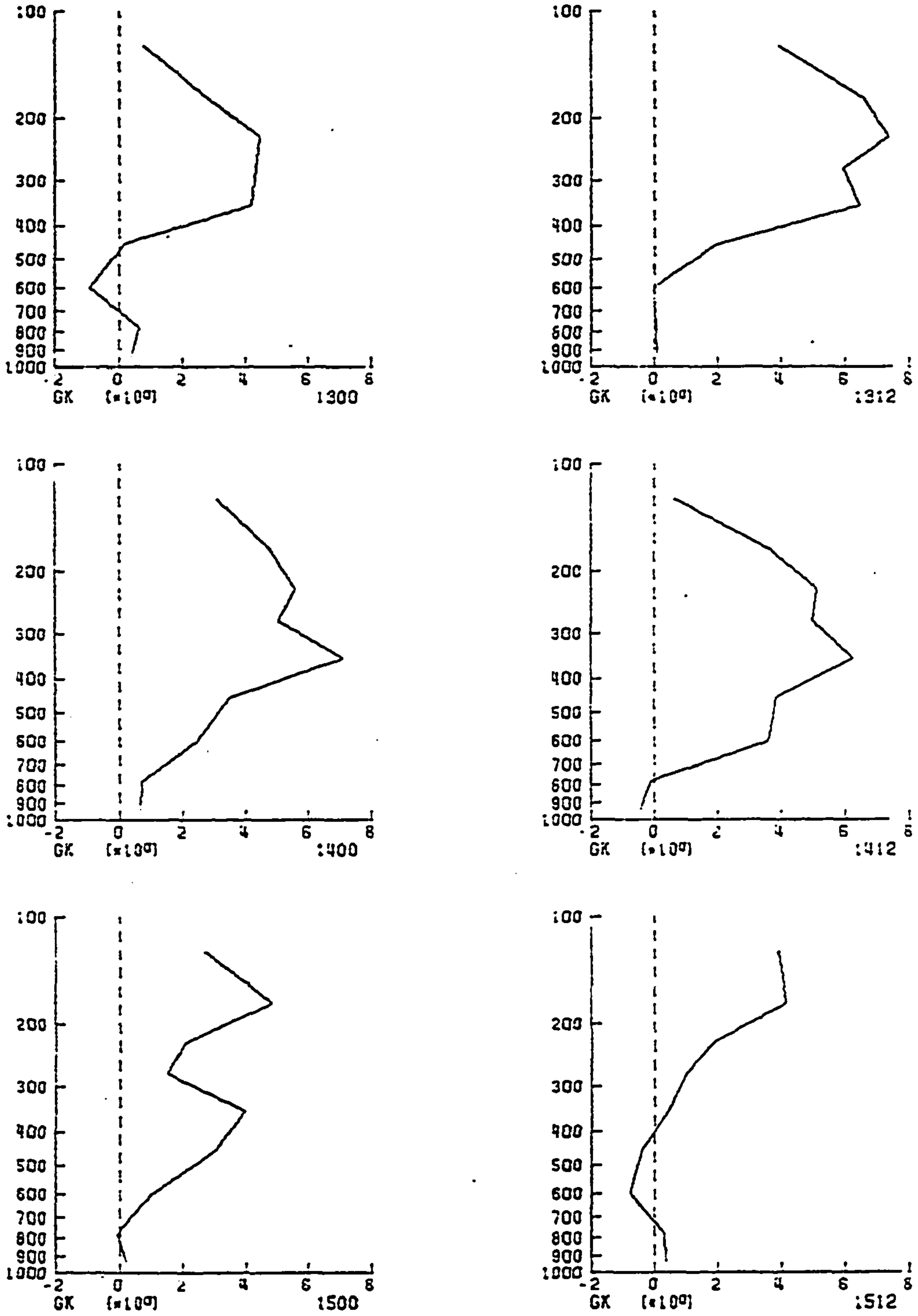

Fig. 46. Vertical profiles of the horizontally averaged GK in W m^{-2}.

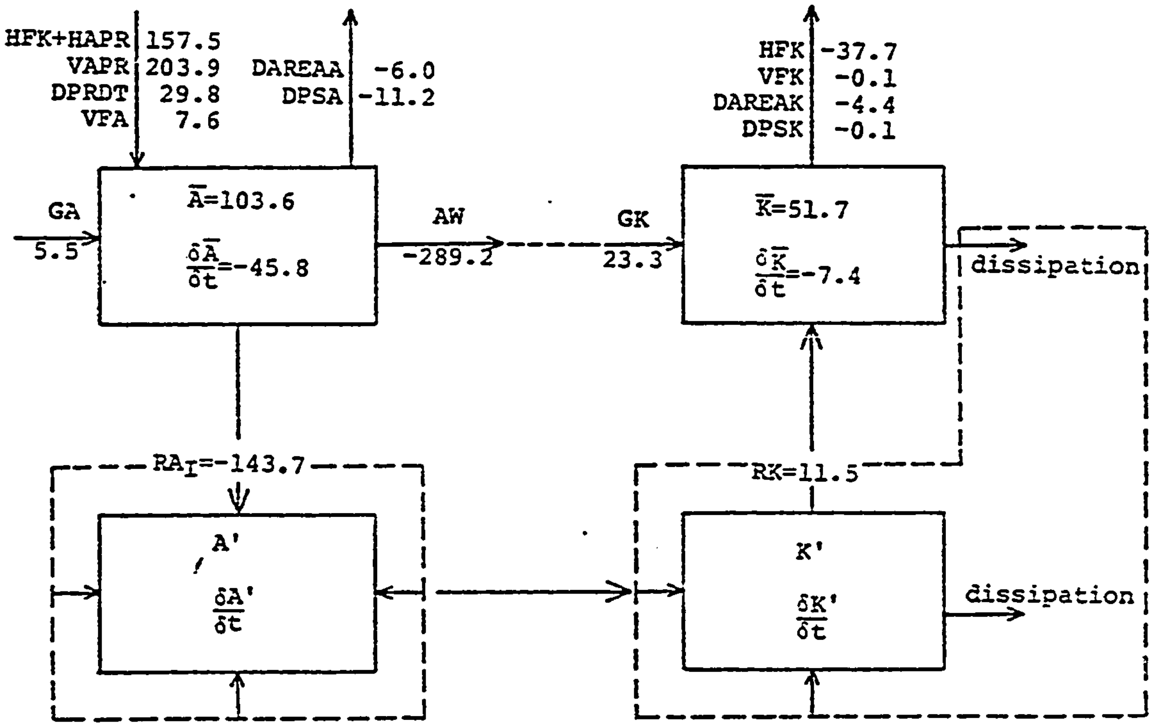

Fig. 47. The energy diagram of the AMTEX storm averaged from 0000 GMT 13 February to 1200 GMT 15 February. The units of $\bar{A}$ and $\bar{K}$ are 10^5 J m^{-2}; the units of all other quantities are W m^{-2}.

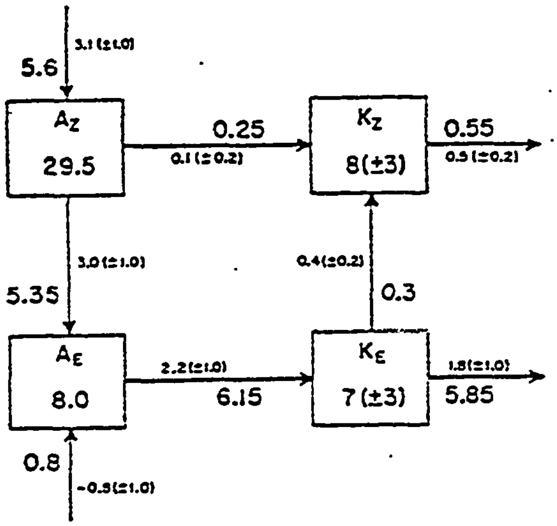

Fig. 48. The energy cycle of the atmosphere as estimated by Oort (1964) and Dutton and Johnson (1967). The estimates by Oort are indicated on the interior side of the arrows, and those by Dutton and Johnson are on the exterior side. The subscripts "Z" and "E" denote zonal and eddy, respectively. The unit of amounts of energy in the boxes is 10^5 J m^{-2}; the unit of energy transformation rates along the arrows is W m^{-2}.